UNIVERSIDAD NACIONAL AUTÓNOMA DE MEXICO
DOCTORADO EN CIENCIAS (FÍSICA)
INSTITUTO DE FÍSICA

CAPILLARY INTERACTIONS BETWEEN COLLOIDAL PARTICLES AT WATER/AIR INTERFACES

TESIS
QUE PARA OPTAR POR EL GRADO DE:
DOCTORA EN CIENCIAS (FÍSICA)

PRESENTA:
VIRGINIA CARRASCO FADANELLI

TUTOR PRINCIPAL
DR. ROLANDO CRISOSTOMO CASTILLO CABALLERO
INSTITUTO DE FÍSICA

MIEMBRO DEL COMITÉ TUTOR
DR. ALEJANDRO VÁSQUEZ ARZOLA
INSTITUTO DE FÍSICA

MIEMBRO DEL COMITÉ TUTOR
DR. HÉCTOR DOMÍNGUEZ CASTRO
INSTITUTO DE INVESTIGACIONES EN MATERIALES

CDMX, MAYO, 2020

To my family and friends.

Acknowledgments

Thanks to my principal advisor, Dr. Rolando Castillo, who has guided me and supported me in the process of this research project. Also, thanks to my advisory committee, Dr. Alejandro Vásquez Arzola and Dr. Héctor Domínguez Castro, for their help in discussions and evaluations.

Thanks to all members of the Complex Fluids Group at IFUNAM, especially to M.Sc. Salvador Ramos Solórzano and Erick Guzmán Gómez for their indispensable technical help as well as to Jorge I. Cruz Morales. Also, thanks to Dr. Erick Sarmiento Gómez, who was always available to help me in all my questions.

Thanks to Antonio Tavera, Zenaida Briceño, Natalia Rincón and Ricky López for their priceless friendship, good moments and support in hard times.

Finally, for the financial support, I thank the National Council of Science and Technology (CONACyT) under the program "Padrón Nacional de Posgrados de Calidad" and the support with the fellowship for SNI III. Thanks to DGAPA-UNAM under PAPIIT-2020 project.

Contents

1. Abstract

Colloidal particles adsorbed at fluid interfaces almost irreversibly and present unusual behavior. One of the most important characteristics of particles at fluid interfaces is self-assembly. This characteristic represents a very relevant property for different applications in basic science and industry. To assemble particles, it is critical to understand and know their interparticle interactions. If gravity forces over the particles are negligible (*Bond number* $\ll 1$), the interface close around the particles can be deformed due to the irregular shape of the contact line, pinned on nanoscopic sites on the colloid surface. Therefore, particles trapped on a planar interface can strongly interact, even when they are not charged. Stamou and collaborators theoretically derived the attraction between homogeneous uncharged microparticles trapped at the water/air interface, whose origin is the irregular shape of the contact line and its distortion of the water surface. Capillary interaction occurs between particles as they move to minimize the interfacial area. The most relevant term of the interaction potential (quadrupolar term) found by these authors and by others is: $\delta E_{AB} = -12\pi\gamma H_{A,2} H_{B,2} \cos\left[2(\phi_A - \phi_B)\right] \left(\frac{r_c}{r}\right)^4$, where the sphere and the water surface intersect at the average contact radius r_c, and r is the center-to-center distance between spheres. $H_{A,2}$ and $H_{B,2}$ are the heights of the meniscus at the contact line, γ is the liquid surface tension, the ϕ_A and ϕ_B are orientation angles of particles (A and B) relative to a line joining their centers.

The main goal of this thesis is to precisely measure capillary interactions between spherical hydrophilic, hydrophobic and Janus particles trapped at the air/water in-

terface. To achieve this task, we used time-shared optical tweezers. This optical technique allowed us to obtained precise measurements.

The colloidal particles used to make the measurements are microspheres made of hydrophobically covered silica. The measured radial force goes as a quadrupolar power law, r^{-n}, with $n = 5.02 \pm 0.18$ and $n = 5.04 \pm 0.18$ for particles of $3\mu m$ and $5\mu m$, respectively. In both cases, the electrostatic interaction is negligible.

The measured force for Janus particles goes from almost pure quadrupolar to almost pure hexapolar interaction due to the three-phase contact line corrugation. Measured force curves are modeled as a sum of power laws, $Ar^{-\alpha} + Br^{-\beta} + Cr^{-\gamma}$, obtained from an expansion in capillary multipoles. The mean values for the exponents of particles pairs of $3\mu m$ are $\langle\alpha\rangle = 5.05 \pm 0.12$, $\langle\beta\rangle = 7.02 \pm 0.03$, and $\langle\gamma\rangle = 5.96 \pm 0.03$. For particles pairs of $5\mu m$, we find $\langle\alpha\rangle = 5.02 \pm 0.04$, $\langle\beta\rangle = 6.94 \pm 0.06$, and $\langle\gamma\rangle = 5.80 \pm 0.05$. In both cases, $A < 0$, $B < 0$, and $C > 0$.

As can be seen from the results presented, the fitting of the experimental data has a form of r^{-5} for hydrophobic particles. This adjustment corresponds to a capillary attraction consistent with that calculated by Stamou. For the Janus case, the unexpected results obtained show how complex the phenomena is. With our results, we can conclude that the origin of the interaction between uncharged colloidal particles straddling at the air/water interface is due to the corrugated shape of the contact line, in agreement to the model of Stamou *et al.* and Danov *et al.*

2. Resumen

Cuando partículas coloidales son colocadas en alguna intercara fluida, éstas son adsorbidas en dicha intercara de manera casi irreversible y, además, presentan un comportamiento inusual. Una de las características más importantes de partículas coloidales adsorbidas en intercaras fluidas es el autoensamblaje. Esta característica representa una propiedad muy relevante para diferentes aplicaciones en ciencia básica e industria. Para el ensamblaje de las partículas, es fundamental comprender y conocer sus interacciones. Si la fuerza de gravedad sobre las partículas es despreciable ($No.\ de\ Bond \ll 1$), la intercara cerca de las partículas puede deformarse debido a la forma irregular de la línea de contacto, anclada en sitios nanoscópicos de la superficie coloidal. Por lo tanto, las partículas atrapadas en una intercara plana pueden interactuar fuertemente, incluso cuando no están cargadas. Stamou y colaboradores derivaron teóricamente la energía de atracción entre micropartículas homogéneas sin carga atrapadas en la intercara aire/agua, cuyo origen es la forma irregular de la línea de contacto y la irregularidad de la superficie del agua. La interacción capilar ocurre entre las partículas a medida que se mueven para lograr minimizar el área interfacial. El término más relevante del potencial de interacción (térmoni cuadrupolar) encontrado por estos autores y por otros es: $\delta E_{AB} = -12\pi\gamma H_{A,2} H_{B,2} \cos\left[2(\phi_A - \phi_B)\right] \left(\frac{r_c}{r}\right)^4$, donde r_c es el radio de contacto, y r es la distancia de centro a centro entre las partículas. $H_{A,2}$ y $H_{B,2}$ son las alturas del menisco en la línea de contacto, γ es la tensión superficial del líquido, ϕ_A y ϕ_B son ángulos de orientación de las partículas (A y B) en relación con una línea que une

sus centros.

El objetivo principal de esta tesis es medir con precisión las interacciones capilares entre partículas esféricas hidrofílicas, hidrófobas y Janus atrapadas en la intercara aire/agua. Para lograrlo, utilizamos pinzas ópticas de tiempo compartido. Esta técnica óptica nos permite obtener mediciones precisas.

La fuerza medida para partículas hidrofóbicas se aplica como una ley de potencia cuadrupolar, r^{-n}, con $n = 5.02 \pm 0.18$ y $n = 5.04 \pm 0.18$ para partículas de $3\mu m$ y $5\mu m$, respectivamente. En ambos casos, la interacción electrostática es insignificante.

La fuerza medida para las partículas Janus va desde la interacción cuadrupolar casi pura hasta la interacción hexapolar casi pura debida a la corrugación de la línea de contacto. Las curvas de fuerza medidas se modelan como una suma de leyes de potencia, $Ar^{-\alpha} + Br^{-\beta} + Cr^{-\gamma}$, obtenida de una expansión en multipolos capilares. Los valores medios para los exponentes de los pares de partículas de $3\mu m$ son $\langle\alpha\rangle = 5.05 \pm 0.12$, $\langle\beta\rangle = 7.02 \pm 0.03$ y $\langle\gamma\rangle = 5.96 \pm 0.03$. Para pares de partículas de $5\mu m$, encontramos $\langle\alpha\rangle = 5.02 \pm 0.04$, $\langle\beta\rangle = 6.94 \pm 0.06$ y $\langle\gamma\rangle = 5.80 \pm 0.05$. En ambos casos, $A < 0$, $B < 0$ y $C > 0$.

El ajuste de los datos experimentales tiene una forma de r^{-5} para partículas hidrofóbicas. Este ajuste corresponde a una atracción capilar consistente con la calculada por Stamou. Para el caso de partículas Janus, los resultados obtenidos fueron inesperados y muestran cuán complejo es el fenómeno. Con nuestros resultados, podemos concluir que el origen de la interacción entre las partículas coloidales no cargadas que se encuentran en la intercara aire/agua se debe a la forma corrugada de la línea de contacto, de acuerdo con el modelo de Stamou textit et al. y Danov textit et al.

3. Introduction

Colloidal systems surround us everywhere. From milk we pour to cereal in the morning to the paint of our walls are colloids, Fig. 3.1. Colloidal suspensions are mixture of tiny particles, ranging in size from a few nanometres to several micrometers, dispersed in a continuous phase. Typically, colloidal suspensions are classified depending on the type of particles and in the continuous phase in which they are dispersed. Table 3.1 summarizes all kinds of colloids that can be found.

Figure 3.1: Examples of colloidal systems present in everyday life.(a) Milk is a colloidal suspension named emulsion: liquid fat-globules are suspended in water. (b) Paint is a colloidal system named sol, where solid pigment particles are suspended in a liquid solvent solution. (c) Sprays in cosmetics are colloidal systems called aerosol consisting of liquid particles suspended in air or other gas.

Dispersed Phase	Dispersed Medium	Name of Colloidal Solution	Examples of the Colloid
Gas	Liquid	Foam	Soap lather, Whipped cream, soda water, froth etc.
Gas	Solid	Solid foam	Cake, Bread, Pumice stone lava.
Liquid	Gas	Aerosol	Mist, fog, clouds.
Liquid	Liquid	Emulsion	Milk, cream, butter, oil in water
Liquid	Solid	Gel	Curd, Cheese, Jellies, boot polish, butter.
Solid	Gas	Solid Aerosol	Smoke, dust
Solid	Liquid	Sols	Paints, cell fluid, inks
Solid	Solid	Solid Sols	Alloys, Coloured glass, gem stones.

Table 3.1: Colloidal suspensions can be classified according to different properties of the dispersed phase and medium. In this table is shown a classification based on the physical state of the dispersion medium and dispersed phase [1].

Colloids present phenomena like aggregation, flocculation, sedimentation, coalescence, or creaming depending on the predominant forces acting on them. In industry, these processes could be a significant problem to address and understand to control at will.

The behavior of colloidal systems can be described by DLVO theory established by Derjaguin, Landau, Verwey, and Overbeek in the 1940s (Derjaguin and Landau 1941, Verwey and Overbeek 1948). This theory is based on the assumption that the electrostatic double-layer forces, the van der Waals forces and the hardcore inter-

actions between the particles are independent and therefore, can be superimposed or added at each interacting distance. Van der Waals forces are the result of forces between molecules in each colloidal particle and are usually attractive. The electrostatic forces are due to the dissociation of surface groups into the continuous phase creating an electric double layer, these forces are repulsive. The hardcore interactions exclude the interpenetration of approaching surfaces. The sum of these forces describes the behaviour of the colloidal system, Fig. 3.2. However, when colloidal particles are constrained at a fluid interface, these theories can not predict their stability correctly.

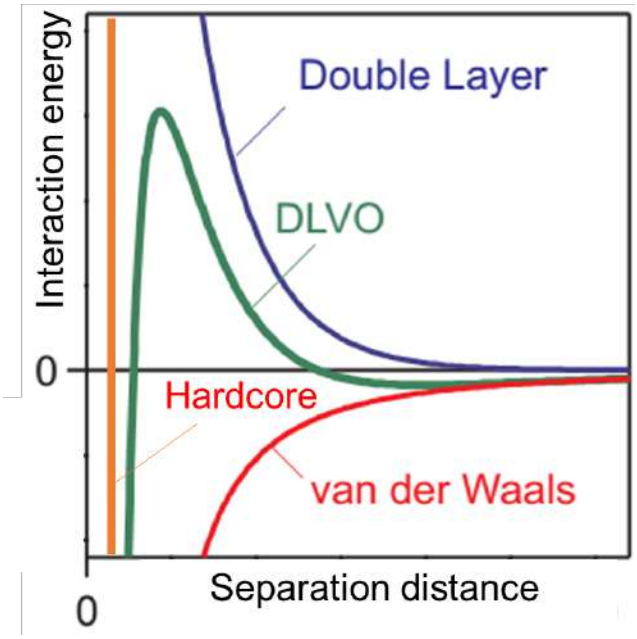

Figure 3.2: Van der Waals interactions dictate the profiles at large and small distances, while the double layer force dominates the intermediate distances. At contact, the DLVO profile is infinitely deep, but in reality, repulsive forces are acting at very short distances.

Colloidal particles have the characteristic that under some conditions — if large enough and of the right wettability properties — are adsorbed at a fluid interface almost irreversibly (details in Appendix A). This feature gives them the ability to stabilize emulsions and foams better than surfactants do. Ramsden first noted the adsorption of colloidal particles at fluid-fluid interfaces in 1903, followed by Pickering. They observed many new effects when particles had been confined to a $2D$ space[2],[3]. Particles at interfaces can self-assemble. This ability represents a very relevant property for different applications. Among other things, it is used for the construction of solid nanostructured surfaces in both two and three dimensions [4], [5], the formation of electro-optical and electronic devices [23], bicontinuous interfacially jammed emulsion gels (or "bijels") [6], [7], in the stabilization of Pickering emulsions and in the creation of novel materials with interesting features [8], [9].

Interparticle interactions are vital in understanding the self-assembly of particles at interfaces. The origin of colloidal systems interactions and the consequences in their behavior are discussed in the next section.

3.1 Capillary interactions

When particles are trapped at the interface of two fluids, there are interactions not present between particles immersed in the liquid. These interactions can be divided into two general categories: dipole-dipole interactions and capillary interactions.

An outline of all the interactions between colloidal particles in a fluid interface is shown in Fig. 3.3: dipole-dipole interactions, (Fig. 3.3 (b), (c) and (f)) and capillary interactions (Fig. 3.3 (a), (d) and (e)) [24].

Dipole-dipole interactions are due to the solvation or dissociation, either homogeneously or inhomogeneously, of charged functional groups on the surface of the

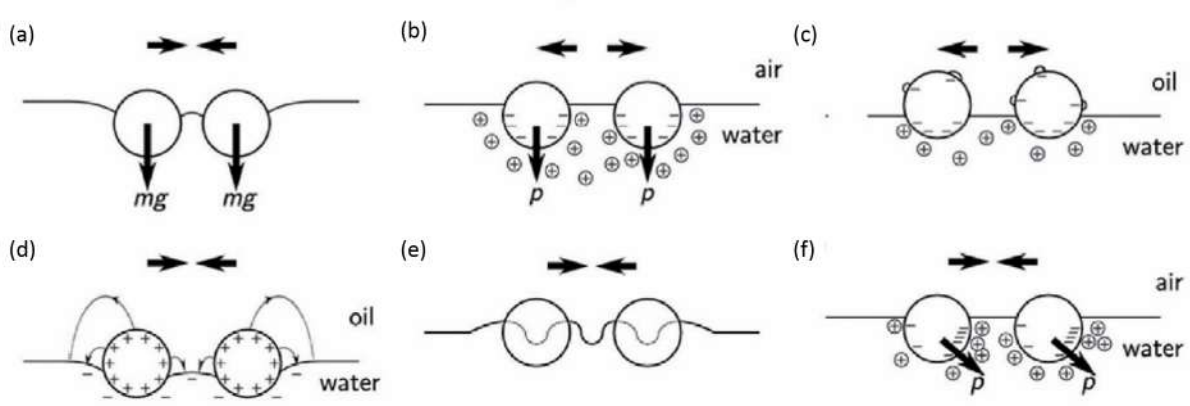

Figure 3.3: Scheme of the interactions of colloidal particles at interfaces [10].

particles. This solvation creates a double electrical layer in the portion of the particles that is submerged in the water, generating dipoles. These dipoles interact with each other, producing attractions or repulsions. These electrostatic interactions stabilize most colloidal suspensions against aggregation.

On the other hand, capillary interactions are due to the deformation of the liquid surface where the particles are trapped. In the absence of particles, the surface is assumed to be flat. The interaction between particles is directly proportional to the deformation produced by the particle. Although capillary interactions arise from deformations of the fluid interface, these deformations have a varied nature.

Flotation forces predominate in particles whose Bond numbers are $B \gg 1$ [1]. Deformations of the fluid surface generate these forces due to gravity. They are a consequence of the balance between the weight of the object, the surface tension and the buoyant force. When two particles float in the fluid interface, they approach or

[1]Bond number measures the importance of gravity with respect to surface tension. This number is given by $B = \frac{\Delta\rho g R^2}{\gamma}$, where $\Delta\rho$ is the difference in densities of the two media, g is the gravity, R is the characteristic length of the particle and γ is the surface tension. When $B \ll 1$, the deformation of the fluid surface due to the weight of the particle is negligible. For large particles $B >> 1$, the weight is responsible for the deformation of the interface.

move away; the menisci of both particles are altered in such a way that the gravitational potential energy of the system reaches a minimum. This effect is known as the 'Cheerios effect' [11]. Fig. 3.4 shows two objects attracted by capillary interactions by flotation [12].

Figure 3.4: When we pour cereal in milk, we can observe that they attract each other, forming aggregates. Also, we notice that cereal tends to go to the sides of the plate. This attraction is due to capillary forces. This effect is known as the Cheerios effect.

If the particle size is decreased until $B \ll 1$, the buoyant force also decreases and becomes negligible. Then, two other capillary interactions begin to predominate: (1) one due to deformations caused by electric fields and (2) other due to deformations caused by an irregular contact line.

(1) Charged particles produce electric fields around them. These fields produce deformations of the interface, Fig. 3.3 (d) [13].

The other (2) is a capillary interaction caused by local interface deformations due to the pinning of the fluid on the surface of the particles in random places, Fig. 3.3 (e). The contact line, which is the line corresponding to the union of the three phases and discussed in detail later, is irregularly pinning on physical or chemical defects on the surface of the particles, Fig. 3.3 (e), causing deformations in the fluid interface around the particles. The interparticle interaction potential due to these distortions

of the interface decays as r^{-4} (Fig. 3.5), as will be discussed in other section. This interaction acts over long distances (about a diameter between particles), where Van der Waals forces are negligible.

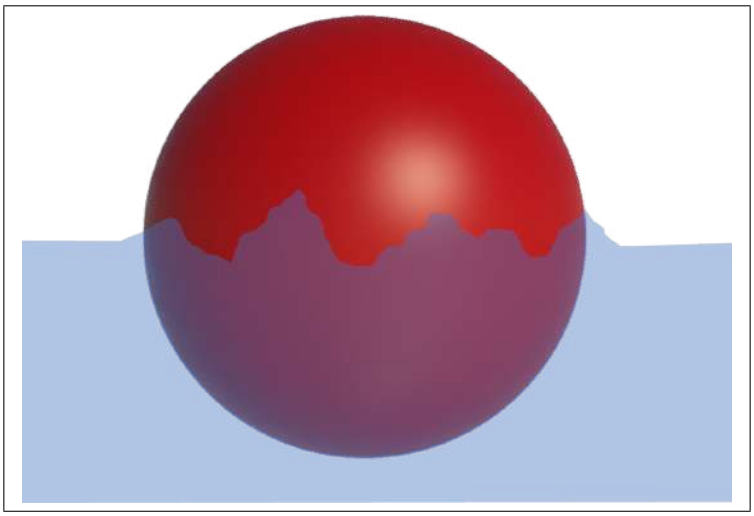

Figure 3.5: Deformations of the surface around a particle due to the pinning of the contact line.

Contact Angle and Contact Line The contact angle is a function of the surface energies of the particle–fluid and fluid–fluid interfaces. Is defined by the angle formed by the intersection of the solid-liquid interface and the liquid-vapour interface, as seen in Fig. 3.6. The interface where the solid, liquid and vapour coexist is called the contact line.

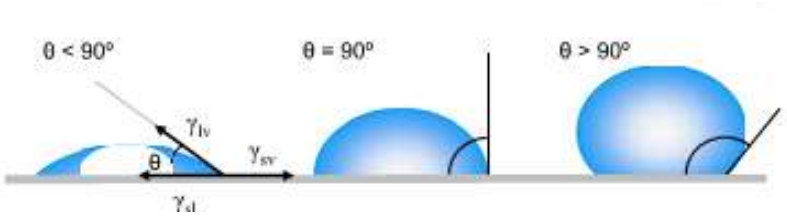

Figure 3.6: Illustration of the contact angles formed by a drop on a solid, homogeneous and smooth surface.

Contact angles less than 90° generally mean that the solid is hydrophilic, and the liquid partially wets the solid surface. Contact angles greater than 90° mean the solid is hydrophobic, so the liquid tends to minimize its contact with the solid surface. When the angle is 0°, there is a complete wet, that is, a drop of water on a surface wets it completely when such drop spreads totally on the solid. The contact angle is defined by the thermodynamic equilibrium of the drop under the action of three surface tensions or energies,

$$\gamma_{lv} \cos\theta_Y = \gamma_{sv} - \gamma_{sl} \tag{3.1}$$

Where γ_{lv}, γ_{sv}, and γ_{sl} represent the surface tensions liquid-vapour, solid-vapour, and solid-liquid, respectively, and θ_Y is the contact angle. The equation 3.1 is known as the Young's equation. From this equation, applied to a specific system, and with three thermodynamic parameters, a single contact angle θ_Y is determined. In practice, this is not so, because there are metastable states of a drop on a solid, and the contact angle is not equal to θ_Y. That is if we push the drop forward or backward, or the equivalent of tilting the substrate, the contact angles of the front and back of the drop are not equal [16]. These angles are known as the advancing and receding angles, respectively, Fig. 3.7. The difference between the receding angle, θ_r, and

advancing angle, θ_a, is called the angle of hysteresis, H:

$$H = \theta_a - \theta_r \tag{3.2}$$

The significance of contact angle hysteresis has been extensively investigated [18]-[21]. The general conclusion is that it results from surface roughness and chemical heterogeneity [17]. De Gennes named the defects where the contact line is pinned as *pinning points* [22].

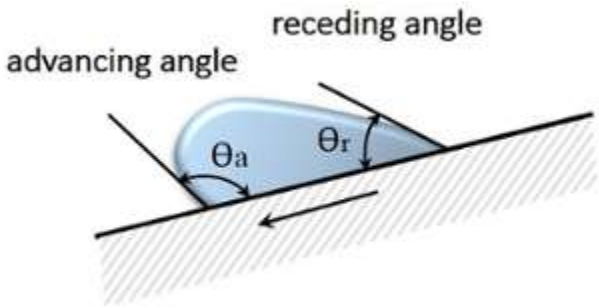

Figure 3.7: Diagram of the contact angle hysteresis.

For anisotropic particles, such as colloidal ellipsoids, rods, or doublets, it is impossible to satisfy the three-phase contact angle over the entire particle perimeter without inducing deformation in the interface.

When colloidal particles at interfaces have a negligible charge (essentially neutral), dipole-dipole interactions are reduced to a minimum. The only predominant interaction comes from capillarity due to the pinning of the fluid on the particle surface (for colloidal particles $B \ll 1$). However, there is no direct evidence of the corrugation line and the interface distortion in spherical microspheres. Boniello *et al.*

[14] using phase-shifting interferometry, where the vertical resolution was enhanced to 1 nm, found no noticeable deformation of the interface in the range of a few micrometers around the particle position trapped at the air/water interface. Despite this, the authors found a relation between diffusion and particle immersion in terms of thermally activated fluctuations of the interface, at the triple line, driving the system out of mechanical equilibrium and giving extra random forces on the particle. Also, with an optical technique, Kaz *et al.* [15] captured the details of a particle approaching an interface, the moment it breaches, and the slow logarithmic time relaxation that follows. The contact line and its undulations move along the particle surface. Hence, the accompanying interfacial distortion can fluctuate over time. The observed dynamics agree with a model describing activated hopping of the contact line over nanoscale surface heterogeneities, resembling the aging dynamics in glassy systems. Therefore, precise measurements of this capillary interaction are relevant because it is the only way to account for the corrugations that, most of the times, it is used as a convenient assumption. Theoretical derivations of capillary attraction between homogeneous uncharged microparticles trapped at air/water interface, whose origin is the irregular shape of the contact line and its resulting distortion of the water surface have been done. The most relevant term of the interaction potential found by these theoretical analyses depends on interparticle distance as r^{-4} as discussed further in the next section.

3.2 Homogeneous particles at interfaces

Though the idea of pinning points was brought many years ago, it was until 2001 that Stamou, Duschl *et al.* [27] proposed that capillary forces in systems of colloidal particles trapped at interfaces were caused by pinning points. This assumption

came after observing spherical negatively charged particles of polystyrene of $0.5 - 5\mu m$ in diameter. They observed aggregates in which interparticle distances were greater than a micrometer. Van der Waals forces could not attain these attractive interactions due to the long interparticle distances neither by buoyancy forces because of the small size of the particles, where their Bond number was of the order of $\approx 10^{-5}$. The mechanism to explain these observations was based on the notion that the particle surface is not perfectly smooth; on the contrary, it has chemical and physical defects. The interface close around the particles is then deformed due to the irregular shape of the contact line, pinned on the defects sites or pinning points of the particle surface, as shown in Fig.3.8. Therefore, particles trapped on a planar interface can strongly interact to lower surface energy, even when they are not charged [28].

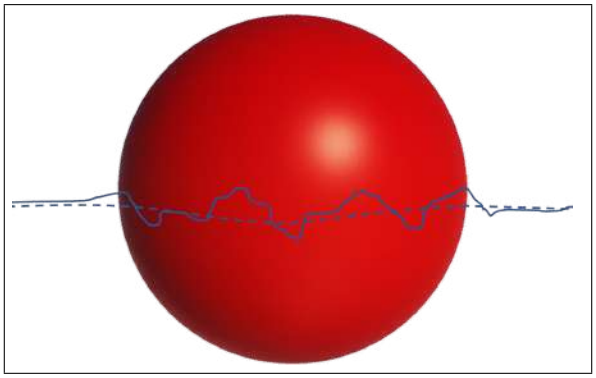

Figure 3.8: Schematic description of the three contact line due to the pinning points. The dashed line is the ideal flatted straight contact line. The continuous line shows the contact line due to pinning points.

Deformations around the particles trapped at an originally planar air/water interface create an excess interface surface area. When two adjacent particles assume an optimum relative orientation and distance, this excess area is minimized. Sta-

mou *et al.* first derived an expression for the height of the water surface around an isolated particle. From this height, an excess area dS created at the air/water interface can be calculated. The energy cost per particle is $dE = \gamma dS$, where γ is the air/water interface tension. Subsequently, Stamou*et al.* derived an approximation of the excess area around two interacting particles A and B. With the single-particle energy one can obtain the interaction energy as $dE_{AB} = \gamma(\delta S_{AB} - \delta S_A - \delta S_B)$.

The mean curvature of the water surface vanishes everywhere accordingly with Young's equation [29] because the effects of gravity are ignored, and the pressure across the water surface is zero. It is assumed that the slope of the water surface is small everywhere ($\ll 45°$), therefore the approximated mean curvature is $\Delta h(r, \phi)$ with Δ the Laplace operator and $h(r, \phi)$ the local water level.

As a result (in cylindrical coordinates) we have left that

$$\Delta h(r, \phi) = \left(\frac{1}{r} \frac{\partial}{\partial r} r \frac{\partial}{\partial r} + \frac{1}{r^2} \frac{\partial^2}{\partial \phi^2} \right) h(r, \phi) = 0. \tag{3.3}$$

To solve equation 3.3 $h(r, \phi)$ can be written as a product of two independent variables, in the form given in 3.4.

$$h(r, \phi) = R(r)\Phi(\phi). \tag{3.4}$$

The solutions are of the form

$$\Phi_m(\phi) = \Phi_{m,0} \cos(m(\phi - \phi_{m,0})), \tag{3.5}$$

$$R_m(r) = R_{m,0} r^{-m}. \tag{3.6}$$

And thus, we have that

$$h(r,\phi) = \sum_{m=0}^{\infty} R_{m,0}\Phi_{m,0}\cos(m(\phi-\phi_{m,0}))r^{-m}. \tag{3.7}$$

In equation 3.7, the coefficients $\Phi_{m,0}$, $R_{m,0}$ y $\phi_{m,0}$ come from the boundary conditions. The sphere and the water surface intersect at the contact radius r_c which is close to the particle radius R (unless the contact angle is very small or very large). Therefore, the height of the contact line $h(r_c,\phi)$ can be expressed with a multipolar approximation as

$$h(r_c,\phi) = \sum_{m=0}^{\infty} H_m \cos\left(m(\phi-\phi_{m,0})\right), \tag{3.8}$$

with $H_m = R_{m,0}\Phi_{m,0}r_c^{-m}$. The monopole $m = 0$ term is forbidden because there is no external force like gravity dragging the particle away from its optimum height. The dipolar term, $m = 1$, is also neglected because there is no torque force due to the homogeneity of the particle surface: it is symmetric. The next term is the quadrupolar term, $m = 2$. This term predominates over the forthcoming ones. Equation 3.8 states that the different multipole orders decay with an inverse power equal to the multipole order. The quadrupole order is the lowest allowed order and decays as r^{-2}. For a long-range interaction, the quadrupole term is the most important one. Approximating $h(r,\phi)$ to the quadrupolar term, one obtains

$$h(r,\phi) = H_2\cos(2(\phi-\phi_{2,0}))\left(\frac{r_c}{r}\right)^2. \tag{3.9}$$

The coefficient H_2 gives the height of the water surface around the particle at the contact line. The water surface around the particle (when $r = r_c$) has a "quadrupolar" distortion, that is, the contact line follows the law $h(r,\phi) = H_2\cos(2(\phi-\phi_{2,0}))$, with ϕ the azimuthal angle and $\phi_{2,0}$ the orientation of the particles. This quadrupolar

distortion is shown in Fig. 3.9.

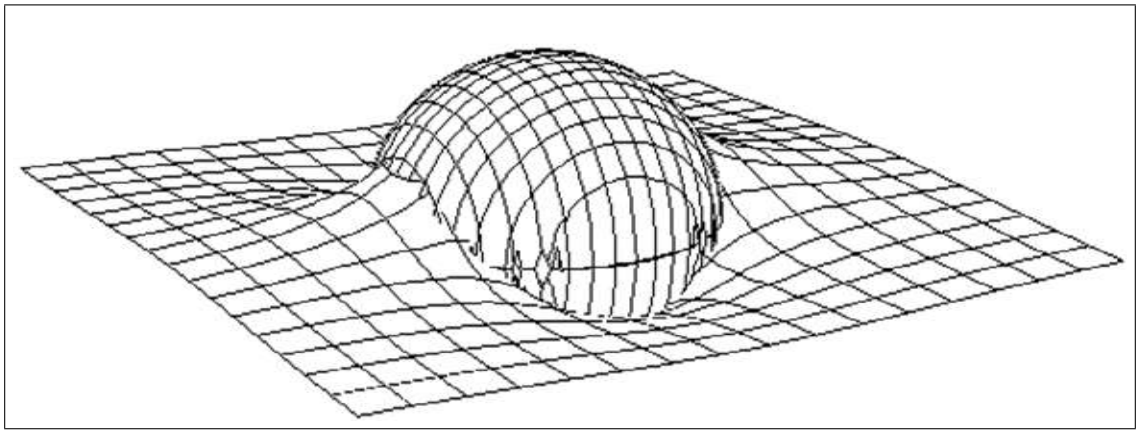

Figure 3.9: Water surface around the particle (when $r = r_c$) has a "quadrupolar" distortion, that is, the contact line follows the law $h(r, \phi) = H_2 \cos(2(\phi - \phi_{2,0}))$, with ϕ the azimuthal angle and $\phi_{2,0}$ the orientation of the particles.

Next, it is necessary to find the particle's energy at the water/air interface due to its distortion. The excess interfacial area, δS multiplied by the surface tension, γ gives the particle's energy as expressed by 3.10.

$$\delta E = \gamma \delta S. \tag{3.10}$$

The excess interfacial area is obtained considering an infinitesimal element between the flat interfacial area and the distorted interfacial area. Then, the integration of this infinitesimal element gives us

$$\delta S = \frac{1}{2} \int_{r=r_c}^{\infty} \int_{\phi=0}^{2\pi} (\nabla h)^2 r d\phi dr = 4 H_2^2 r_c^4 r^{-6} \tag{3.11}$$

In consequence, the energy of a particle at the interface, $\delta E = \gamma \delta S$, is given as

$$\delta E = 2\gamma H_2^2 r_c^4 2\pi \int_{r=r_c}^{\infty} r^{-6} = \pi\gamma H_2^2. \tag{3.12}$$

The prefactor H_2 can be estimated from experimental values of contact angle hysteresis for silica particles and water, $\Delta\theta \approx 30^\circ$ [30]. The value for pinning-induced deviations from the ideal contact line for a silica particle of 3 μm in diameter is $H_2 \approx \frac{1}{2}R \times \Delta\theta \approx 25\ nm$, which is about 2% of the particle radius. With these input parameters, the self energy δE comes out to be $\delta E \approx 10^5 kT$.

The interaction between two particles, A y B, with a center-of-mass separation r, δE_{AB}, is given by

$$\delta E_{AB} = \gamma(\delta S_{AB} - \delta S_A - \delta S_B), \tag{3.13}$$

with δS_{AB} the surface area around the interacting particles, δS_A and δS_B the surface area around each isolated particle.

The potential fields h_A and h_B are considered as produced from hypothetical isolated particles A and B that overlap, thus $h_{AB} = h_A + h_B$. One can assume that the field h_A is small at particle B, and conversely. Hence, from equation 3.13 and equation 3.11 one gets

$$\delta E_{AB} = \frac{\gamma}{2}\int[(\nabla(h_A + h_B))^2 - (\nabla h_A)^2 - (\nabla h_B)^2]dS = \gamma\int \nabla h_A \cdot \nabla h_B dS \tag{3.14}$$

The integral over the area can be transformed into an integral over a line C using the first Green identity.

$$\delta E_{AB} = \int_C h_B(\vec{n} \cdot \nabla h_A)dC \tag{3.15}$$

where $\vec{n}$ is a unit vector perpendicular to the boundary pointing away from the integration area. As a result of the integration, the total interaction energy, δE_{AB} is

$$\delta E_{AB} = -12\pi\gamma H_{A,2} H_{B,2} \cos\left[2(\phi_A - \phi_B)\right] \left(\frac{r_c}{r}\right)^4, \tag{3.16}$$

where ϕ_A and ϕ_B are the angles relative to the line joining the particles and $H_{A,2}$, $H_{B,2}$ are the heights of the contact line deformation of particles A and B, respectively (as shown in Fig. 3.10). When the two particles approach, they first rotate between them until they find a stable orientation in which $\cos[2(\phi_A - \phi_B)]$ is a minimum. Then, the particles come closer to each other to minimize the system's energy.

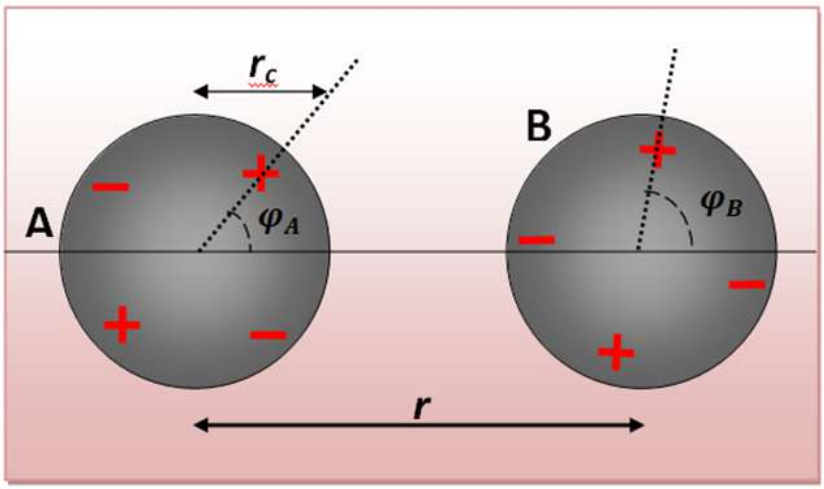

Figure 3.10: Schematic representation of the particles A and B separated a distance r from their centers of mass. The signs + and − refer to the parts where there are an elevation and a depression, respectively, with respect to the flat surface of the water.

Subsequently, Danov *et al* [31] following Stamou's proposal derived a theoretical expression for the interaction between two capillary multiples of arbitrary order. They considered two solid particles, A and B. The total interaction energy due to

surface deformation obtained in Ref. [31] for the general case is

$$\delta E_{AB}(r \to \infty) = \frac{\pi\gamma}{2}(m_A H_A^2 + m_B H_B^2). \tag{3.17}$$

In Table 3.2, obtained by Danov *et al.*, is shown the analytical expression for the energy of two particles separated by a distance r. In this Table is included the case $m_A = 0$, where one of the interacting particles has a Bond number $B > 1$ (not negligible weight), as shown in Fig. 3.3(a). In the special case when $m_A = m_B = 2$, the same result obtained by Stamou *et al.* of capillary quadrupoles is obtained. Typically, for $H \geq 5\ nm$, the energy δE_{AB} associated with this value of H is much greater than the thermal energy kT, so that capillary forces between multiples have an influence that must be taken into account when studying the phenomena with monolayers of particles at fluid-fluid interfaces.

Type of interaction	$(m_{\mathrm{A}}, m_{\mathrm{B}})$	Interaction energy $\delta E_{AB}(r)$ for r_A , $r_B \ll r \ll q^{-1}$
Charge–quadrupole	$(0, 2)$	$-\frac{\pi}{2}\sigma Q_{\mathrm{A}} H_{\mathrm{B}} \cos[2(\varphi_{\mathrm{B}} - \pi)]\left(\frac{r_B}{r}\right)^2$
Charge–multipole	$(0, m_{\mathrm{B}})$	$-\frac{\pi}{2}\sigma Q_{\mathrm{A}} H_{\mathrm{B}} \cos[m_{\mathrm{B}}(\varphi_{\mathrm{B}} - \pi)]\left(\frac{r_B}{r}\right)^{m_{\mathrm{B}}}$
Dipole–quadrupole	$(1, 2)$	$4\pi\sigma H_{\mathrm{A}} H_{\mathrm{B}} \cos[\varphi_{\mathrm{A}} - 2\varphi_{\mathrm{B}}] \frac{r_A r_B^2}{r^3}$
Quadrupole–quadrup	$(2, 2)$	$-12\pi\sigma H_{\mathrm{A}} H_{\mathrm{B}} \cos[2(\varphi_{\mathrm{A}} - \varphi_{\mathrm{B}})] \frac{(r_A r_B)^2}{r^4}$
Quadrupole–hexapol	$(2, 3)$	$24\pi\sigma H_{\mathrm{A}} H_{\mathrm{B}} \cos(2\varphi_{\mathrm{A}} - 3\varphi_{\mathrm{B}}) \frac{r_A^2 r_B^3}{r^5}$
Hexapole–hexapole	$(3, 3)$	$-60\pi\sigma H_{\mathrm{A}} H_{\mathrm{B}} \cos(3\varphi_{\mathrm{A}} - 3\varphi_{\mathrm{B}}) \frac{r_A^3 r_B^3}{r^6}$
Hexapole–octupole	$(3, 4)$	$120\pi\sigma H_{\mathrm{A}} H_{\mathrm{B}} \cos(3\varphi_{\mathrm{A}} - 4\varphi_{\mathrm{B}}) \frac{r_A^3 r_B^4}{r^7}$
Multipole–multipole	$(m_{\mathrm{A}}, m_{\mathrm{B}})$	$-G_0\pi\sigma H_{\mathrm{A}} H_{\mathrm{B}} \cos(m_{\mathrm{A}}\varphi_{\mathrm{A}} - m_{\mathrm{B}}\varphi_{\mathrm{B}}) \frac{r_A^{m_{\mathrm{A}}} r_B^{m_{\mathrm{B}}}}{r^{(m_{\mathrm{A}}+m_{\mathrm{B}})}}$

Table 3.2: Expressions for the total interaction energy δE_{AB} for some cases, corresponding to different m_A and m_B. r_A and r_B are the contact radius of the contact line for the corresponding A and B particles.

Particles with a quadrupolar predominance (m=2) tend to assemble in a square lattice, whereas particles with a hexapolar predominance (m=3) preferably form a hexagonal lattice, with or without voids (Fig. 3.11), in agreement with the results obtained in Refs. [27] and [31]. Another possibility is that the particles could form simple linear (chain) aggregates. Such structures have been observed experimentally [32]-[34] and [35].

The above-mentioned theoretical results highlight the importance of experimental evidence to observe the interface's deformations due to the presence of colloidal particles. However, as was commented before, some attempts to observe the irregu-

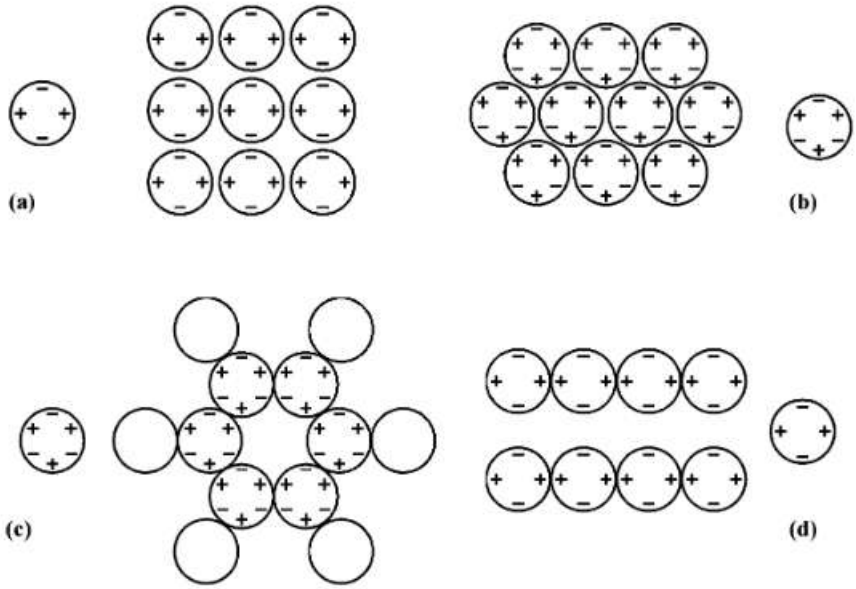

Figure 3.11: Arrays formed by capillary quadrupoles ($m = 2$) and hexapoles ($m = 3$); the signs '+' and '−' denote, respectively, positive and negative 'capillary charges,' i.e., convex and concave local deviations of the meniscus shape from planarity at the contact line. (a) Quadrupoles form a tetragonal close-packed array. Hexapoles could form (b) close-packed array; (c) hexagonal array with voids. (d) Linear aggregates made of quadrupoles. In contrast with the electric charges, two similar capillary charges attract each other, while the interaction between opposite capillary charges is repulsive.

lar contact line have been carried out with no success [14],[15]. Nonetheless, precise experimental measurements of the interaction forces between particles at interfaces can determine if this interaction force depends on distance as a r^{-5} power law as calculated theoretically in Refs. [27], [31]. Park and Furst [36] reported measurements of capillary interactions due to the irregular contact line in spherical particles. These authors confirmed the presence of a long-range capillary attraction measuring the effect of the ionic strength on the interaction force between spherical charged colloidal particles, as well as, between colloidal doublets straddling on a decane–water

interface using different concentration of salt in the water phase and surfactant in the oil phase. They measured the interaction between pairs of polystyrene latex particles that were charge-stabilized with surface sulfate groups of 3 μm of diameter trapped at an oil/water interface using time-shared optical tweezers. Their experimental arrangement consisted of an interface formed by decane and water in a flow cell (where the interface was located) placed above an inverted microscope objective (Fig. 3.12(a)).

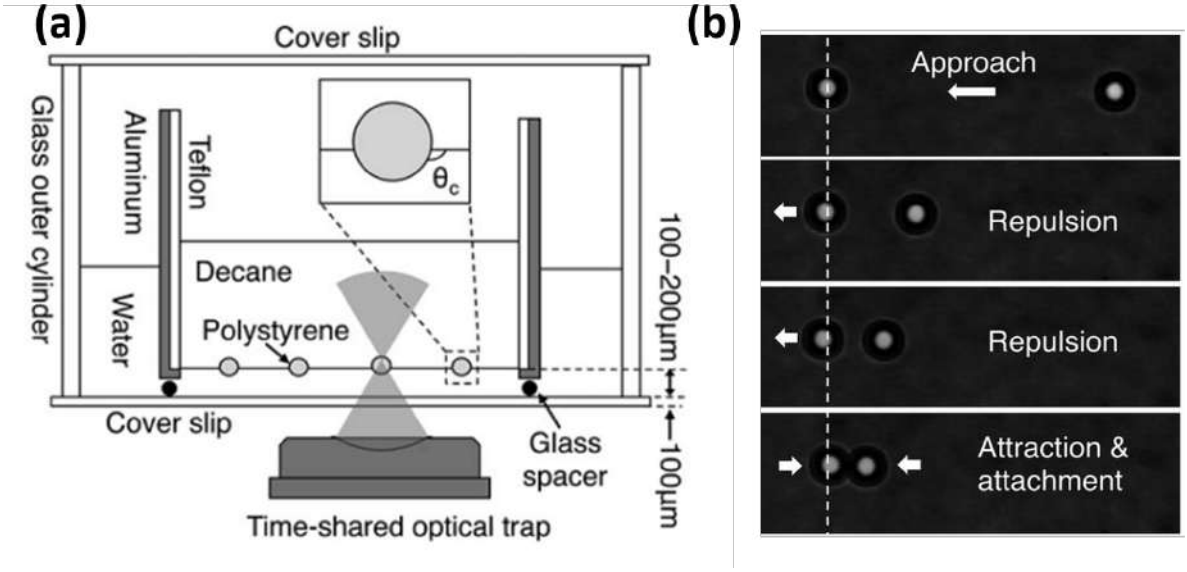

Figure 3.12: (a) Park and Furst experimental geometry consisted of an interface formed by water and decane. A flow cell, constructed from an outer glass cylinder and an inner cylinder made of aluminum placed on the stage of an inverted microscope. Glass beads acted as spacers to provide contact between the water phase and the water reservoir outside of the inner cylinder assembly. (b) Snapshots for the direct measurement of the interaction force between two spherical particles using time-shared optical traps.[36].

Park and Furst trapped two particles with optical tweezers that were calibrated using the particle drag force method. They initially placed them at a large distance from each other, so their interaction was negligible. Then, the particle on the right in Fig. 3.12 (b) was approximated to the stationary particle in the left. The stationary particle shifted from its equilibrium position, which is indicated with the dashed line. This displacement depended on the magnitude of the repulsion or attraction

between the particles. In some cases, at certain separation distance, the particles, the particles jump into contact.

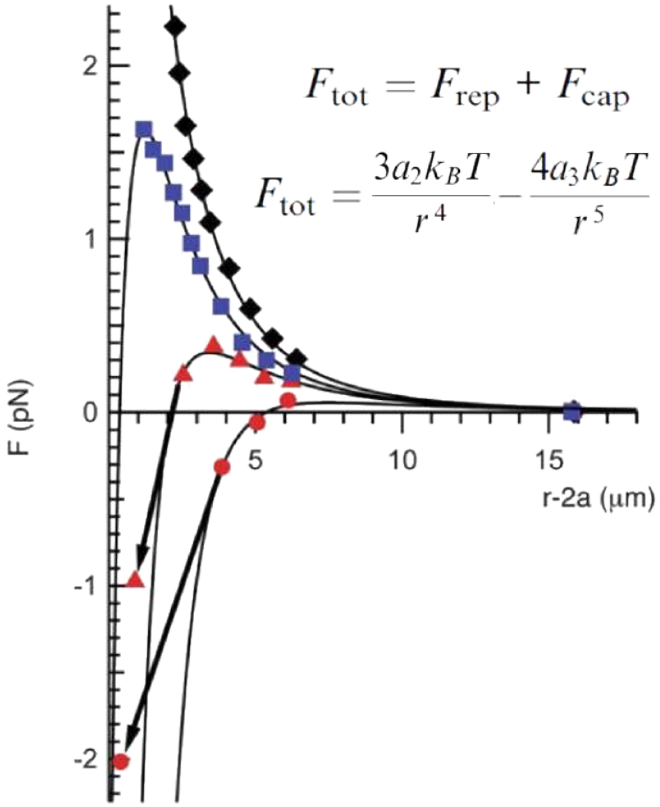

Figure 3.13: Representative total interaction forces obtained by Park and Furst. Different colors correspond to a different salt concentration. The fitting (line) was made with $F_{tot} = F_rep(r) + F_{cap}$ as assumption [36].

Particles presented repulsive forces that were in agreement with a dipole-dipole repulsion: $F_rep(r) = \frac{3a_2k_BT}{r^4}$, with a_2 a prefactor which quantifies the magnitude of the repulsive interaction. Several force curves deviated from the expected $F_{rep} \approx r^{-4}$ and in the near field exhibit a weaker repulsion or even a jump-in to attraction. The authors added salts to screen charges responsible for the repulsion to observe

the presence of this weaker attractive force. The greater the salt concentration, the weaker the repulsive force was. The particles interacted attractively at distances of the order of micrometers, where van der Waals forces were negligible, as can be seen in Fig. 3.13. The total force measured was at different salt concentrations, and it was modeled as $F_{tot} = F_{rep} + F_{cap}$, where the attractive force, $F_{cap} = \frac{4a_3 k_B T}{r^5}$, corresponds to the quadrupole capillary interactions that arise from the deformation of the interface, as suggested by Stamou *et al* and the repulsive force was as mentioned before. The height of the meniscus calculated from their results had an approximate value of 45 nm.

However, their measurements presented low precision. Furthermore, some considerations about the authors' results are: (1) As mentioned above, the optical tweezers were calibrated using the particle drag force method. In this method, particles trapped at the oil/water interface are subjected to solvent drag forces by translating the microscope stage at a constant velocity, U. The particle displacement from the optical trap δx is measured as a function of the imposed Stokes drag force, $F_s = 6\pi a \eta_{eff} U$, with $\eta_{eff} = [\eta_{oil}(1 - \cos\theta) + \eta_{water}(1 + \cos\theta)]/2$ the effective viscosity. Nevertheless, taking the effective viscosity, η_{eff}, as a simple average, is not quite accurate. Nobili *et al.* have shown experimentally that particles at fluid interfaces present thermally activated fluctuations at the contact line that induce an extra viscous drag force on the particle that leads to a measured diffusion slowing down. (2) Particles at oil/water interfaces could present disassociated charges in the particle surface exposed to the oil phase. The inhomogeneous charge disassociation can contribute to both attractive and repulsive interactions. From the experimental results, the authors could not tell if the inhomogeneous charge disassociation was present. (3) The addition of salt and surfactants to the sub-phases can affect the particles' contact angle in unexpected ways that were not taken into account in the

results. (4) The measurements presented an error of almost 10%.

A. Kozina, S. Ramos, P. Díaz-Leyv and R. Castillo [37] studied the ordering of hydrophobic and hydrophilic particles (silica particles of 3 μm in diameter) in an air/water interface. They found that hydrophilic particles (which were not modified on their surface), were more orderly compared to hydrophobic particles (which were chemically modified). They also observed that the positional and orientational correlation functions declined faster for hydrophobic particles. The authors suggested the effective potential that determines the structure must be the superposition of the capillary depending on the orientation and all other electrostatic interactions. If $H_2^A \sin H_2^B$, the capillary interaction implies that the particles move and rotate until they form a square configuration with a phase difference of zero. Therefore, the hexagonal order is not favorable unless the density of the system is increased, resulting in the particles being so close to each other that hardcore forces dominate: the two orientation orders compete. The quadrupole interaction is frustrated by hexagonal arrangements at high densities, which introduces an anisotropy and explains why the orientation order of union decays so fast with a small variation in density. The modified particles have more surface defects and therefore seem to contribute to increasing the height h_2 of the contact line. In turn, the capillary interaction is stronger, resulting in a greater decay in the order correlation function. Nevertheless, the results of this thesis show that are not dipole interactions but hexagonal interactions that play a role.

3.3 Inhomogeneous particles at interfaces

Janus particles are heterogeneously coated particles that posses areas on their surface of different functionality, for example, hydrophilic and hydrophobic. The

definition of Janus particles is extended to particles with anisotropic structures that contain optical, electrical, or magnetic properties as physical properties, often contrary in nature[38]-[41]. Janus particles were suggested by Pierre-Gilles de Gennes when he made his Nobel Laureate speech in 1991 [42]. Janus particles are both surface-active and amphiphilic. Although Janus particles inherit some features observed in homogeneous colloidal particles straddling at interfaces, Janus particles present new challenges for understanding their behavior, which is different from those when they are spread in bulk. Janus particles also have exciting applications as solid surfactants for the stabilization of mixtures with various phases such as emulsions and foams [43]. Janus particles have promising applications in medicine for drug delivery, where a single Janus particle material with multiple domains can simultaneously realize multidrug loading and serve as an ideal carrier [44]-[46]. Another relevant field of application of Janus particles is in the preparation of self-propelled objects, which could be used as nano and micropumps, cell transport, sensing, or water purification[47]-[49]. When Janus particles are at a fluid interface, their surface heterogeneities produce very irregular contact lines and, therefore, capillary interactions between the particles are manifested (Figure 3.14) [52].

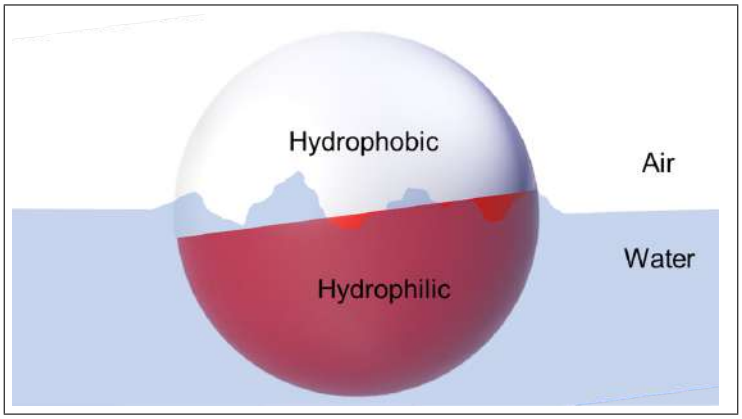

Figure 3.14: Scheme of Janus particle with undulations in its contact line.

In particular, Janus particles without charge are much more complicated, because the Janus boundary is not necessarily parallel to the interface [50], and this boundary can be at a different height with respect to the flat interface depending on the Janus balance, as can be seen in Fig.3.15. The tilted non-equilibrium orientations give rise to inter-particle interactions with a complex angular interaction and a pair potential inversely proportional to the third power of the inter-particle distance (capillary dipolar interaction)[51].

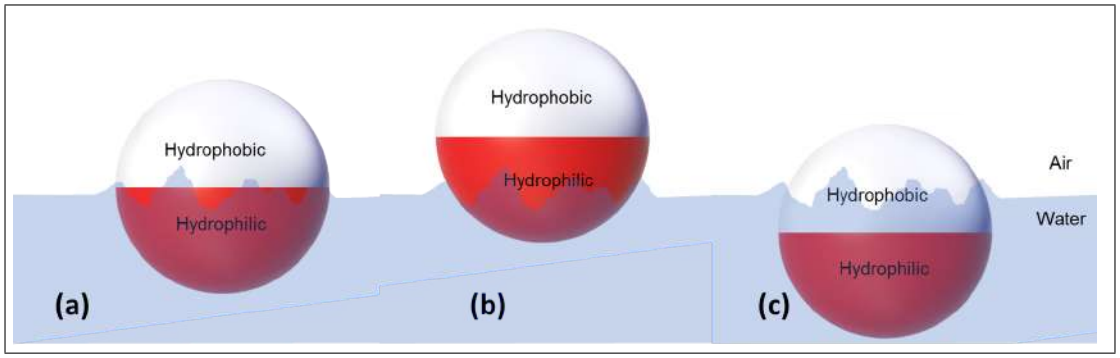

Figure 3.15: Scheme of Janus Balance. Janus balance depends on the respective areas of hydrophilic and hydrophobic chemical properties of the surface and the hydrophobicity of the two sides. (a) The equilibrium position of the Janus particle with a Janus boundary parallel to the interface. (b) and (c) Janus particles with the Janus boundary up or down, respectively, to the interface due to Janus's balance.

Experimental studies of the interface deformations due to the presence of particles are still an issue that has not been fully explored. There are only a few reports where the contact line shapes for Janus particles at oil/water interfaces [57], ellipsoidal Janus particles at air/water interfaces [58] and spherical particles trapped in thin membranes [59] using interferometry are studied. The self-assembly of particles at interfaces is of great interest due to all its applications. This phenomenon has been well studied, both experimentally and theoretically, for homogeneous particles. However, there are several questions about the possible ordering and effective interactions between inhomogeneous particles, such as Janus particles, trapped at fluid interfaces.

Most of the reports found in the literature dealing with Janus particles at fluid-fluid interfaces have focused on the theoretical calculations and simulations describing the detachment energy and also on the interfacial phenomena at the macroscopic

scale such as emulsion stabilization [53], [54]-[56]. Park and collaborators reported the only one experimental study on interactions between spherical Janus particle pairs at a fluid interface to our knowledge at the moment of writing this doctoral thesis. Park *et al.* [57] investigated the behavior of Janus particles at a water/oil interface. The Janus particles were made of polystyrene (Ps) particles of 2.9 μm in diameter with a hemisphere cover with gold ($Au-Ps$). They observed the orientation of amphiphilic Janus particles with respect to the oil/water interface. The also noted that the wettability of the gold hemisphere significantly influences the orientation of Janus particles. About 30% of $Au - PS$ particles were seen to have random orientations ($Au - Ps$ particles were observed using Scanning Electron Microscopy (SEM) and a gel trapping technique, Fig. 3.16): the Janus boundary of some Au-PS particles was tilted to the water/oil interface, and some Janus particles had the gold hemisphere completely submerged in the water phase.

Park *et al.* estimated the magnitude of the interface deformation by measuring the capillary forces between pairs of Janus particles. The interparticle force, F_{inter}, was determined based on the following force balance: $F_{inert} = F_{drag} + F_{inter} + F_{fluc}$, where the inertial force, F_{inert}, and the thermal force, F_{fluc}, are negligible. Electrostatic interaction and van der Waals interaction possibly contributed to the overall interparticle force, F_{inter}. However, these two forces are negligible compared to the capillary forces in the case of interface-trapped Janus particles. The interparticle force was determined with the drag force, F_{drag}, at each distance r. They used particle trajectory analysis. So the velocity U was measure to get the drag force later, given as $F = -6\pi a \eta_{eff} U$, with η_{eff} is the effective viscosity in the oil/water interface and defined as $\eta_{eff} = \frac{[\eta_{oil}(1-\cos\theta_c)+\eta_{water}(1+\cos\theta_c)]}{2}$. Here, the contact angle, θ_c, was measure by the gel trapping method used for the SEM images.

The forces between two particles obtained by Park *et al.* resulted in attractive

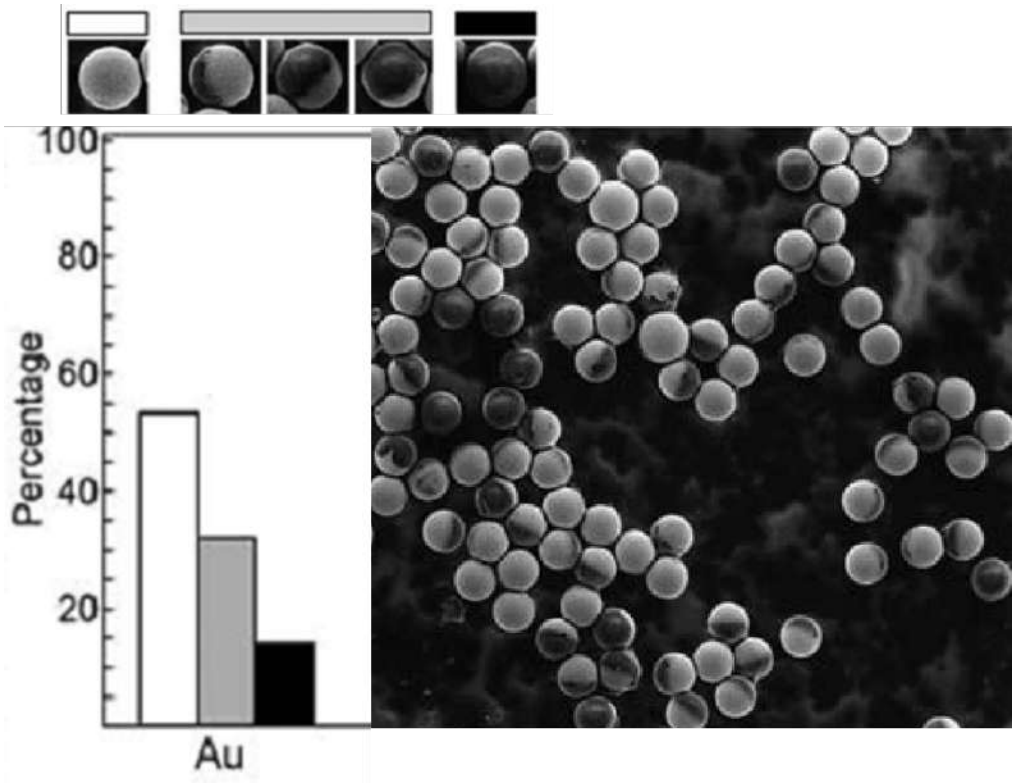

Figure 3.16: Histogram of the orientation of $Au - Ps$ particles (left), based on SEM images (right). White, gray, and black bars represent the fraction of Janus particles with its gold hemisphere in the oil phase, those with Janus boundary rotated out-of-plane of the water/oil interface, and those with the gold hemisphere in the aqueous phase, respectively [57].

forces that scale as $F \approx r^{-5}$, as shown in Fig. 3.17.

The authors stated that the slope of the curves in Fig.3.17 is -5, which corresponds to the quadrupolar capillary interaction due to the undulated contact line. They asserted that this attractive interaction is likely due to the pinning of the contact line around the diffuse boundary between the two hemispheres of the Janus particles. Authors were able to calculate the meniscus height from their results as 70 μm. This value obtain by Park and Furst for hydrophobic particles of nearly the

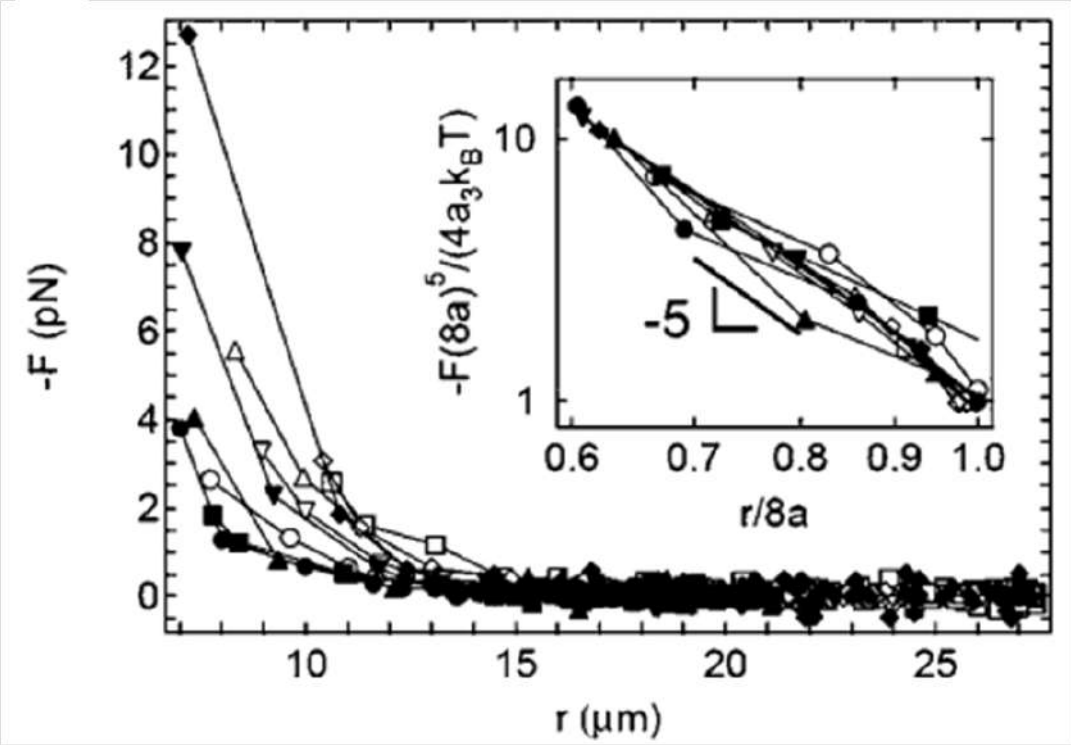

Figure 3.17: Measurements of attractive interactions between two Janus particles at the oil–water interface by [57]. Insets indicate that the measured force decays as $F \approx r^{-5}$.

same diameter is almost half the value obtained by Park *et al.* (45 μm). Nonetheless, the slope values of the curves in Fig. 3.17 can be approximated to ≈ -5, and also to ≈ -6 and also to ≈ -4 and any number in between. The curves have a great fluctuation in the exponent (or slope in the inset) that could not be explained by the authors. The assumption of an effective viscosity, η_{eff}, along with the method to measure the interparticle capillary forces induce an error as the thermally activated fluctuations of the interface are not taken into account [14] neither the Janus balance and the role of the charge. With those results, more questions than answers

4. Experimental techniques

4.1 Optical trapping principles

The radiation pressure of light upon an object has been known since 1619 by J. Kepler. In *"De Cometis Libelli Tre"*, Kepler used the concept of radiation pressure to explain why the direction of comets tails are away from the sun. In 1871 J. C. Maxwell described the radiation pressure as the change in momentum between light and the objects [63]. Even though light — electromagnetic waves in general — does not have mass, it carries momentum. The force exerted by light when striking upon an object surface is a consequence of the conservation of momentum, and it is experienced as radiation pressure. The change of momentum per unit area or radiation pressure of the incident light, P_i, is given as the ratio between the energy flux carried by the wave, I, and its velocity, c,

$$P_i = \frac{I}{c} \tag{4.1}$$

The surface on which the incident light hits can totally or partially absorb or reflect it, depending on the surface properties. If the surface absorbs the incident light completely, then it is called a perfect absorber. And if the surface reflects the incident light totally, it is called a perfect reflector. The absorption or reflection of light brings in a change in pressure, P_{net}, that for the conservation of momentum and Newton's third law of motion, it gives rise to a force on the surface.

$$P_{net} = P_f + P_i = \begin{cases} \frac{I}{c} & \textit{(perfect absorber)} \\ \frac{2I}{c} & \textit{(perfect reflector)} \end{cases} \tag{4.2}$$

where P_f and Pi are the light pressures before and after the light has reached the surface, respectively. For partially absorbed or reflected light, the radiation pressure P_{net} lies between the two values in eq. 4.2. Thus, the force, F_r, on an area surface, A, due to the momentum of light hitting it can be obtained as $F_r = P_{net}A$. The same result is obtained if we consider photons instead of waves. If light with power P hits a surface, then $\frac{P}{h\nu}$ photons impinges such surface every second and transfer a total momentum of $(\frac{2P}{h\nu})(\frac{h\nu}{c}) = \frac{2P}{c}$ on it. So, as calculated by Ashkin, a light source of $P = 1\ W$ should produce a force of $\approx 10\ nN$ if the surface is perfectly reflective. For objects and light sources in everyday life circumstances, forces are so weak that they are not noticeable.

However, pressure forces become relevant as the surfaces on which light impinges are reduced in size to the order of microns. In 1970, Arthur Ashkin published the first successful attempt to accelerate and trap micron-sized particles by radiation pressure [64]. He used latex spheres of different diameters suspended in water. Then, he positioned a TEM_{00}-mode laser beam of an argon laser horizontally through the cell containing the particles and used a microscope to observe the experiment. Ashkin noticed that when the beam was focused on one single particle, this was attracted to the beam center, then pushed and accelerated in the light direction (Fig. 4.1) until the particle reached the glass of the cell and remained there as long as the beam was not switched off.

In Ref. [64] Ashkin also reported the trapping of similar particles with two equal TEM_{00} counter-propagating laser beams (shown in Fig. 4.2). He was able to trap

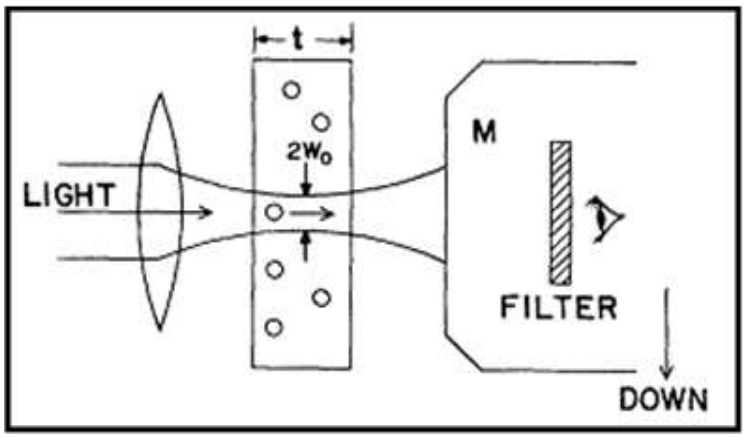

Figure 4.1: Sketch of Ashkin's set up to observe the motions of particles in a focused laser beam [64]. The laser beam was focused by a lens which focal point coincides with the cell center. The cell containing the particles had a width of t. The light travels from left to right, as indicated by the rows. When the beam was focused on one single particle, this particle was attracted to the center of the beam and then pushed and accelerated in the direction of the light. The particle was observed with a microscope (M). The gravitational force is directed downward. This is, perpendicularly to the direction of propagation of the laser beam, as shown in the figure.

particles in a stable way using the radiation pressure of light. From these first successful attempts in trapping small objects with light, others followed, showing the possibilities of these new techniques [65],[66],[67]. In 1986 Ashkin and collaborators attained the trapping of dielectric particles with a single laser beam in three-dimensional space [68].

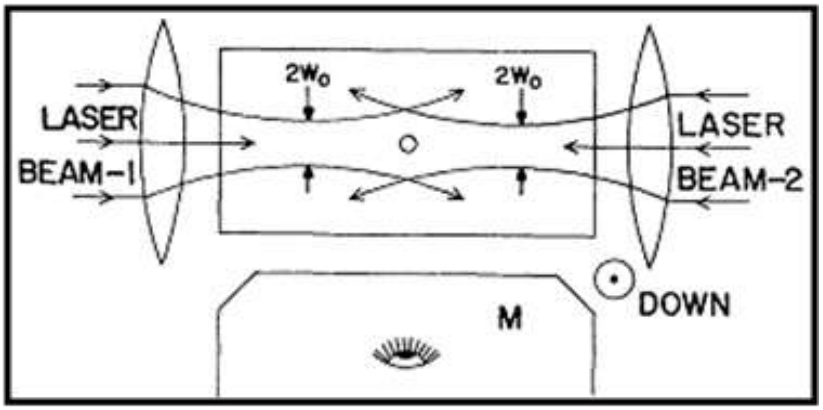

Figure 4.2: Two counter-propagating laser beams trapping a particle in Ashkin's experiments [64]. Both laser beams were focused using a lens. The observations were made with a microscope, M. The gravitational force direction is perpendicular to the direction of propagation of the laser beam, inward to the page in the figure, denoted by the dot in the circle. The particle was trapped in the center of the two beams.

Ashkin *et al.* used a strongly focused laser beam to trap a dielectric particle with the experimental setup described in Fig. 4.3, generating two types of forces acting on the particle: A gradient and a scattered force. Both of these forces are explained below. Ashkin's work was the turning point in the development of a powerful tool with a wide range of applicability.

The basic idea behind optical trapping is to have a highly focused laser beam to get the confinement and control of microscopic objects with sizes ranging between $\approx 10\ nm$ to $\approx 10\ \mu m$. When a particle is put in the laser beam's focus, the photons of the light hit it: the particle scattered some photons and absorbs others. As a result, there is a transfer of momentum to the particle from the incident photons. For particle sizes of some microns, the phenomenon can be explained in terms of ray op-

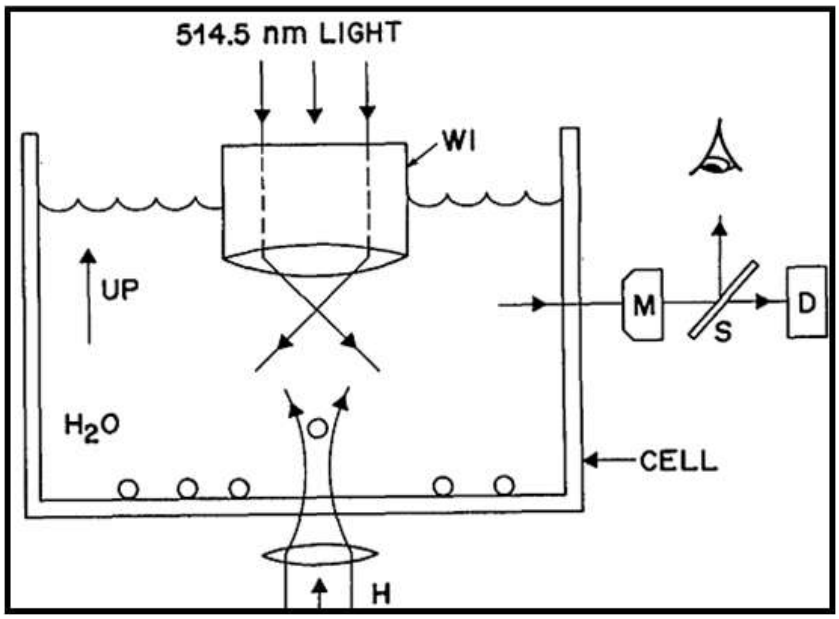

Figure 4.3: Sketch of the experimental set up used for Ashkin to confine particles in a single beam trap [68]. Laser light of 514.5 nm is strongly focused by a high numerical aperture microscope objective(WI). The objective focuses the beam downward-directed into a water cell where the particles are immersed. The particles are carried to the objective focus with an auxiliary beam (H) from the bottom of the cell. To observe the experiment was used a microscope M, or it was recorded with a detector D.

tics. But as the particle diameter is smaller than the wavelength of the light used for trapping, the forces no longer can be obtained in the same theoretical frame. There can be distinguished two limiting cases for which optical trapping forces are understood and have an analytical expression [69],[70], depending on the relative size of the particle and the wavelength of light: (a) Rayleigh regime or dipole approximation regime and the (b) geometrical regime or ray optics regime.

4.1.1 Rayleigh regime

This regime applies when the particle is an order of magnitude smaller than that of the wavelength of light, λ. In this case, the particle is considered a point dipole embedded in an inhomogeneous electromagnetic field of the laser beam that interacts. If particles are dielectric, then a classical approach is needed. For the trapping of molecules or atoms, a semi-classical approach should be followed. To get a general expression for dielectric particles, we consider a dipole consisting of two opposite charges at a distance d from each other, of mass M_1 and M_2, that is interacting with an external electromagnetic field, $\vec{E}$ and $\vec{B}$. From the motion equations for the dipole, the electric field can be expanded around each charge position with a Taylor expansion as:

$$\vec{E}(\vec{r}) = \sum_{n=0}^{\infty} \frac{1}{n!} \left[(\vec{r}_1 - \vec{r}) \cdot \nabla\right]^n \vec{E}(\vec{r}) \tag{4.3}$$

where $\vec{r}$ and $r \vec{-} 1$ are the center of mass coordinate and the position of one charge, respectively. The same calculation can be done for the other charge. As for the required condition is $d = |\vec{r}_1 - \vec{r}_2| \ll \lambda$ the expansion can be truncated at the second term (dipole approximation). Using the definition for dipole moment, $\vec{p} = q\vec{d}$, the total force $\vec{F} = (M_1 + M_2)\ddot{\vec{r}}$ yields to

$$\vec{F} = (\vec{p} \cdot \nabla)\vec{E} + \dot{\vec{r}} \times (\vec{p} \cdot \nabla)\vec{B} + \dot{\vec{p}} \times \vec{B} \tag{4.4}$$

Eq. 4.4 has three terms, the first two originate due to the interaction between the dipole and the inhomogeneous electromagnetic field, and the last one is due to the Lorentz force. The second term is almost always minimal compared with the others and can be neglected. The last term in the equation can be rewritten and

approximated becoming as

$$\vec{F} = \sum_i p_i \nabla E_i + \frac{d}{dt}\left(\vec{p} \times \vec{B}\right) \tag{4.5}$$

where $i = x, y, z$, and the last term vanishes when the average over time (or ensemble average as the system is assumed ergodic) is computed,

$$\left\langle \vec{F} \right\rangle = \sum_i \langle p_i(t) \nabla E_i(t) \rangle \tag{4.6}$$

Eq. 4.6 is the average force due to radiation light field on the oscillating dipole. The electromagnetic field has a general expression given by $\vec{E}(\vec{r}, t) = \vec{E_0}(\vec{r})e^{-i\omega t}$ and $\vec{B}(\vec{r}, t) = \vec{B_0}(\vec{r})e^{-i\omega t}$. Where ω is the angular frequency of the field. Assuming a linear response between the dipole and the field, the the dipole oscillates at the same frequency ω as $\vec{p}(\vec{r}, t) = \vec{p_0}(\vec{r})e^{-i\omega t}$. The real part of this equation correspond to the dipole force or the gradient force mentioned by Ashkin. The imaginary part is the scattered and absorbed longitudinal component of the force. In the simplest case where the electromagnetic field has an angular frequency dependency, ω and has a linear relationship with the dipole then its moment is proportional to the electric field and can be written in terms of the polarizability α,

$$\vec{p} = \alpha(\omega)\vec{E}(\vec{r_0}) \tag{4.7}$$

For small particles in aqueous medium $\alpha(\omega)$, the polarizaility is approximately

$$\alpha(\omega) = \frac{\alpha_0(\omega)}{1 - (2/3)ik^3\alpha_0(\omega)} \tag{4.8}$$

where $\alpha_0(\omega) = a^3\frac{\epsilon-1}{\epsilon+2}$ is the Clausius-Mosotti relation. Substituting 4.8 into 4.6 and

taking the real part we get

$$\left\langle \vec{F}_{grad} \right\rangle = 2\pi n_m^2 \epsilon_0 a^3 \frac{m^2-1}{m^2+2} \nabla I(\vec{r}) \tag{4.9}$$

in which m is the ration between the refractive index of the particles, n_p and the medium, n_m. From eq. 4.9 can be noted that the gradient force depends on the gradient of the intensity of the light applied: particles feel a force in the direction of the high-intensity regions of the beam. As mentioned early, we can obtain the scattered-absorbed force from the imaginary part of eq. 4.6 and expressed in terms of absorbing, σ_{abs}, and scattering, σ_{scatt} cross-section as [71]

$$\vec{F}_{abs+scatt} = \frac{\vec{E}_0^2}{8\pi}(\sigma_{abs} + \sigma_{scatt})\frac{\vec{k}}{k} \tag{4.10}$$

and being

$$\begin{aligned} \sigma_{abs} &= 4\pi k a^3 Im\left\{\frac{\epsilon-1}{\epsilon+2}\right\} \\ \sigma_{scatt} &= \frac{8\pi}{3}k^4 a^6 \left(\frac{\epsilon-1}{\epsilon+2}\right) \end{aligned} \tag{4.11}$$

For most applications are used almost transparent objects, where the absorption is negligible, $\sigma_{abs} \approx 0$, so the total force in 4.10 is due to the change in the momentum of photons hitting the object when scattered. So,

$$\left\langle \vec{F}_{scatt}(\vec{r}) \right\rangle = \frac{8\pi n_m}{3c}(ka)^4 a^2 \left(\frac{m^2-1}{m^2+2}\right) I(\vec{r})\hat{k} \tag{4.12}$$

It is important to remark that the scattered force is in the direction of propagation of the incident light, $\hat{k}$. Furthermore, it highly depends on the wavelength through

$k = \frac{2\pi}{\lambda}$ and the intensity of the beam.

4.1.2 Geometrical approximation

This regime is applicable for objects that have a greater size compared to that of the wavelength of the light in use. In this case, the beam can be seen as a bundle of rays. For simplicity, we can consider a spherical particle with a greater refractive index than the medium displaced into the Gaussian beam axis. Let's consider two rays, 1 and 2, from the beam striking the spherical particle, as shown in Fig. 4.4. According to Snell's law, as the rays enter through the particle, they are refracted twice (when it enters the particle and when it leaves the particle). The final change of the direction of the rays (thus, the rays momentum) gives rise to a net force over the particle. Note that unlike in the Rayleigh regime, where the identification of gradient and scattered forces is clear, in geometric approximation cannot be made this distinction easily. Despite this, one can identify two forces: reflection forces and refraction forces. However, we can divide the net force acting on the particle into two components, one parallel to the direction of the incident rays propagation (due to any ray that has been reflected), and another perpendicular to it (due to any refracted ray). The parallel component can be recognized as the scattered force, and the perpendicular as the gradient force, in correspondence with the dipole approximation. The gradient force points toward the high-intensity region of the Gaussian beam.

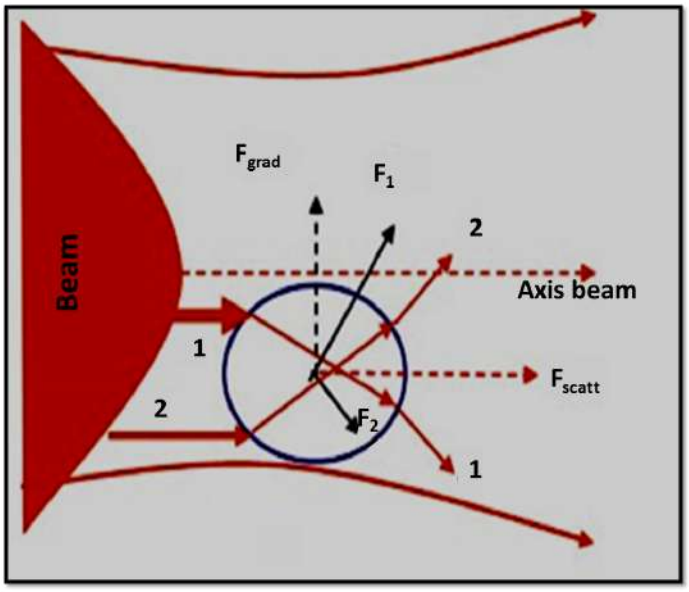

Figure 4.4: Sketch of forces acting on a spherical dielectric particle due to a strongly focused Gaussian beam (in red). The particle is placed slightly out of the axis of the beam. Net force due to the incident rays striking a spherical particle slightly displaced out of the beam axis. The gradient component of the force is towards the high-intensity profile of the beam.

When the rays reach the medium/particle interface, they are subjected to a reflection and a refraction. The refracted rays then travel through the particle until they reach the particle/medium interface occurring a new refraction and a new reflection, and so on, as can be seen in Fig. 4.5. If the ray striking on the sphere has power P and an angle θ, such ray carries momentum $\frac{n_m P}{c}$, where again n_m is the refractive index from the medium. We can calculate the total force acting on the sphere due to the ray with Fresnel equations for reflection and transmission. The coefficient for transmission T and reflection R vary from 0 to 1, depending if the

the ray is completely reflected ($R = 1$, $T = 0$) or completely transmitted ($R = 0$, $T = 1$). The sum of the power of the first refraction, PR, and the infinite number of refracted rays of successively decreasing power PT_2, PT_2R,..., PT_2R_N (as described in Fig.4.5) gives us the total force acting on the sphere [69].

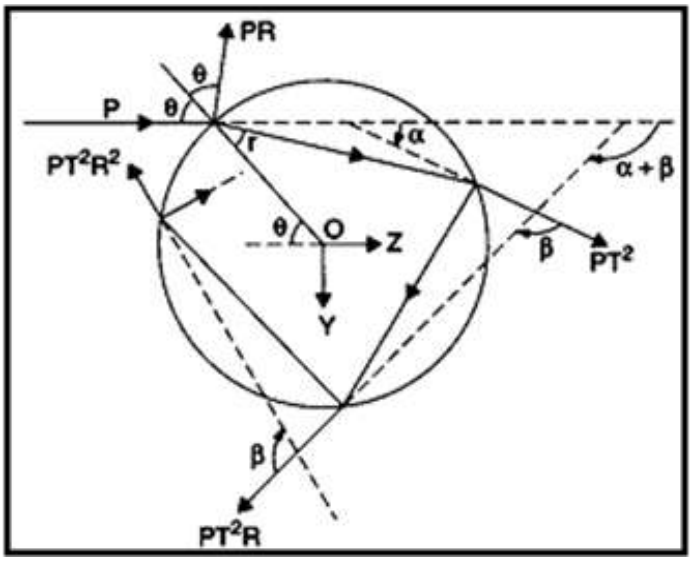

Figure 4.5: Multiple partial refractions from an incident ray at particle/medium interfaces [69]. An incident ray of power P hits a spherical particle. The ray is partially reflected (PR) with an angle θ and partially refracted into the particle with an angle r. Once encountering the particle/medium interface, the refracted ray is again partially refracted (PT^2) and partially reflected inside the particle. The partial rays refraction and reflection process repeats infinitely.

$$F_{scatt} = \sum_{i}^{N} \frac{n_m P_i}{c} \left[1 + R_i \cos(2\theta_{R_i}) - \frac{T_i^2 \left[\cos(2\theta_{R_i} - 2\theta_{T_i}) + R_i \cos(2\theta_{R_i}) \right]}{1 + R_i^2 + 2R_i \cos(2\theta_{T_i})} \right] \quad (4.13)$$

$$F_{grad} = \sum_{i}^{N} \frac{n_m P_i}{c} \left[1 + R_i \sin(2\theta_{R_i}) - \frac{T_i^2 \left[\sin(2\theta_{R_i} - 2\theta_{T_i}) + R_i \cos(2\theta_{R_i}) \right]}{1 + R_i^2 + 2R_i \cos(2\theta_{T_i})} \right] \quad (4.14)$$

In equations 4.13 and 4.14 are dependent of polarization because R y T differ if the light is parallel or perpendicular polarized respect to the plane of incidence. If the particle refractive index is smaller than the refractive index of the medium, the scattered force is greater than the gradient force, and the particle is pushed away from the high-intensity region of the beam. If, on the other hand, the refractive index of the particle is higher than the medium refractive index, then the predominant force is the gradient force, and the particle is attracted to the high-intensity zone of the beam. This attraction causes the particle trapping in two dimensions, but the particle is still being pushed away, as observed by Ashkin. However, to achieve three-dimensional trapping, there is no need to have two counter-propagating beams as Ashkin did, but a highly focused beam. Very focused rays would have very high incident angles, which means a strong gradient force that surpasses the scattered forces, resulting in the trapping of the particle at the focus of the beam. As could be seen, it is possible to trap particles of different sizes using light. The complexity of the setup design necessary to accomplish optical trapping depends on the size and material of the object and the medium.

When the particle is not embedded in the bulk of a liquid but straddled at a fluid interface, the same principle of trapping applies.

But for micron-sized particles in a liquid and trapped by optical tweezers are also subjected to another phenomenon: Brownian motion. To successfully carry out optical trapping is required the gradient forces to be greater than thermal driven forces. The next section analyzes the behavior of a trapped spherical particle in the

presence of Brownian motion.

4.2 Dynamics of a particle trapped at the air-water interface and under a harmonic potential

As seen in the last section, the gradient force in optical trapping provides the restoring action, which pulls the particle towards the center of the trap. This behavior can be taken as the restoring force of a spring, and its energy can be approximated to a harmonic potential. Also, because the particle is suspended in a liquid interface, it presents Brownian motion due to its size. Hence, the particle dynamic can be described with the Langevin equation.

$$m\dot{v} = -kx - \alpha v + F_s(t) \tag{4.15}$$

where v is the instantaneous velocity, $-kx$ is the force of the harmonic potential, αv is the friction force. $F_s(t)$ is a stochastic force due to the random fluctuations of the density of the fluid. The Langevin equation is a stochastic equation that describes the Brownian motion, with apparently random movement.

In this section, we focus on calculating the mean square displacement (MSD) from the Langevin equation. To achieve this, we obtain the velocity autocorrelation function ($VACF$) of the Brownian particle first. And then, using the $VACF$, one can find the mean square displacement (MSD). MSD measures the deviation in time of the position of the particle from a reference position, and it is related to other quantities of our interest, as is mentioned later. To calculate the $vacf$ we rewrite the

Langevin equation as

$$\dot{v} + \omega_0^2 x + \gamma v = f_s(t), \tag{4.16}$$

with $\omega_0^2 = \frac{k}{m}$, $\gamma = \frac{\alpha}{m}$ and $f_s(t) = \frac{1}{m}F_s(t)$.

To simplify equation 4.16 is necessary to rewrite it in terms of the instantaneous velocity and its derivatives.

In doing so, the Langevin equation takes the following form:

$$\dot{v} + \omega_0^2 \int_0^t v(\tau)d\tau + \gamma v = f_s(t) \tag{4.17}$$

Now we multiply equation 4.17 by $v(0)$ and take the average over time or ensemble. We get

$$\langle \dot{v}v(0) \rangle + \omega_0^2 \int_0^t \langle v(\tau)v(0) \rangle \, d\tau + \gamma \langle vv(0) \rangle = \langle f_s(t)v(0) \rangle$$

The stochastic force is independent of the particle velocity then $\langle f_s(t)v(0) \rangle = 0$. Furthermore, to simplify the equation, we rewrite $VACF$ as $\langle vv(0) \rangle = c_{vv}$ and $\langle \dot{v}v(0) \rangle = \dot{v}_{vv}$. We get:

$$\dot{c}_{vv} + \gamma c_{vv} + \omega_0^2 \int_0^t c_{vv}d\tau = 0 \tag{4.18}$$

The solution to equation 4.18 can be easily found using its Laplace transformation.

$$\mathscr{L}\{\dot{c}_{vv}\} + \mathscr{L}\{\gamma c_{vv}\} + \mathscr{L}\left\{\omega_0^2 \int_0^t c_{vv}d\tau\right\} = 0$$

which leads us to

$$s\tilde{c}_{vv} - c_{vv}(0) + \gamma\tilde{c}_{vv} + \omega_0^2\frac{\tilde{c}_{vv}}{s} = 0$$

Considering that $c_{vv}(0) = \langle v(0)v(0)\rangle = \langle v^2(0)\rangle$ and $\frac{1}{2}m\langle v^2\rangle = k_BT$, then

$$s\tilde{c}_{vv} - \frac{k_BT}{m} + \gamma\tilde{c}_{vv} + \omega_0^2\frac{\tilde{c}_{vv}}{s} = 0$$

$$\tilde{c}_{vv} = \frac{k_BT}{m}\frac{s}{[s^2 + \gamma s + \omega_0^2]}$$

And solving by factorizing the denominator of the last equation

$$s^2 + \gamma s + \omega_0^2 = s^2 + \gamma s + \frac{\gamma^2}{4} + \omega_0^2 - \frac{\gamma^2}{4} = \left(s + \frac{\gamma}{2}\right)^2 + \left(\omega^2 - \frac{\gamma^2}{4}\right)$$

$$= \left(s + \frac{\gamma}{2} + i\sqrt{\omega_0^2 - \frac{\gamma^2}{4}}\right)\left(s + \frac{\gamma}{2} - i\sqrt{\omega_0^2 - \frac{\gamma^2}{4}}\right)$$

The result of the Laplace transformation of the $VACF$ is given as

$$\tilde{c}_{vv} = \frac{k_BT}{m}\frac{s}{(s - s_1)(s - s_2)}, \tag{4.19}$$

where $s_1 = -\frac{\gamma}{2} \pm i\omega$ y $\omega = \sqrt{\omega_0^2 - \frac{\gamma^2}{4}}$.

The inverse Laplace transformation gives this solution. To have the solution in terms of the original variables, we take the inverse Laplace transformation of eq. 4.19. To do this, we use the partial fractions decomposition method, and we obtain

$$\frac{s}{(s - s_1)(s - s_2)} = \frac{A}{(s - s_1)} + \frac{B}{(s - s_2)} \rightarrow (A + B)s - (As_2 + Bs_1) = s$$

Thus,

$$B = 1 - A; \qquad \frac{\gamma}{2}B - iB\omega + \frac{\gamma}{2}A + iA\omega = 0$$

$$c_{vv}(t) = \frac{k_B T}{m}\left[Ae^{-\frac{\gamma}{2}t}e^{i\omega t} + Be^{-\frac{\gamma}{2}t}e^{-i\omega t}\right]$$

$$c_{vv}(t) = \frac{k_B T}{m}e^{-\frac{\gamma}{2}t}\left[\cos(\omega t) - \left(\frac{\gamma}{2i\omega}\right)i\sin(\omega t)\right]$$

$$c_{vv}(t) = \frac{k_B T}{m}e^{-\frac{\gamma}{2}t}\left[\cos(\omega t) - \left(\frac{\gamma}{2\omega}\right)\sin(\omega t)\right] \tag{4.20}$$

Equation 4.20 is the resulted $VACF$. The next step necessary is finding the MSD, as mentioned at the beginning of the section. By definition, the MSD is given by:

$$MSD(t) = \left\langle [x(t) - x(0)]^2 \right\rangle \tag{4.21}$$

MSD in terms of the $VACF$ is expressed as:

$$x(t) - x(0) = \int_0^t v(\tau)d\tau$$

So we have the expression:

$$MSD(t) = \left\langle \left[\int_0^t v(\tau)d\tau\right]\left[\int_0^t v(\tau)d\tau\right]\right\rangle = \int_0^t d\tau \int_0^t d\tau' \left\langle v(\tau)v(\tau')\right\rangle$$

In general, the correlation functions are time-dependent, but in systems that are at equilibrium, such functions are only dependent on the time difference in which the correlations are evaluated. Thus,

$$MSD(t) = \int_0^t d\tau \int_0^t d\tau' c_{vv}(\tau - \tau')$$

To solve the integral in equation 4.2 we make a change in variable: $u = \tau - \tau'$ and $w = \tau'$, with the Jacobian matrix, $\mathbf{J} = \begin{pmatrix} \frac{\partial u}{\partial \tau} & \frac{\partial u}{\partial \tau'} \\ \frac{\partial w}{\partial \tau} & \frac{\partial w}{\partial \tau'} \end{pmatrix} = \begin{pmatrix} 1 & -1 \\ 0 & 1 \end{pmatrix}$. As the determinant of this matrix is 1 and $dvdw = d\tau d\tau'$, then the MSD is

$$MSD(t) = \int_0^t dw \int_{-w}^{t-w} du\ c_{vv}(u)$$

$$MSD(t) = \int_0^t du \int_0^{t-u} dw\ c_{vv}(u) + \int_{-t}^0 du \int_{-u}^t dw\ c_{vv}(u)$$

$$MSD(t) = 2\int_0^t (t-u)\ c_{vv}(u)du \tag{4.22}$$

Taking the Laplace transformation of 4.22 and using 4.19, we can have the solution.

$$\mathscr{L}\{MSD(t)\} = \mathscr{L}\left\{2\int_0^t (t-u)\ c_{vv}(u)du\right\}$$

$$\mathscr{L}\{MSD(t)\} = \frac{2\tilde{c}_{vv}}{s^2} \tag{4.23}$$

From this we obtain that

$$\mathscr{L}\{MSD(t)\} = \frac{2k_BT}{m}\frac{1}{s(s-s_1)(s-s_2)}$$

Following the same procedure for MSD as we did with $VACF$ we get

$$\mathscr{L}\{MSD(t)\} = \frac{2k_BT}{m}\left[\frac{A}{s} + \frac{B}{s-s_1} + \frac{C}{s-s_2}\right]$$

$$\mathscr{L}\{MSD(t)\} = \frac{2k_BT}{m}A\left\{1 + e^{-\frac{\gamma}{2}t}\left[\left(\frac{B}{A} + \frac{C}{A}\right)\cos\omega t - \left(\frac{C}{A} - \frac{B}{A}\right)i\sin\omega t\right]\right\}$$

Finally, the obtained MSD is

$$MSD(t) = \frac{2k_BT}{m\omega_0^2}\left[1 - e^{-\frac{\gamma}{2}t}\left\{\cos\omega t + \frac{\gamma}{2\omega}\sin\omega t\right\}\right] \tag{4.24}$$

The MSD of the particle position given in equation 4.24 has a constant term minus a term that vanishes as time goes to infinity. For short times the behavior is that of a damped harmonic oscillator. As $t \to \infty$, in contrast with free Brownian particles, the MSD of the particle approaches to a plateau value given by $\frac{2k_BT}{m\omega_0^2}$, regardless the dynamic regime, as can be seen in Fig. 4.6: For long times, the particle stops diffusing, just as expected for a Brownian particle that is confined by a potential.

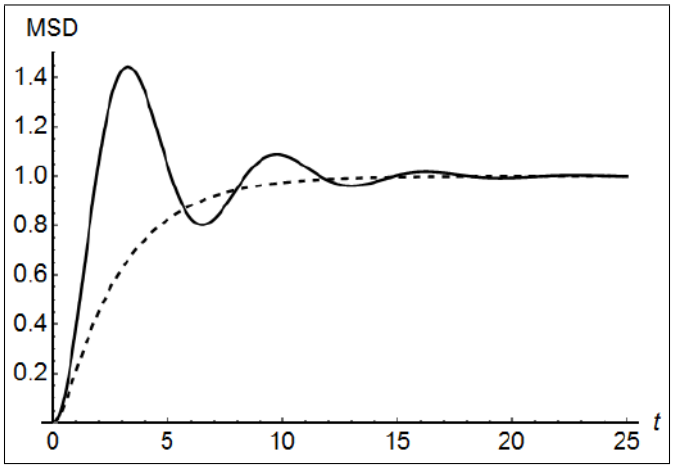

Figure 4.6: MSD for particles under the influence of a harmonic potential: Solid line corresponds to the underdamped case and dashed line for the overdamped case.

Furthermore, at equilibrium, the distribution of the MSD is Gaussian. The Smoluchowski equation is a differential equation that describes the time-evolution of the probability of finding a diffusing particle in a potential field, given its initial position. For a harmonic potential, the solution has a Gaussian shape.

The facts that the particle diffusion is a constant after *long* times and that it is at equilibrium are relevant for two main reasons here: (1) the calibration of the optical tweezers and (2) the measurement of the forces, as discussed in a further section.

Time-shared optical tweezers

As mentioned in Section 4.1, it is possible to trap and manipulate objects using a strongly focused light beam. The main component of optical tweezers is the microscope objective, which focuses the light beam. However, a simple setup for optical trapping only can trap and manipulate one object at a time. As optical tweezers can

measure displacements and forces with high precision and accuracy, it is an ideal tool to study interactions between colloidal particles at interfaces. As the main goal in this work is to measure capillary forces between two particles precisely, it is necessary to have a dual optical trap in which the separation of the two traps can be accurately controlled. We built a time-shared optical tweezers to accomplish this task.

Time-shared optical traps consist of a single laser beam that produces multiple traps in different points in space. These traps can be generated in various ways. The main idea is to pass the laser beam through an acousto-optic deflector that can produce many traps in different spatial points in a line (scanning line).

Acoustic-Optic Deflector An acoustic-optic deflector (AOD) has a transparent crystal to which an acoustic wave is applied using a piezoelectric. This acoustic wave induces a redistribution in the density of the material: the crystal has a high-density region followed by a low-density region repeatedly. This redistribution in the crystal density produces a pattern that acts as a diffraction grid of size Λ (as shown in Fig. 4.7). When a light beam passes across the crystal, the light is diffracted. The first-order diffracted ray (the zeroth-order ray suffers no diffraction) has a deflected angle, θ_{sep}, that depends on the acoustic frequency of the piezoelectric $\theta_{sep} = \frac{\lambda f}{v}$, where λ is the wavelength of the beam light, f and v are the frequency and velocity of the acoustic wave, respectively.

The diffraction efficiency is proportional to the grid size, and thus to the amplitude of the acoustic wave produced. The maximum deflection of an AOD is linearly related to the frequency interval in which it operates.

To control the size of the diffraction grid, and hence to change the deflected angle of the input beam, θ_{sep}, we change the frequency of the acoustic wave. Once the first diffraction ray is set, we can vary the acoustic wave frequency to change

the diffraction angle again. If we do change between two or more acoustic frequency waves, we can spot the beam focus in different points in space, creating a scanning like trap. When the variation of the acoustic frequencies is faster than the Brownian motion of the particles trapped, it creates the illusion of having many traps at the same time in different space points.

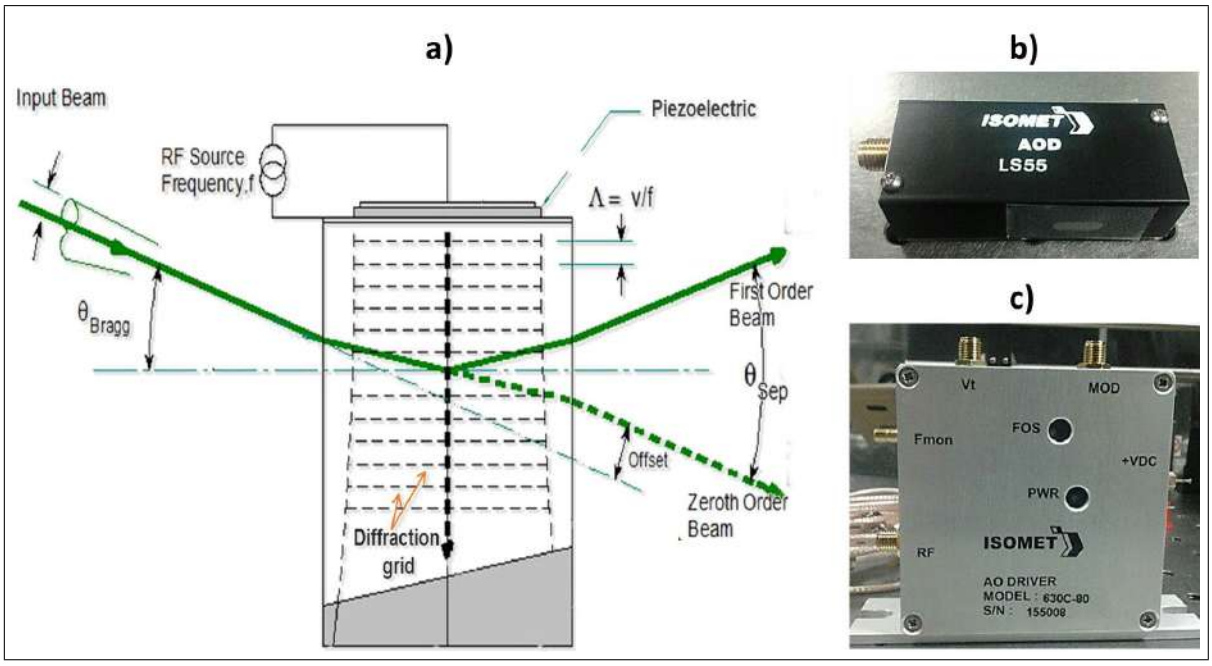

Figure 4.7: a) Schematic diagram of *AOD*. An acoustic wave is applied through the crystal using a piezoelectric. The acoustic wave produces a redistribution of the crystal density: there is a high-density region followed by a low-density region repeatedly. This pattern acts as a diffraction grid. When a light beam enters through the crystal of the *AOD* in an angle, $\theta = \theta_{Bragg}$ (θ_{Bragg} is the Bragg angle), the beam is diffracted. The first-order diffracted ray (the zeroth-order ray suffers no diffraction) has a deflected angle, θ_{sep}. If this diffracted angle is changed rapidly (by changing the acoustic wave frequency), it creates the illusion of having many traps at the same time in different space points. b) ISOMET *AOD* used in the experimental setup. c) *AOD* driver sends the acoustic wave from a device generating it to the deflector.

4.3 Experimental Setup

The experimental optical setup is shown in Fig. 4.8. A linearly polarized beam from a 514.5 nm Argon laser (Spectra-Physics) passes through a quarter-wave plate or retarder (to convert linear polarized light into circularly polarized light, as required for efficiency for the AOD). Then, the beam is split into two beams by the AOD: the zeroth-order diffracted ray (not shown), and the first-order diffracted ray. The first order ray is the main beam used to create the optical tweezers, and the zeroth-order is blocked as it has no other purpose in the optical design. In the following description, the first-order ray is referred to simply as the beam. The beam passes through a double telecentric ($L1$ and $L2$). This system creates a collimated beam centered in the back aperture of a microscope objective with a numerical aperture of $NA = 0.7$ (Mitutoyo $100x$, 3 mm working distance). The objective focuses the beam into the sample. The beam overfills the back aperture of the microscope objective to obtain optimal trapping efficiency. The sample is placed in a Langmuir trough mounted on a precision stage that allows controlling the position of the sample. Cold light and lenses are used to illuminate the sample from the opposite side of the objective. The image and the trapping laser paths are separated with a dichroic mirror and captured by a CCD camera after filtered. To create the two traps, we change the acoustic wave signal at a velocity of 80 kH in the AOD using a wave generator, a signal amplifier, and an oscilloscope, as mentioned before.

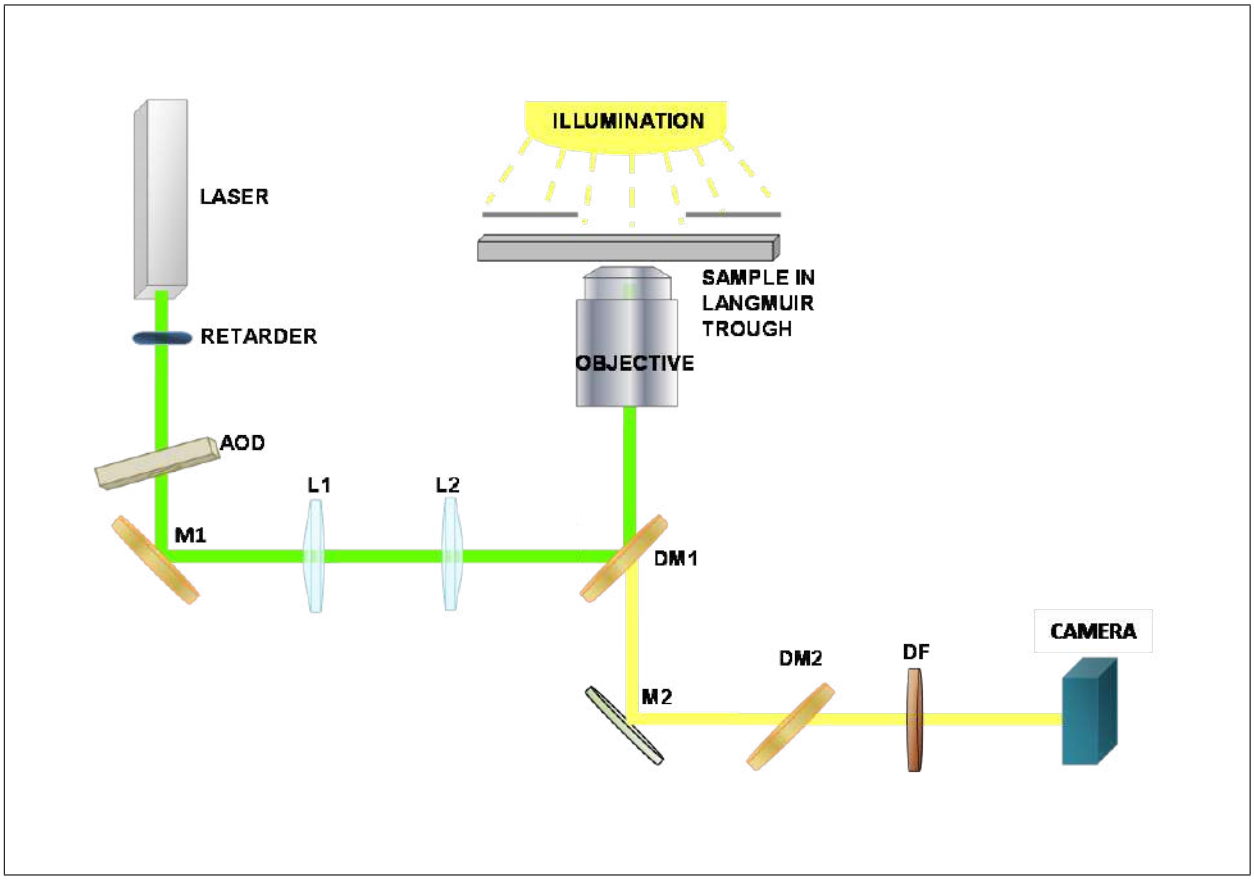

Figure 4.8: Schematic diagram of the experimental setup. The laser beam is converted into a circularly polarized beam by a retarder and diffracted by an AOD. The first-order beam is redirected by a mirror ($M1$) through a double telecentric ($L1$ and $L2$) and then sent to the back aperture of a microscope objective. The objective focuses the beam into the sample placed in a Langmuir trough. The filtered sample image is created through the objective and directed to a CCD camera for recording.

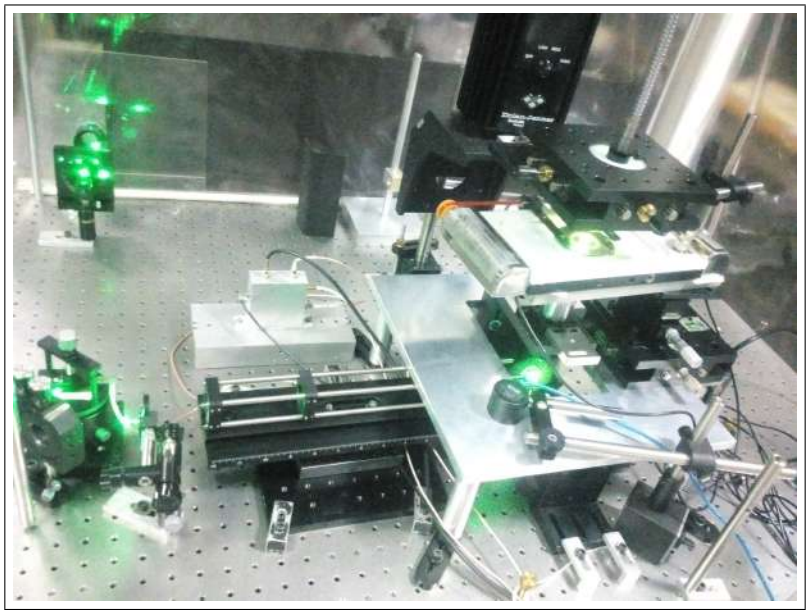

Figure 4.9: Time-shared optical tweezers setup used to measure capillary forces between colloidal particles at the air/water interface.

4.3.1 Calibration

Calibration of the optical tweezers is another crucial step in getting precise measurements.

Calibration gives us the trap stiffness and the force (which depends on the intensity of the beam) that the tweezers exert over the particle. The calibration methods can be separated into two categories: (1) passive method and (2) active methods. In passive methods, the trajectory of the trapped particle is tracked while the optical trap remains fixed. In active calibration techniques, it is measured the effect of a known optical force over the trapped particle, commonly applying a fluid flow.

A passive technique was used to calibrate the optical tweezers: the Boltzmann statistic distribution method. This method consists of constructing a histogram from

position fluctuations of the particle due to the presence of Brownian motion. Then, from that histogram, we can obtain the distribution position plot. The positions of a Brownian particle under a harmonic potential at equilibrium obeys a Boltzmann distribution. Hence, we can fit a curve described by 4.25.

$$\rho(x)dx \propto exp\left(\frac{-E(x)}{k_B T}\right). \tag{4.25}$$

Where $\rho(x)$ is the probability density of finding the particle with energy $E(x)$ in dx. Therefore,

$$E(x) = -ln\left(\rho(x)\right). \tag{4.26}$$

As the optical trap is generated by a Gaussian beam, the fitted curve can be simplified as a parabola, $y = ax^2 + b$, in the central region of the distribution curve. Then, the stiffness constant is calculated as $k = \frac{2a}{k_B T}$.

The advantages of this calibration method are that the particle size is not needed and that the actual shape of the trap can be known [85].

A precise value of k is obtained when we consider that the constant has two components in the interface plane, where particles are confined: k_x and k_y in the x and y axis, respectively. The interface itself restricts movements perpendicular to the interface. Optical traps (and thus, their stiffness constants) can be approximated as a superposition of three harmonic forces acting perpendicular to each other [86]. So, we can construct a curve like 4.25 for each axis separately to find k_x and k_y. The force exerted by the trap imposes an additional deviation on the particles towards the trap center. Thus, MSD can be used as a calibration standard for the position detection system in the presence of force fields. The reconstructed histograms for the x axis displacement for a particle of 3 μm in diameter with two different laser

powers are shown in Fig. 4.10. The same result can be achieved for the y axis. Note that the histogram width decreases with increased lase power, which means that as the laser power increases, the particle center can explore less volume.

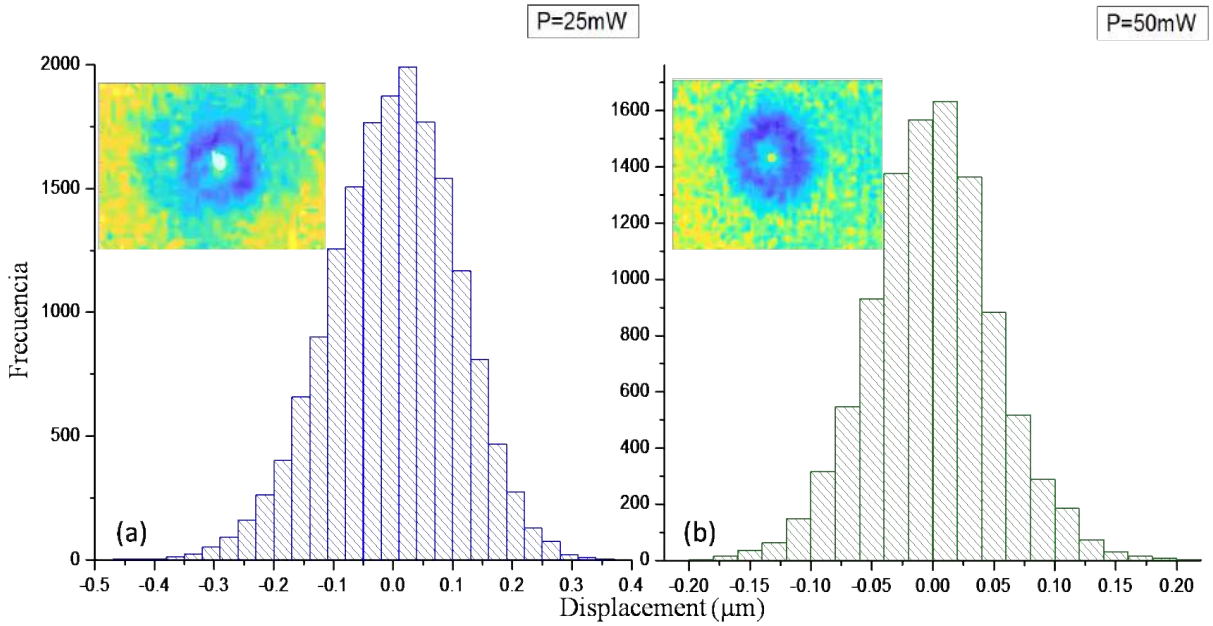

Figure 4.10: Reconstructed histogram in the x axis for particles of 3 μm in diameter optically trapped with a laser power of (a) $25mW$ and (b) $50mW$. The inset images are trapped particle snapshots in which is shown its center trajectory traced during the tracking.

A distribution plot can be obtained from the histogram to fit a Gaussian in the form of 4.25. The k_x value can be found for each desired value of laser power. An example of the fitting is shown in Fig. 4.11 for the cases above mentioned.

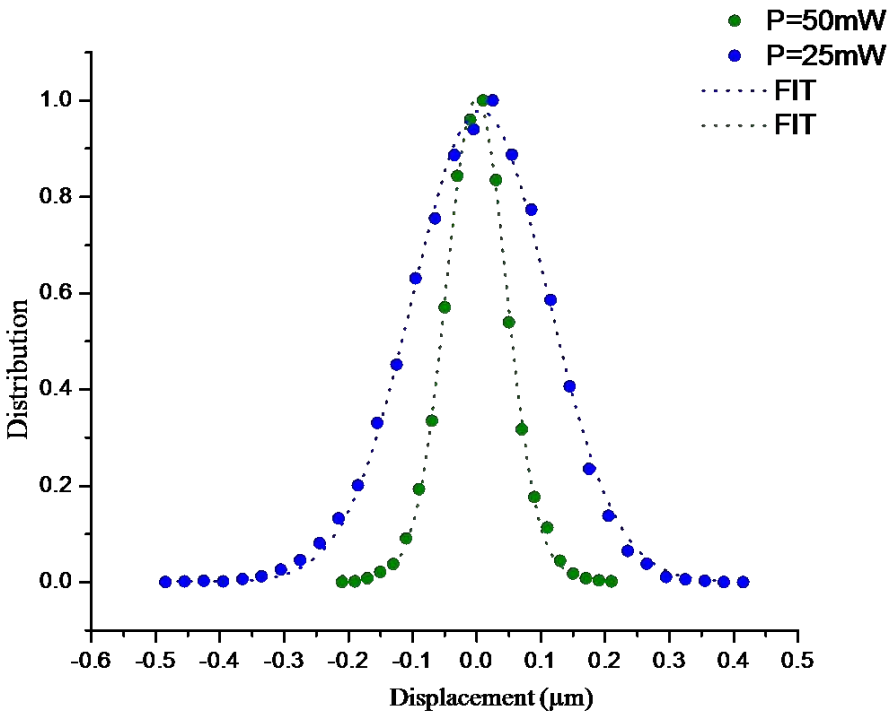

Figure 4.11: Distribution plot for the cases shown in Fig. 4.10. Dots correspond to the experimental data. Dotted lines correspond to the fitting.

If the process is repeated for different laser power values, the result is the calibration curve for the optical trap; this is the relation between laser input power and trap stiffness, as shown in Fig. 4.12. For small laser input powers, the constant stiffness value is directly proportional to the input power. Worth mentioning is that this calibration curve is particle size-dependent, therefore for each particle diameter, a graph of this kind should be obtained.

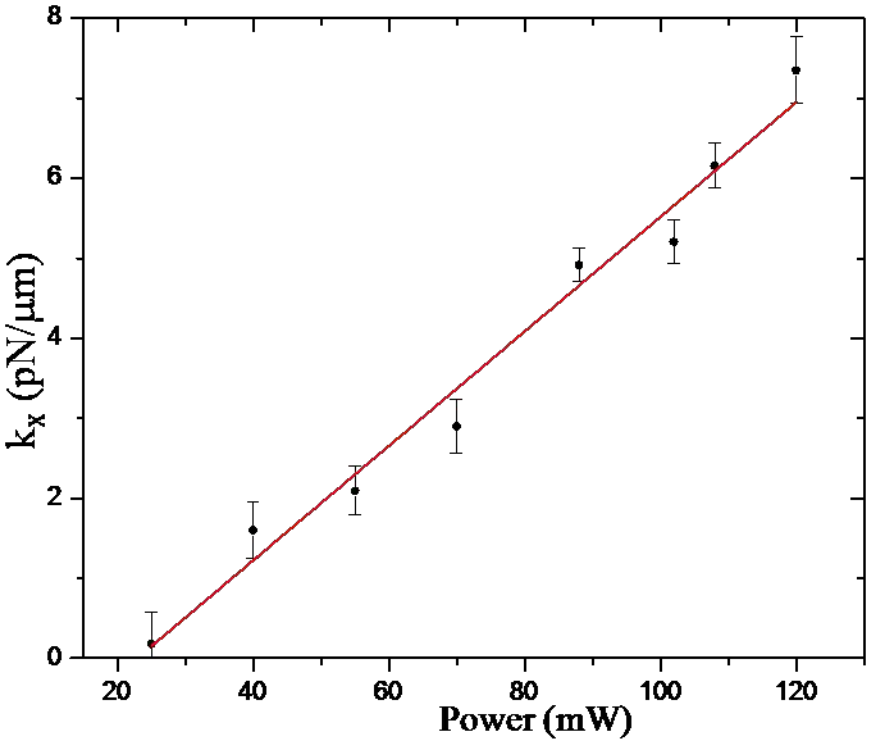

Figure 4.12: Optical tweezers calibration curve for k_x for silica particles of 3 μm diameter. Dots are experimental data, and the red line corresponds to a linear fitting. For relatively small laser power, there is a linear relation with the stiffness, as can be seen in this case. The correlation factor for the fit is $R = 0.967$.

4.4 Measurement of the force between two particles at an air-water interface trapped by a harmonic potential

The system under study consists of two colloidal particles constrained at an air-water interface and trapped by optical tweezers, i.e., a harmonic potential. Under the assumption that the particles interact with each other, the central purpose of this work is to measure and describe such interaction (Fig. 4.13). For clarity, we represented our system as a model consisting of two Brownian particles held by a spring. The particles interact between them. This model is schematized in Fig. 4.14.

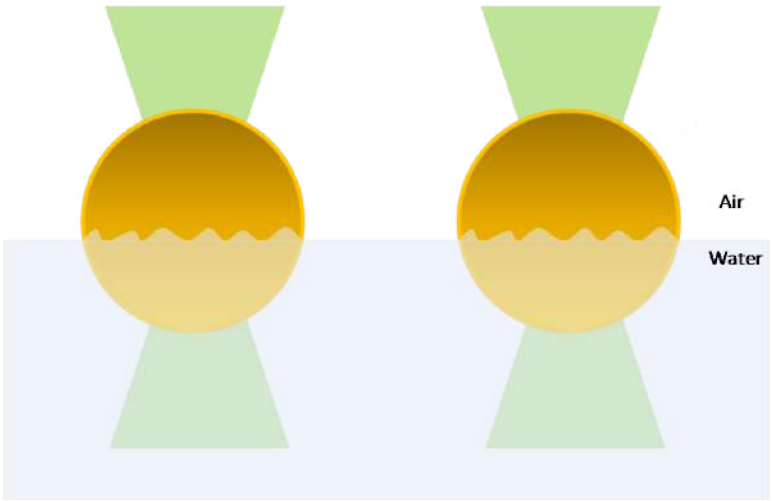

Figure 4.13: Schematic representation of the studied system. Two particles confined at a water/air interface are trapped by optical tweezers (in green). The particles present interaction between them.

To quantify the interaction force between the particles, we consider the model

depicted in Fig. 4.14. For simplicity, we choose the x axis as the displacement direction with respect to the equilibrium position. This choice is true in our case since the particles are limited to move in a plane parallel to the interface, and the interaction that we look for,F_α, is along a straight line joining their centers (x axis). The harmonic forces due to the springs are F_{r1} and F_{r2}, respectively, for each particle. The system can be described in terms of the total energy U_T that is the sum of the three potentials: $U_{r1}(\delta_1)$, $U_{r2}(\delta_2)$ and $U_\alpha(r)$ (Hooke's elastic potential of each trap and the interaction potential between the two particles, respectively).

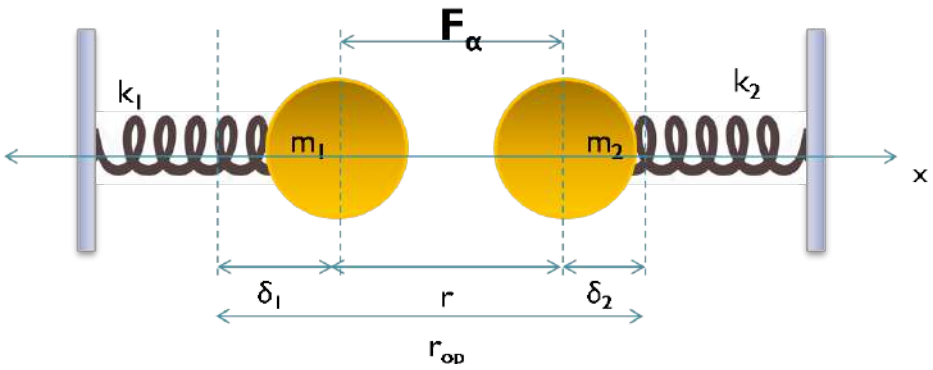

Figure 4.14: Two harmonic oscillators with Brownian motion and a mutual interaction force between them.

$$U_T = U_\alpha(r) + U_{r1}(\delta_1) + U_{r2}(\delta_2) \tag{4.27}$$

$$U_\alpha = U_T - \frac{1}{2}k_1\delta_1^2 - \frac{1}{2}k_2\delta_2^2 \tag{4.28}$$

Where r is the distance from center to center, k_1 and k_2 are the stiffness constants, δ_1 and δ_2 are the particle displacements from their equilibrium positions and r_{op} is the

distance between the equilibrium positions, the counterpart of the distance between the centers of the optical tweezers.

It is reasonable to assume a stationary condition for the system since, in the experiment, particles can be approached quasi-statically. Which leads to

$$\frac{\partial U_T}{\partial \delta_1} = \frac{\partial U_T}{\partial \delta_2} = 0 \tag{4.29}$$

The interparticle distance, r, is the difference of the distance of the equilibrium position, r_q, and the displacements from equilibrium, δ_1 and δ_2. This equivalence lets us express the potential generated by the particles in terms of the distances known in the experiment.

$$\frac{\partial U_T}{\partial \delta_1} = \frac{\partial U_T}{\partial \delta_2} = 0 \tag{4.30}$$

Replacing r as $r = r_q - \delta_1 - \delta_2$, we get that

$$\frac{\partial U_\alpha}{\partial \delta_1} = \frac{\partial U_\alpha}{\partial r}\frac{dr}{d\delta_1} \tag{4.31}$$

$$\frac{\partial U_\alpha}{\partial r}\frac{dr}{d\delta_1} = \frac{\partial U_\alpha}{\partial r}\frac{d(r_{op} - \delta_1 - \delta_2)}{d\delta_1} = -\frac{\partial U_\alpha}{\partial r} \tag{4.32}$$

$$\frac{\partial U_\alpha}{\partial \delta_1} = -\frac{\partial U_\alpha}{\partial r} \tag{4.33}$$

Otherwise we can write

$$\frac{\partial U_T}{\partial \delta_1} = \frac{\partial (U_\alpha + \frac{1}{2}k_1\delta_1^2 + \frac{1}{2}k_2\delta_2^2)}{\partial \delta_1} = \frac{\partial U_\alpha}{\partial \delta_1} + k_1\delta_1 = 0 \tag{4.34}$$

Finally, we obtain

$$\frac{\partial U_\alpha}{\partial \delta_1} = -k_1 \delta_1 \tag{4.35}$$

If we rewrite 4.35, then we can clearly see that the interaction force between the two particles is simply balanced by the exerted force by the optical trap on them.

$$F_\alpha = -k_1 \delta_1 \tag{4.36}$$

In terms of the stiffness constants of both optical traps, we have

$$k_1 \delta_1 = k_2 \delta_2 \tag{4.37}$$

$$\frac{k_1}{k_2} = \frac{\delta_1}{\delta_2} \tag{4.38}$$

$$\frac{k_1}{k_2} = \frac{r_q - r - \delta_1}{\delta_1} \tag{4.39}$$

as we know that $\delta_1 + \delta_2 = r_q - r$, so we can write again

$$F_\alpha = -k_1 \delta_1 = \frac{k_1 k_2 (r_q - r)}{k_1 + k_2} \tag{4.40}$$

If the two traps are generated with the same power beam, then their stiffness constants are the same, k, and equation 4.40 is reduced to $F_\alpha = \frac{k(r_q - r)}{2}$. Equation 4.40 tells us that to obtain the interaction force between the two particles, we need to measure the equilibrium positions, the displacement of the particles from the center of the optical tweezers, and the distances between them. [87].

5. Results and Discussion

5.1 Synthesis of colloidal particles

5.1.1 Hydrophilic Particles

Fused silica particles with a diameter of $3\mu m$ and $5\mu m$ (Bangs Laboratories, USA) were used. These particles are hydrophilic when acquired by the supplier. In this case, a modification is not necessary. Nevertheless, a cleaning process is mandatory to avoid possible contamination and induced effects by dirt. The cleaning process was made suspending the particles in 5 ml of a solution of sulfuric acid (H_2SO_4) with hydrogen peroxide (H_2O_2 aqueous) at 50% volume in a centrifuge tube. The particles were sonicated for thirty minutes. Then, 50 ml of Milli-Q water was added, and it was centrifuged for 1 minute at 4000 rev/min extracting the supernatant. The process was repeated until the supernatant pH was neutral. Finally, particles were left to dry in a partial vacuum for a few hours.

5.1.2 Hydrophobic Particles

The hydrophobic particles were obtained from bare silica particles of $3\mu m$ and $5\mu m$ (Bangs Laboratories, USA). The particle surface was modified with dichloro dimethyl silane ($DCDMS$) (Sigma-Aldrich, USA) by dispersing 20 mg of bare silica particles previously cleaned in 0.1% in volume of a solution of $DCDMS$ and ethanol. After that, the particles were dispersed in the $DCDMS$/ethanol solution and stirred

by approximately 10 minutes. The modified particles were rinsed with 20 ml of clean ethanol three times and with chloroform until the supernatant pH was neutral. Finally, the particles were left to dry in a partial vacuum for a few hours.

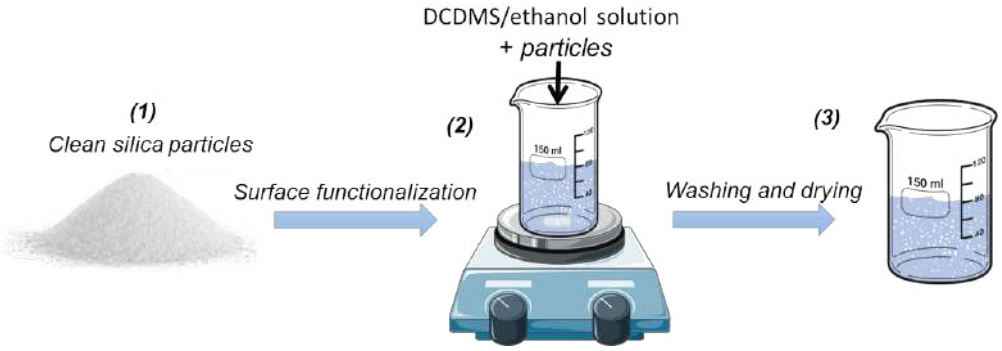

Figure 5.1: Schematic representation of the step-by-step surface functionalization of silica particles. (1) The hydrophobic particles were obtained from bare silica particles of $3\mu m$ and $5\mu m$. (2) The particle surface was modified with $DCDMS$ by dispersing bare silica particles cleaned previously in a $DCDMS$ and ethanol solution. Then, the particles were dispersed in the $DCDMS$/ethanol solution and stirred. (3) The modified particles were rinsed with clean ethanol and chloroform. Finally, the particles were left to dry in a partial vacuum.

5.1.3 Janus Particles

Janus particles used in the experiments have two different chemical compositions on their two hemispheres. One hemisphere is a bare silica (hydrophilic) hemisphere, and the other hemisphere was modified with $DCDMS$ (hydrophobic). To get this kind of Janus particles, a technique of solidified emulsions [73] was used. Initially, 50 mg cleaned bare silica particles of $3\mu m$ and $5\mu m$ (Bangs Laboratories, USA) were adsorbed in the interface of oil in water emulsion, molten paraffin (paraffin,

Sigma Aldrich: water, Nanopure-UV, resistivity 418.3 MO cm) as the oil phase. This emulsion was prepared using 5 ml (for particles of 3μm) and 3 ml (for particles of 5μm) of $DDAB$ (Didodecyldimethylammonium bromide, Sigma Aldrich) at a concentration of $0.04g/l$. The $DDBA$ concentration is such that the particles were adsorbed about half its volume into the paraffin phase. The dispersion of particles and $DDAB$ was mixed with 500 mg of molten paraffin at $75°C$ and stirred 15 minutes to form a stable paraffin-in-water emulsion with the particles at the paraffin/water interface. After that, the paraffin droplets were cooled in a water container to solidify them and form paraffin droplets or colloidosomes. Then, the colloidosomes were filtered and washed with deionized water to remove the $DDAB$ and not adsorbed particles and left to dry for approximately 12 hours. Chemical modification of the exposed surface of the particles in the colloidosomes was carried by a vapor-phase deposition of $DCDMS$ for 10 minutes. After the chemical modification, the paraffin was dissolved in chloroform and washed until no paraffin residues were seen when observed with a Brewster angle microscopy (BAM). Finally, the particles were left to dry several hours in a partial vacuum.

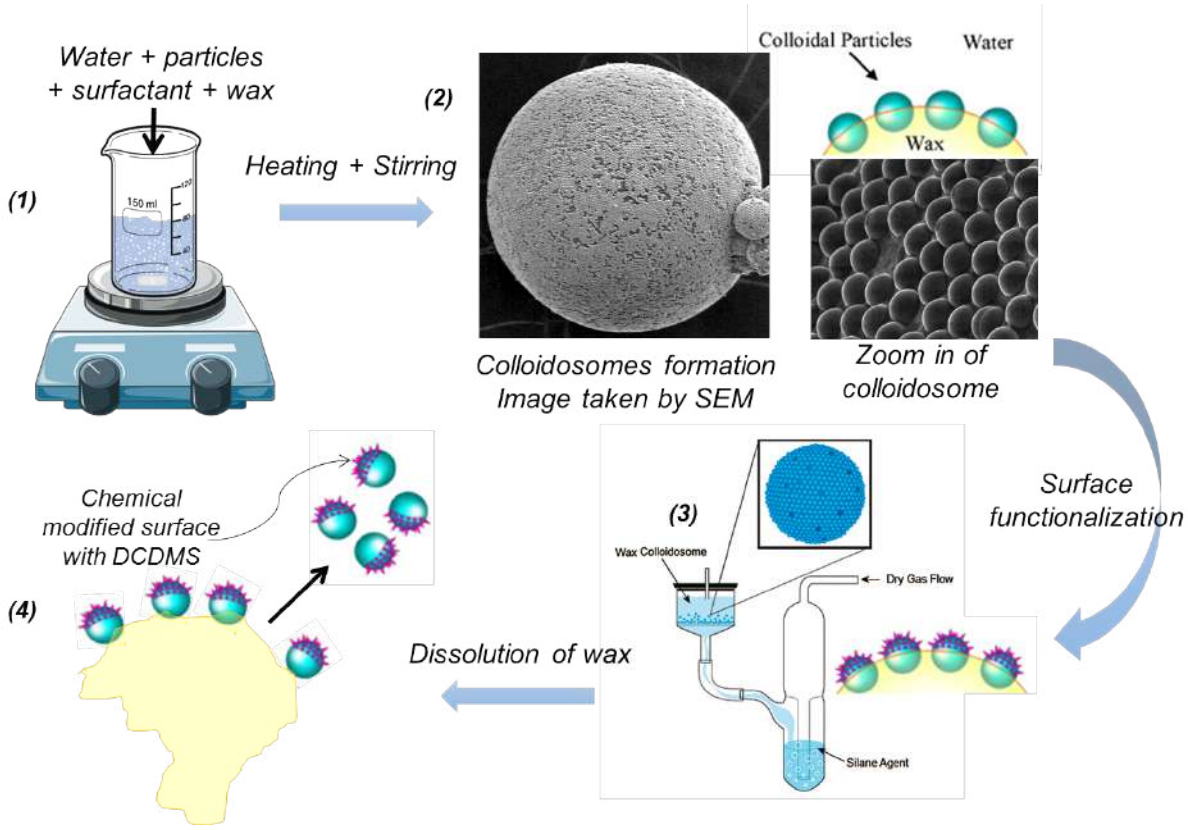

Figure 5.2: Schematic plot of the step-by-step fabrication of Janus particles by a paraffin-in-water emulsion. (1) Particles were added to a paraffin-in-water emulsion with $DDAB$ surfactant. (2) The formed paraffin droplets were cooled in a water container to solidify them and form colloidosomes (image taken by scanning electron microscopy). (3) Vapor-phase deposition of $DCDMS$ was carried out for the chemical modification of the exposed particle surface in the colloidosomes. A dry nitrogen gas flow brings the $DCDMS$ vapor in contact with the colloidosome, which is over a glass frit and gently moved every $5 - 10$ minutes. (4) The paraffin was dissolved in chloroform and washed until clean. Finally, the particles were left to dry several hours in a partial vacuum.

5.2 Capillary interactions between homogeneous colloidal particles

The presented results were obtained with spherical hydrophilic and hydrophobic silica particles of 3 μm and 5 μm in diameter. The experiments were performed in a Langmuir trough (NIMA, USA) mounted on a precision stage that allows controlling the position of the sample in the xyz axis. Before the experiment, the particles were washed to ensure there was no dirt of any kind. The Langmuir trough and syringe used in the monolayer's preparation were also washed and rinsed with ultrapure water (Nanopure-UV, 18.3$M\Omega$).

The monolayer was made with ultrapure water in the Langmuir trough. Subsequently, suspended particles in chloroform were spread on the surface of the water using a syringe. About 10 minutes were waited for the chloroform to be evaporated. Immediately after depositing the particles, most of them were irreversibly trapped at the air/water interface. The measurements were carried out with a controlled temperature of 25°C and with purified air to prevent that any contaminant fell on the monolayer.

To measure the interaction force between two particles, we proceeded by positioning the traps of 12 μm from their centers. The centers' positions and distance between the two optical tweezers were previously measured. Each optical trap center, x_0, was obtained averaging the position of a trapped particle (while keeping the other trap empty), x, i.e, $x_0 = \frac{1}{N}\sum_{i=1}^{i=N} x_i$, where N is the number of frames in the recordings, as the measurements standard deviation is reduced by factor $\frac{1}{\sqrt{N}}$. N was set as $N = 5000$. Then, a pair of particles were trapped with the tweezers and recorded to determine their positions. Afterward, the particles were slowly approximated to

each other and recorded at every distance until contact. The same procedure was carried out with different pairs of particles and different k (for particles of 3 μm). The recordings consisted of $N = 5000$ frames. The trapped particles recordings were analyzed with a tracking program, based on a known algorithm [74] [75] modified by Dr. Alejandro Vásquez in Matlab to obtain the particles centers position. The average interparticle distance and the average particle center positions were obtained. If the interaction of the particles is negligible at a given distance, then the averaged particle positions should coincide with the traps centers position. Otherwise, the difference between averaged particles and traps positions determines the displacement of the particles from the trap center (or equilibrium position) due to the interaction. This displacement is proportional to the interaction force, $F_\alpha = \frac{k(r_q - r)}{2}$, as was shown in Section 4.4. In some cases, at a certain distance, the particles jump-to-contact: the gradient of the interparticle interaction force is stronger than the stiffness of the optical trap, k. The values of k were increased to access smaller interparticle distances, to avoid the jump-to-contact.

5.2.1 Hydrophilic particles

For hydrophilic particles, the measurements were done as described above. However, the interaction forces between pairs of particles were not possible to obtain. The displacements of the particles from the equilibrium position were (possibly) of the same range as the Brownian MSD. The causes for this results could be related to the contact angle of bare silica with water and the MSD of a particle straddled at the air/water interface, as is explained below. The macroscopic contact angle of bare silica in water is approximately 30°. Although this value is measured from a macroscopic droplet of water over a flat surface of bare silica, it can give a clue of

the microscopic contact angle of bare silica particles at air/water interfaces. This angle value says that bare silica is hydrophilic, and when at the interface, a silica particle should be submerged more than half its volume. With this assumption, the minimum distance possible between two particles (even when touching each other) was too large to measure the force with precision. Also, H_2 is small because it is almost horizontal, as schematized in Fig. 5.3.

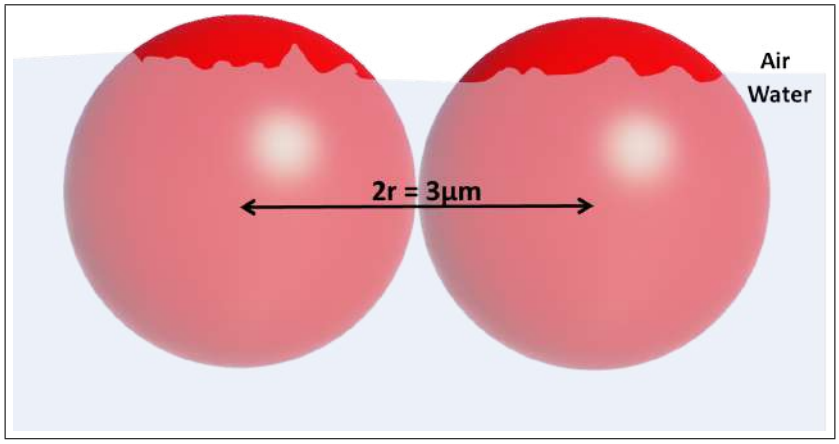

Figure 5.3: Schematic representation to the possible position of hydrophilic particles at air/water interface which could explain the measured results.

On the other hand, when particles are constrained at a water/air interface, the value of their MSD increases as the particles are more submerged in the water. Recently, Nobili *et al.* [14] studied the behavior of spherical bare silica particles of diameters $2-7\ \mu m$ and prolate ellipsoidal particles (obtained by stretching polystyrene beads of 1 μm radius). They found that the MSD of a particle straddling at the air/water interface decreases as the particle protrudes more to the air. These results are contrary to those predicted by classic hydrodynamic analysis [90]. Nobili *et al.* suggested that their unexpected results arise from thermally activated fluctuations

on the interface at the contact line and their coupling to the particle drag. To measure a displacement δx of a particle from the center of an optical trap, it should be larger than the MSD of its Brownian motion ($\delta x_{min} > \sqrt{MSD}$). To distinguished with certainty between the obtained displacement and the particle Brownian motion (this is, to have statistical significance) is desirable that $\delta x > 3\sqrt{MSD}$ (99.7% significance), as the position distribution is Gaussian (this precision can improve if averaged N measures, $\delta x_{min} \geq \frac{\sqrt{MSD}}{\sqrt{N}}$).

Thus, the hydrophilic particles presented a greater MSD value than the hydrophobic ones, as predicted by Nobili *et al.*, and the displacements from the equilibrium position were just a little larger than the MSD. Then we had a small statistical significance that, combined with the situation schemed in Fig.5.3, prevented us from detecting any interacting force.

5.2.2 Hydrophobic particles

The results presented here were obtained following the procedure described at the beginning of this Section. As the particles used here are hydrophobic, the electrostatic interactions are reduced to a minimum (are negligible). In this way, we assure that the only remaining interaction comes from capillarity, and can be modeled as a power-law $F = \frac{C}{r^n}$ in Ref. [27] . As the experiments were performed, we noted that there was a distance at which the particles jump-to-contact with each other. Changing the power of the laser, we could access different values of the constant and thus have access to closer distances between particles avoiding the jump and making it easier to measure the capillary force and the value of n. When particles make contact, it is not possible to separate them with the optical tweezers, because adhesion due to the van der Waals force is very strong at contact. In Fig. 5.4 are

shown different stages of measurement, from large distances until jump-to-contact.

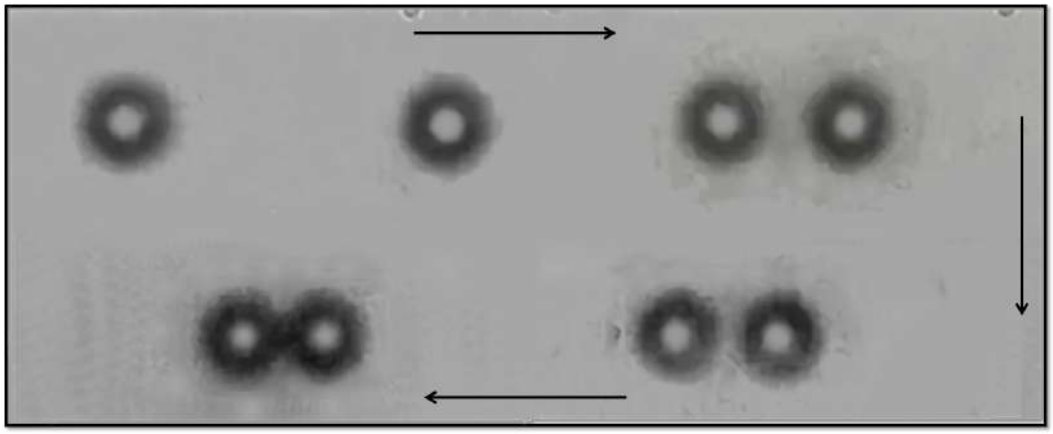

Figure 5.4: Snapshots of the particles trapped by optical tweezers at different distances. The last snapshot in the bottom right shows the particles in contact after one of them jumped from the trap due to their interaction force.

The interaction forces for hydrophobic pairs of colloidal particles of 3 μm adsorbed at the air/water interface calculated based on the experimental data are shown in Fig. 5.5. The points in the graph are from different pairs of particles measurements at different trap stiffness values(k). Each color represents different measurements.

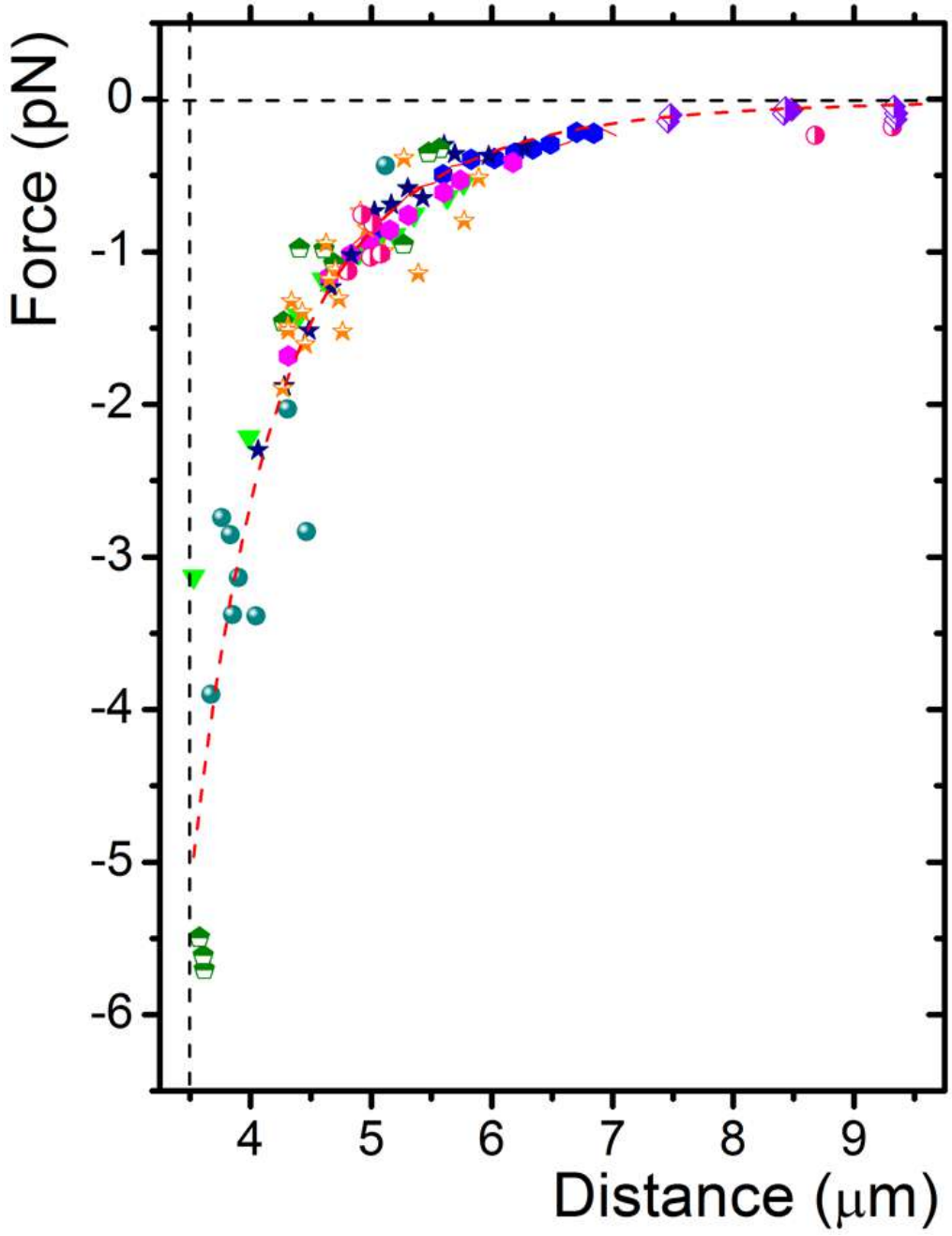

Figure 5.5: Graph of force between two particles of 3 μm trapped in the air/water interface. The x axis represents the distances in microns from center to center between the particles. Experimental data are shown in different colors. The dotted red line corresponds to the fitting.

The experimental results were fitted with a curve of the type $F = \frac{C}{r^n}$. It is an unreliable way to proceed to plot the experimental values, supposedly coming from power-law, in logarithmic scales, and fit them by a least-squares adjustment to get the constants. We used the reliable method of maximum likelihood, where:

$$n = 1 + k \sum_{i=1}^{k} ln \left(\frac{x_i}{x_{min}} \right) \tag{5.1}$$

with standard deviation error given by $\sigma = \frac{n-1}{\sqrt{k}}$, x_i are the measured values of x and x_{min} is the minimum of them [93].

As noted, and as one might expect, the force measured between the particles is independent of the laser power. From the fitting curve, we find $n = 5.02 \pm 0.18$ and $C = -26,326 \pm 2,284\ pN\ \mu m^5$. With these values, the average value for H_2 can be estimated, $H_2 \approx 30\ nm$.

These same experiments were performed with hydrophobic particles of $5\mu m$ in diameter. The results obtained can be seen in Fig.5.6.

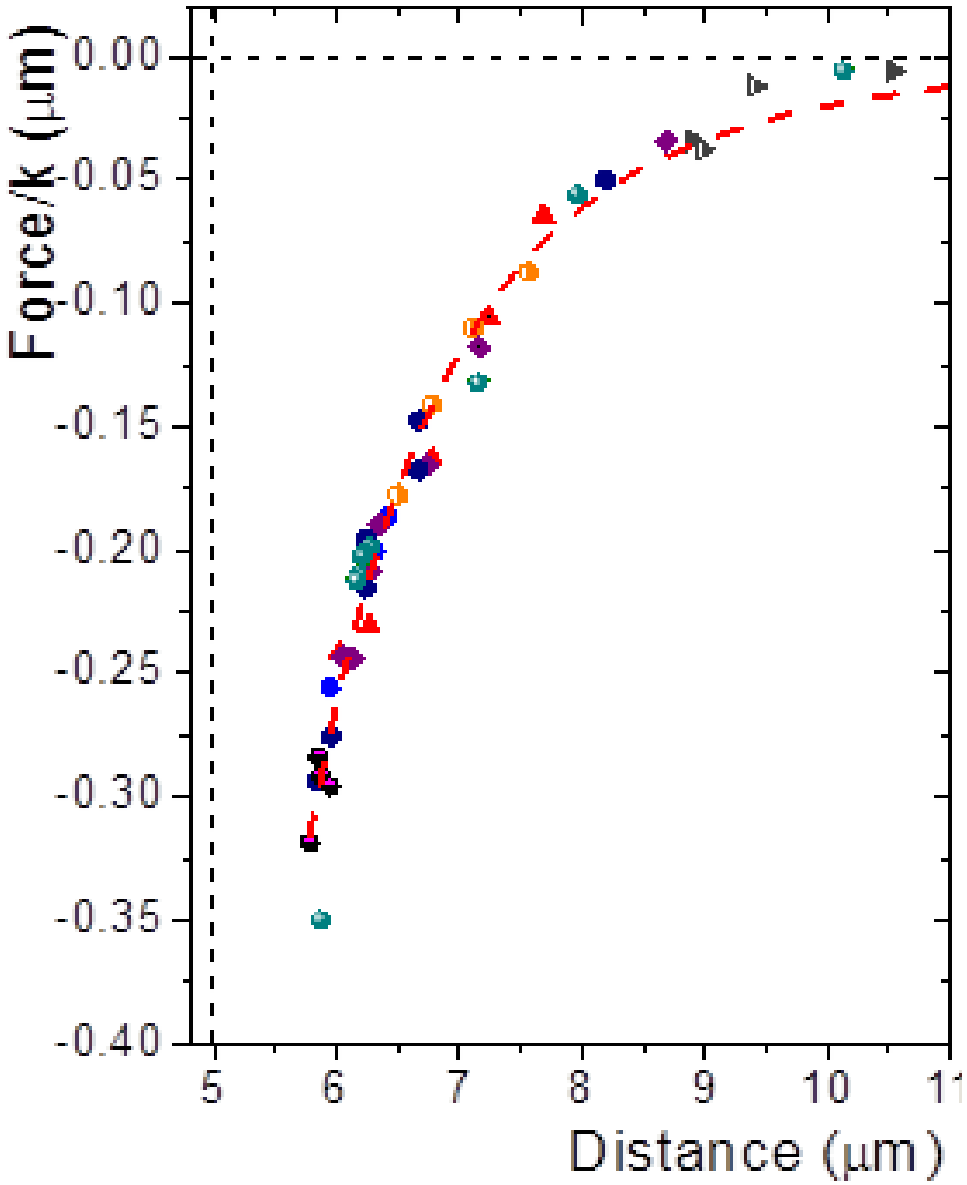

Figure 5.6: Graph of the force over stiffness ratio between two particles of 5 μm trapped in the air/water interface. The x axis represents the distances in microns from center to center between the particles. Experimental data are shown in different colors. The dotted red line corresponds to the fitting.

For the 5 μm hydrophobic particles, the Brownian motion is not very well detectable. We decided to present the force over stiffness ration instead to avoid a significant error in the calculations of the interacting force. As already discussed in Section 4.1.2, when the ray optic regime holds, particles intercept all the converging rays at the laser focus, so the trapping force is the same, irrespective of diameter. However, the trapping rays are spread out over a larger distance the bigger the particle is, so the stiffness should decrease with increasing diameter: a particle with twice the diameter has to move twice as far for the same force to be produced on it by the trap. This effect was noticed in our experiments, which tells us that we obtained reliable results. Reminding that the interacting force equals the force of the trap, and this force is proportional to the displacement from the trap center by a factor given by the stiffness constant, the generic form of the curve is maintained. From these measurements, we can get the precise value of the force exponent, even when the magnitude of the force remains unknown. The experimental results were fitted with a curve of the type $\frac{F}{k} = \frac{C}{r^n}$. The values obtained were $n = 5.04 \pm 0.18$. However, we did not evaluate C; we just measured n from the experimental values of r and the displacements mentioned above. There is no evidence of electrostatic interaction for the fitting values of the curves of both particle sizes, as it was suspected. As it is seen in the graph, the jump of one particle into the other is observed at greater distances than for those observed with particles of 3 μm. This observation indicates that the interacting forces increase as the particle's size increase since the force depends on the particle contact radius (r_c), as it was expected. However, we can not say the same for the size of the particle's chemical or topographic heterogeneity. Defects on particle surface are not proportional to their size but a consequence of the particle synthesis and chemical composition. A rougher surface seems to have as a consequence a stronger capillary force (H_2 seems to be larger for a rougher surface).

Directly measuring capillary forces is the only way we account for the truth of this hypothesis, as these defects have not yet been observed.

5.3 Capillary interactions between inhomogeneous colloidal particles

The results for capillary forces between inhomogeneous particles pairs were obtained using Janus particles with negligible charge. The interaction forces for pairs of Janus colloidal particles of 3 μm adsorbed at the air/water interface were calculated in the same way as with homogeneous particles. Experimental results are shown in Fig. 5.7. Points in the graph are from different pair particles measurements at different trap stiffness values(k). Each color represents different measurements with different colloidal pairs of particles.

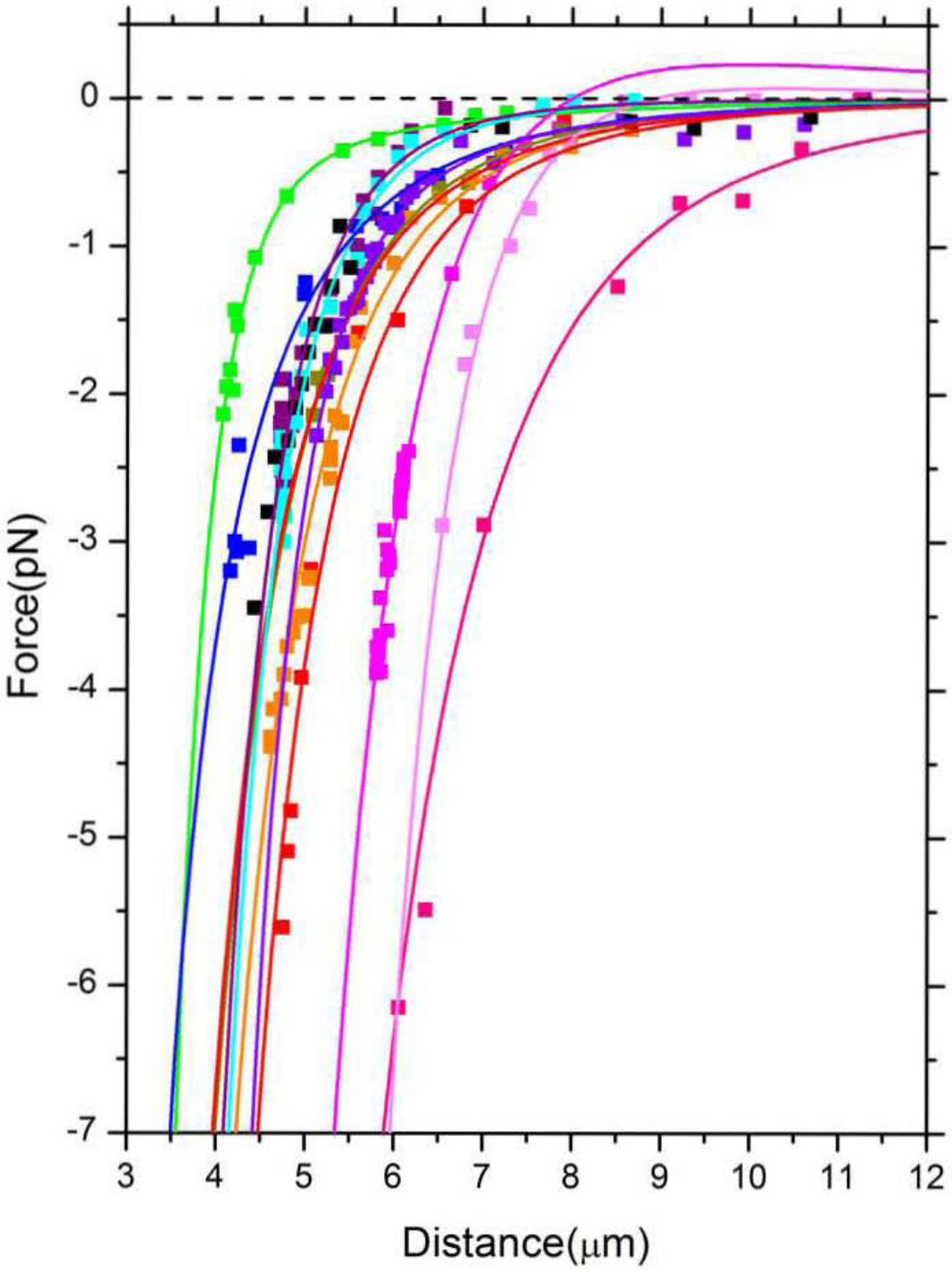

Figure 5.7: Graph of force between two Janus particles of 3 μm trapped in the air/water interface. The x axis represents the distances in microns from center to center between the particles. Experimental data are shown with different colors. The continuous lines correspond to the fitting, which is explained in the text.

The force-stiffness ratio for pairs of Janus colloidal particles of 5 μm adsorbed at the air/water interface calculated based on the experimental data are shown in Fig. 5.8. Points in the graph are from different pair particles measurements at different trap stiffness values(k). Each color represents different realizations with different colloidal pair particles.

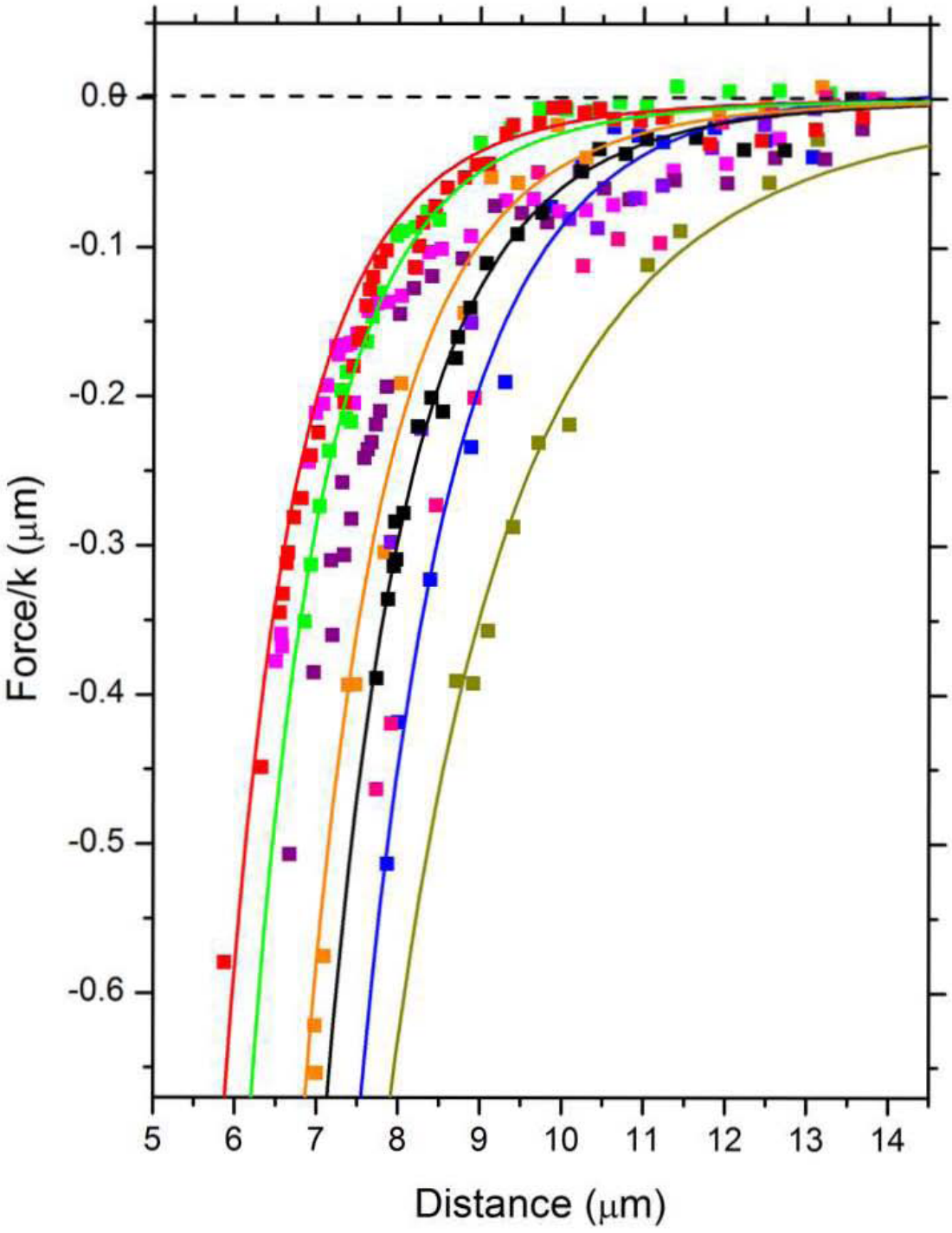

Figure 5.8: Graph of force/stiffness ratio between two Janus particles of 5 μm trapped in the air/water interface. The x axis represents the distances in microns from center to center between the particles. Experimental data are shown with different colors. The continuous lines correspond to the fitting.

From the experimental result is noted that interaction forces between pairs of particles are attractive, in the range of a few pNs. The force curves are different for each pair, and just some of the measurements can be fitted to a r^5 power-law. Other measurements do not follow this power law (not shown). To explain the dispersion of data, we need to consider that the contact line might not follow the hydrophobic-hydrophilic boundary line, which was generated during the synthesis of the Janus particles. These particles had passed through a process in which they were in a wax/water interface, and the approximation of the shape around the particle must be quadruolar, since it is not a perfect straight boundary. We can consider that depending on how water is pinned on the surface defects of the Janus particles, contact lines might be more corrugated in some particles than in others (Fig. 5.9). This increase in corrugation, inevitably, would be reflected in the total interaction force between particle pairs.

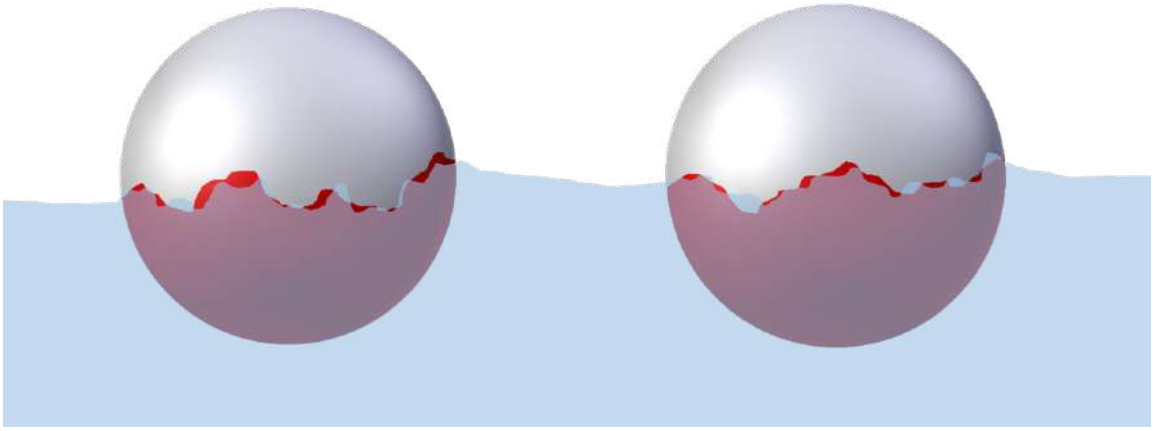

Figure 5.9: Janus particles the air/water interface. The red face is hydrophilic and the white face corresponds to the hydrophobic part. Note that the Janus boundary is irregular and the contact line does not follow precisely this boundary, being different for each particle.

Thus, the form of the contact line should be approximated with extra terms than that considered by Stamou in Ref. [27], so the contact line for Janus particles must be described by

$$h(r,\phi) = H_2 \cos(2\phi - 2\phi_2)\frac{r_c^2}{r^2} + H_3 \cos(3\phi - 3\phi_3)\frac{r_c^3}{r^3} \tag{5.2}$$

The interaction potential between the Janus particles considering the second term in the series, that we calculated following Stamou's procedure (in detail in Appendix C)is given by

$$E = -\frac{12\pi H_{2,A} H_{2,B} r_c^4 \cos(2(\phi_A - \phi_B))}{L^4} - \frac{60\pi H_{3,A} H_{3,B} r_c^6 \cos(3(\phi_A - \phi_B))}{L^6} + \frac{24\pi H_{2,B} H_{3,A} r_c^5 \cos(3\phi_A - 2\phi_B)}{L^5} + \frac{24\pi H_{3,B} H_{2,A} r_c^5 \cos(2\phi_A - 3\phi_B)}{L^5} \tag{5.3}$$

where A and B refer to each particle. With this calculated potential we have that the interaction force

$$F = -\frac{48\pi H_{2,A} H_{2,B} r_c^4 \cos(2(\phi_A - \phi_B))}{L^5} - \frac{360\pi H_{3,A} H_{3,B} r_c^6 \cos(3(\phi_A - \phi_B))}{L^7} + \frac{120\pi H_{2,B} H_{3,A} r_c^5 \cos(3\phi_A - 2\phi_B)}{L^6} + \frac{120\pi H_{3,B} H_{2,A} r_c^5 \cos(2\phi_A - 3\phi_B)}{L^6} \tag{5.4}$$

The first two terms of 5.4 are attractive interactions and the last two correspond to a repulsive interaction. Fig. 5.10 shows examples of the interaction calculated with Eq. 5.4, varying the H_m values, when the quadrupolar and hexapolar terms are of the same order. The resultant capillary force is the black line; blue and red lines are the repulsive and the sum of attractive terms, respectively. When the contribution of

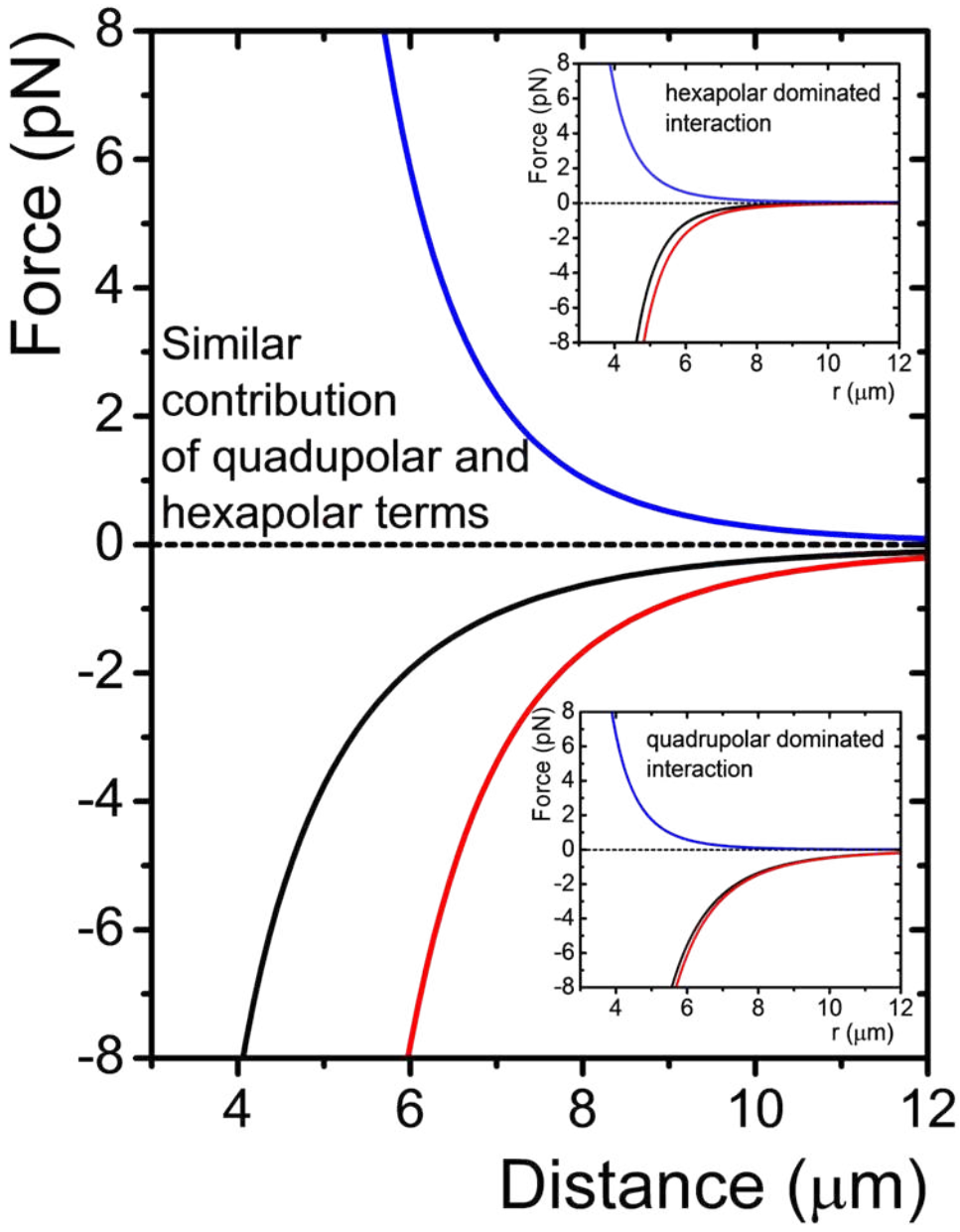

Figure 5.10: Calculated net capillary interaction (black) for Janus particles of 3 μm, when the quadrupolar and hexapolar contributions are of the same order. Blue and red lines are the repulsive and the sum of attractive terms, respectively. Insets present the interactions when the quadrupolar or hexapolar terms dominate.

To fit the experimental data (curves in continuous lines in Fig. 5.7 and 5.8)it was proposed to use due to equation 5.4

$$F = \frac{A}{r^{\alpha}} + \frac{B}{r^{\beta}} + \frac{C}{r^{\gamma}} \tag{5.5}$$

The mean values for the exponents of particles pairs of 3 μm are $\langle\alpha\rangle = 5.05 \pm 0.12$, $\langle\beta\rangle = 7.02 \pm 0.03$, and $\langle\gamma\rangle = 5.96 \pm 0.03$. For particles pairs of 5 μm, we found $\langle\alpha\rangle = 5.02 \pm 0.04$, $\langle\beta\rangle = 6.94 \pm 0.06$, and $\langle\gamma\rangle = 5.80 \pm 0.05$. In both cases, $A < 0$, $B < 0$, and $C > 0$, in agreement with the eq. 5.4. Depending on the measured particle pair, capillary interaction can go from quadrupolar to hexapolar. From all measurements, approximately 40% are dominated by the quadrupolar interaction, $F \approx \frac{A}{r^5}$. Here, probably the contact line and the hydrophilic-hydrophobic boundary coincides. On the contrary, 20% of the measurements are dominated by the hexapolar interaction, $F \approx \frac{C}{r^7}$. Here, the contact line necessarily is more corrugated than in the former case. So, this line does not coincide with the original boundary determined by the synthesis with $m = 2$. The average value for H_2 can be estimated; pure quadrupolar $H_2 \approx 30\ nm$, and pure hexapolar $H_3 \approx 70\ nm$. For the remaining 40% of the measurements, the quadrupolar and hexapolar interactions are approximate of the same size. We did not observe dipolar-dipolar interactions as was thought would be at the beginning. These results of a hexapolar additional term in Janus particles was surprising. The quadrupolar order and the hexagonal order could be noticed in our Janus monolayers, Fig. 5.11 and Fig. 5.12.

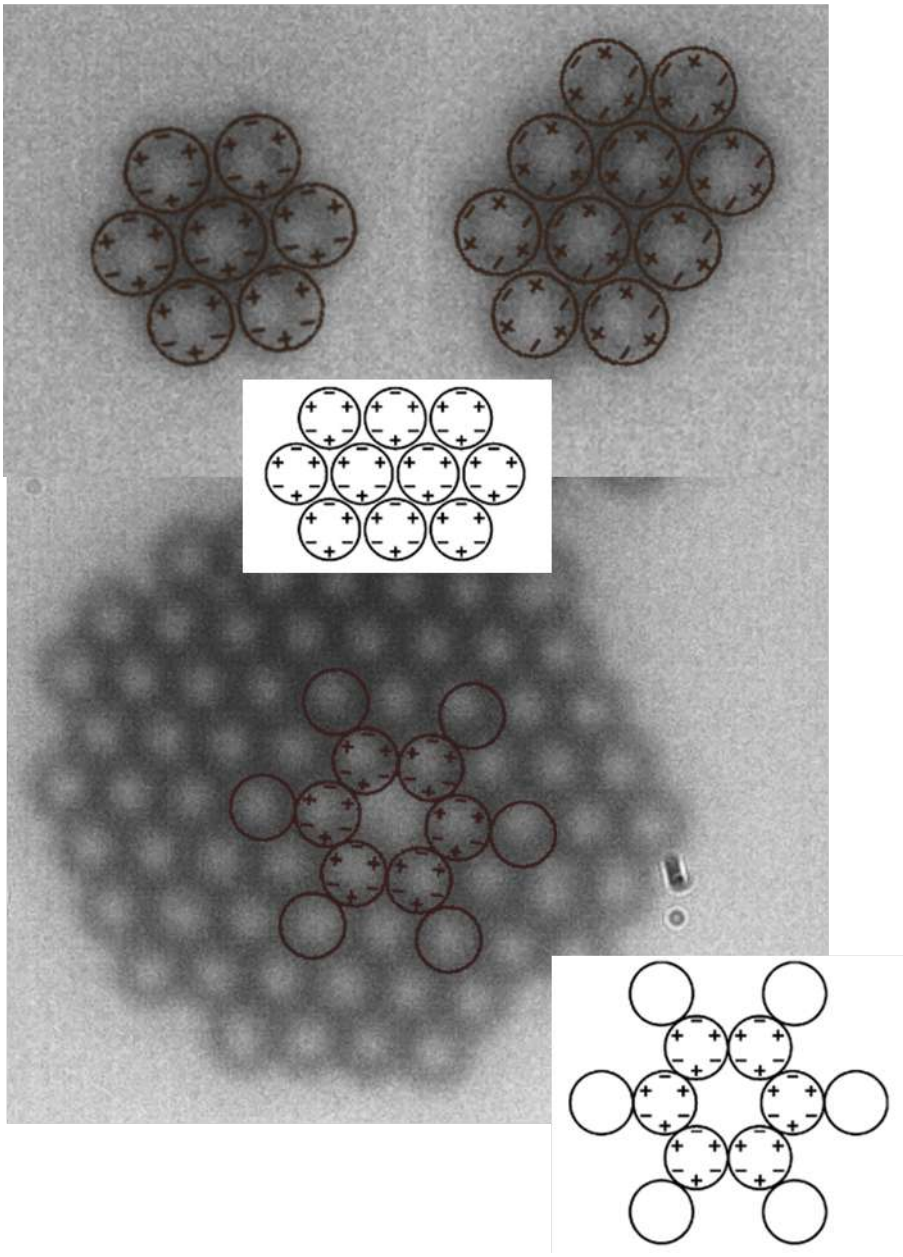

Figure 5.11: Observed hexapolar order during our experiments. Clusters shown as insets predicted by Danov *et al.* [31] for the mentioned interaction. Signs represent the maxima and minima of the contact line undulations.

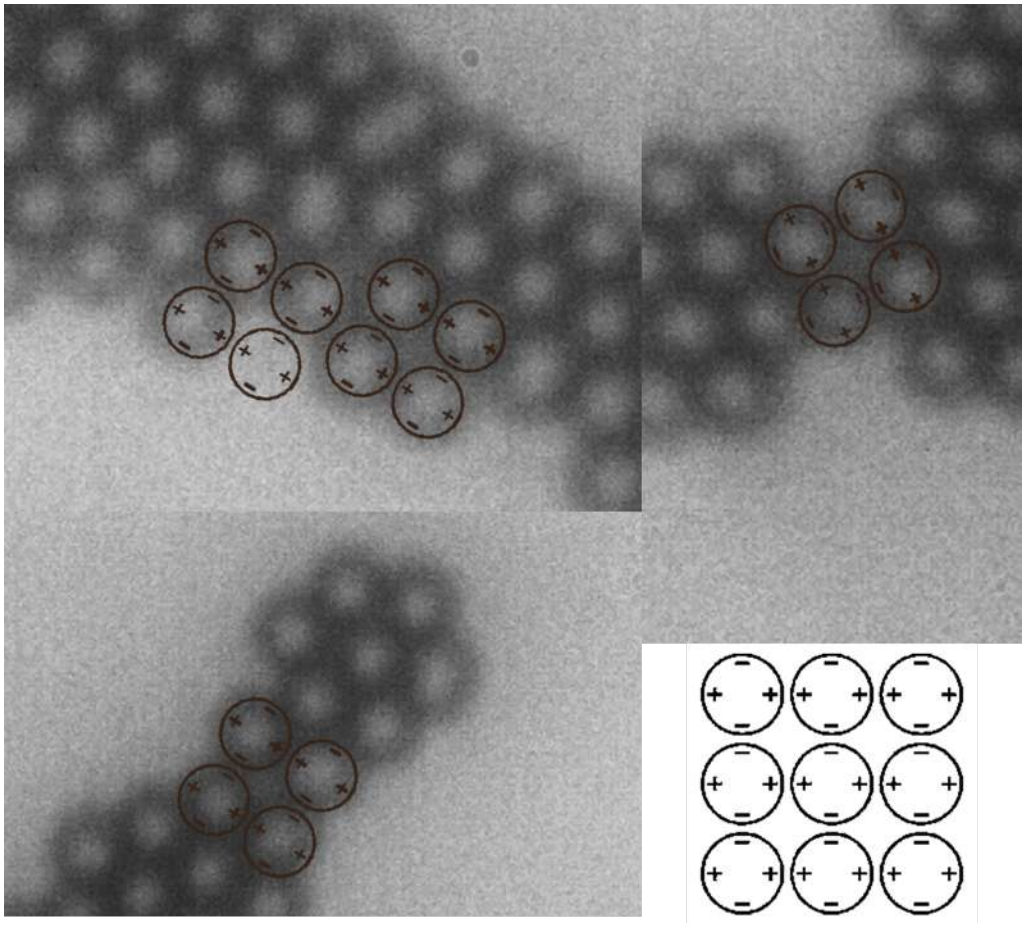

Figure 5.12: Observed quadrupolar order during our experiments. Clusters shown as insets predicted by Danov *et al.* [31] for the mentioned interaction. Signs represent the maxima and minima of the contact line undulations.

5.4 Conclusions

As can be seen from the results presented, the fitting of the experimental data has a form of r^{-5} for hydrophobic particles. This adjustment corresponds to a capillary attraction consistent with that calculated by Stamou *et al* and with the

results obtained by Furst and Park in their measurements. However, the differences between the Furst *et al* experiments and ours are significant in clarifying the origin of the observed interactions: Furts has particles, although of the same diameter as ours, that are negatively charged, so they have a repulsive dipole-dipole interaction. Another difference is that they have an oil/water interface, so they cannot discern whether the attractive interactions they measure are a superposition of other possible interactions and described in the Section 3.1. However, in our system we do not have any of these interactions and we can ensure that the results obtained can correspond to the capillary interactions only.

In the Janus particles we found that the contact line is a superposition of two dominant terms: quadrupolar ($h(r,\phi_3) = H_3 \cos\phi \frac{r}{r_c}^{-2}$) and hexapolar ($r^{-3}$). For the Janus case, the unexpected results obtained shows how complex the phenomena really is. Before we thought that the dipolar term (r^{-3}) would dominate as the Janus particles does not necessarily had to be at equilibrium, this is, Janus boundary parallel to the air/water interface. We believe optical trapping and the handling of the particles to bring them together could give the necessary energy to reach the equilibrium configuration. With our results we can conclude that the origin of the interaction between uncharged colloidal particles straddling at the A/W interface is due to the corrugated shape of the contact line, in agreement to the model of Stamou *et al.* [27].

6. Perspectives

Optical trapping is a very useful technique with a width range of applications due their precision and accuracy. The most important application is the measurement of forces in biological and colloidal systems. With optical trapping forces as small as fN can be detected. With our experimental setup, any object with a greater refractive index than the medium can be trapped, so the possibilities are many. As we could see the roughness of the surface of colloidal particles seems to play an important role in their interaction potential (and thus their general behaviour) when this particles are straddled at a fluid-fluid interface. The most direct form to show that in fact are the deformation of the interface is relevant is measuring this interaction forces. Other experiments with particles with a more prominent roughness could be carried out, even with a more precise control of the particles position at the interface, let's say for example, measuring Janus particles in which the relative position to each other of their two hemisphere are somehow known. This would give a more detailed information about the phenomena. Also could be explore the relation between the size of the surface roughness with the capillary force, something until now unclear.

There is a big interest from science and industry in understanding some systems in the deepest causes of the properties of the material to have control over it. In an oil in water emulsion, there are processes that are not quite understood yet, one of them is coalescence. In coalescence two or more droplets merge during contact to form a single droplet. Coalescence produced as final result the separation of the two phases completely. This is usually an undesirable problem in emulsions. Forces between

A. Single colloidal particle at a fluid, flat and horizontal interface

When we put colloidal particles at a fluid interface, the particles absorb irreversibly at the interface instead of being dispersed in the bulk of one of the phases. For colloidal particles, for which the Bond number is much less than one, the equilibrium position at the interface is determined by the three-phase contact angle, θ, given by Young's equation (as described in Appendix B).

$$\cos\theta_E = \frac{\gamma_{SL} - \gamma_{SV}}{\gamma} \tag{A.1}$$

The energy of the system can be written as

$$E_T = A_{pw}\sigma_{pw} + A_{pa}\sigma_{pa} - A_{aw}\sigma_{aw} \tag{A.2}$$

Because a sphere cap area is given by $A = 2\pi R^2(1 - cos\theta)$, then this leads to

$$E_T = 2\pi R^2(1 + z_0)\sigma_{pw} + 2\pi R^2(1 + z_0)\sigma_{pa} - \pi R^2(1 + z_0^2)\sigma_{aw} \tag{A.3}$$

where z_0 is the height of the particle from the interface ($z_0 = \frac{z}{R}$, Fig.**??**). Which yields to

$$E_0 = \pi R^2\sigma_{aw}\left(z_0 + \frac{2z_0(\sigma_{pw} - \sigma_{pa})}{\sigma_{aw}} + \frac{2(\sigma_{pw} + \sigma_{pa})}{\sigma_{aw}} - 1\right) \tag{A.4}$$

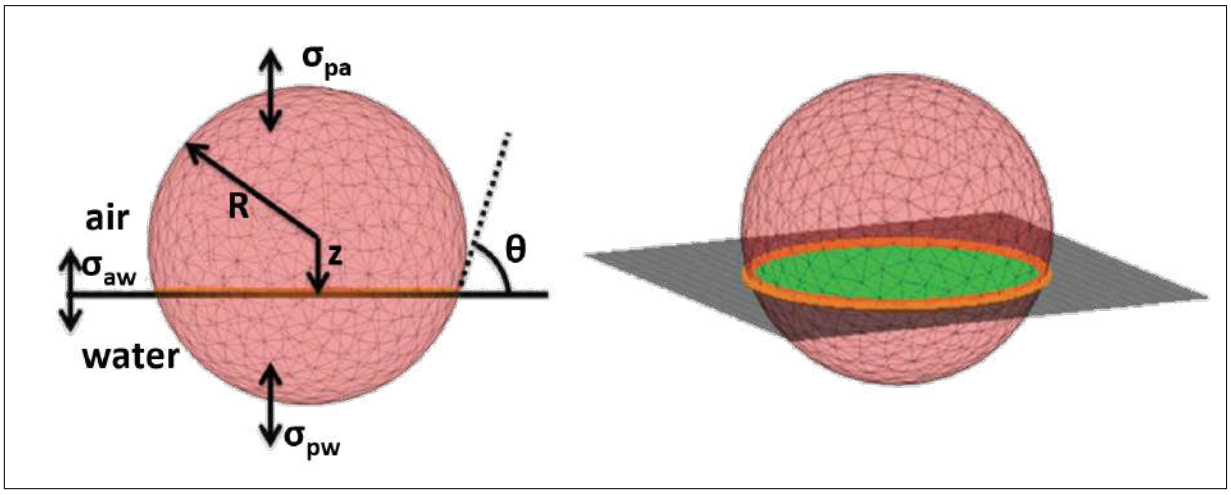

Figure A.1: Schematic representation of a spherical particle at a fluid interface. The green area in the right shows the interface that is removed by the particle [91].

Equation A.4 shows the energy required for the particle to be at the air/water interface. But at what height will the particle straddle so to the position is stable or at equilibrium? This 'equilibrium height' is such that A.4 is minimized. So differentiating and setting to zero $\left(\frac{dE_0}{dz_0} = 0\right)$ we obtain an minimum 'equilibrium height' is

$$z_0^{min} = \frac{\sigma_{pw} - \sigma_{pa}}{\sigma_{aw}} \tag{A.5}$$

From this can be seen that the necessary energy to remove a particle from the energy minima into to either fluid phase is

$$\Delta E_1 = E_0(z_0 = 1) - E_0(z_0 = z_0^{min})) \tag{A.6}$$

Changing the expression into terms of Young's angle, we get the most common expression for the attachment energy of a colloidal particle at a liquid-liquid interface

(Eq. A.7)[91].

$$\Delta E = \pi R^2 \sigma_{aw} (1 \pm \cos\theta)^2 \tag{A.7}$$

As example, take a silica particle of 3 μm in diameter at an air/water interface. The energy needed by the particle to escape from the interface is on the order of $\approx 7 \times 10^{-6} k_B T$ which is a huge energy barrier.

B. Young Equation Derivation

Let's assume an ideally flat surface. If a water drop is placed on such surface, the drop deforms and takes the shape of a perfect spherical cap, as shown in B.1. The cap of the drop has radius R, and a contact angle with the solid surface of θ. For such configuration, we have that

$$V = \frac{\pi R^3}{3}(1 - \cos\theta)^2(2 + \cos\theta) \tag{B.1}$$

$$S = 2\pi R^2(1 - \cos\theta) \tag{B.2}$$

Where V is the volumen and S the surface of the cap.

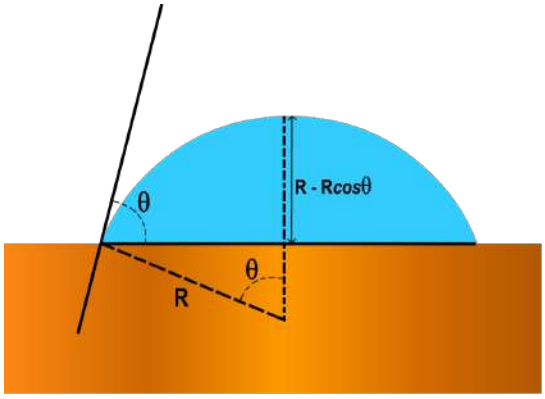

Figure B.1: Water drop partially wetting an ideally flat surface.

The Gibbs free energy of this system is given by

$$G = \gamma S + \pi(R\sin\theta)^2(\gamma_{SL} - \gamma_{SV}) \tag{B.3}$$

where γ,γ_{SL}, and γ_{SV} are the vapor-liquid, solid-liquid, and solid-vapor surface tension, respectively. $\pi(R\sin\theta)^2$ is the drop area that is in contact with the solid surface. If B.1 and B.2 are substitute in B.3, then Gibbs free energy can be expressed in terms of the contact angle and the volume. This is useful given that now the drop equilibrium state can be obtained as a function of θ minimizing the free energy, regarding that the drop is not evaporating, this is $V = constant$.

$$G = \left[\frac{9\pi V^2}{(1-\cos\theta)\,(2+\cos\theta)^2}\right]^{\frac{1}{3}} (2\gamma - (\gamma_{SL} - \gamma_{SV})\,(1-\cos\theta)) \tag{B.4}$$

Minimizing the energy as $\frac{dG}{d\theta}\big|_{\theta=\theta_E} = 0$:

$$\frac{dG}{d\theta} = \left[\frac{9\pi V^2}{(1-\cos\theta)^4\,(2+\cos\theta)^5}\right]^{\frac{1}{3}} 2\,(\gamma_{SL} - \gamma_{SV} - \gamma\cos\theta)\sin\theta = 0 \tag{B.5}$$

$$\gamma_{SL} - \gamma_{SV} = \gamma\cos\theta_E \tag{B.6}$$

$$\cos\theta_E = \frac{\gamma_{SL} - \gamma_{SV}}{\gamma} \tag{B.7}$$

The equation B.7 gives the equilibrium contact angle that the drop should adopt on a perfectly flat and homogenous surface and is known as Young's equation[92].

C. Calculation of the force between hexapoles and quadrupoles

The energy produced for the air-water interface deformation due to the presence of a colloidal particle is given by

$$\delta E = \gamma \delta S \tag{C.1}$$

where γ is the air-water surface tension and δS is the excess area, i.e., the difference between the deformed surface area $S*$ and the flat interface S.

The excess of area δS is

$$\delta S = \frac{1}{2}\int_{r_c}^{\infty}\int_{0}^{2\pi} (\boldsymbol{\nabla} h)^2 r d\phi dr \tag{C.2}$$

Taking into consideration tow terms now, $m = 3$ and $m = 3$, we have

$$\delta S = \frac{1}{2}\int_{r_c}^{\infty}\int_{0}^{2\pi} \left[\boldsymbol{\nabla}\left(\frac{H_2 r_c^2 \cos(2(\phi-\phi_{2,0}))}{r^2} + \frac{H_3 r_c^3 \cos(3(\phi-\phi_{3,0}))}{r^3}\right)\right]^2 r d\phi dr \tag{C.3}$$

For this case

$$\boldsymbol{\nabla} h = \boldsymbol{\nabla}\left(\frac{H_2 r_c^2 \cos(2(\phi-\phi_{2,0}))}{r^2} + \frac{H_3 r_c^3 \cos(3(\phi-\phi_{3,0}))}{r^3}\right)\cdot \boldsymbol{\nabla}\left(\frac{H_2 r_c^2 \cos(2(\phi-\phi_{2,0}))}{r^2} + \frac{H_3 r_c^3 \cos(3(\phi-\phi_{3,0}))}{r^3}\right) \tag{C.4}$$

Resulting in

$$\boldsymbol{\nabla} h = -\frac{2H_2 r_c^2 \cos(2(\phi-\phi_{2,0}))}{r^3} - \frac{3H_3 r_c^3 \cos(3(\phi-\phi_{3,0}))}{r^4}\hat{r} + \frac{-\frac{2H_2 r_c^2 \sin(2(\phi-\phi_{2,0}))}{r^2} - \frac{3H_3 r_c^3 \sin(3(\phi-\phi_{3,0}))}{r^3}}{r}\hat{\phi} \tag{C.5}$$

So,

$$(\boldsymbol{\nabla} h)^2 = \boldsymbol{\nabla} h \cdot \boldsymbol{\nabla} h = \frac{r c^4 (4H_2^2 r^2 + 9H_3^2 r_c^2 + 12H_2 H_3 r r_c Cos(\phi + 2\phi_{2,0} - 3\phi_{3,0}))}{r^8} \tag{C.6}$$

The *self-energy*, C.1, is

$$\delta E \approx \frac{\gamma}{2}\int_{r_c}^{\infty}\int_0^{2\pi} r c^4 \frac{4H_2^2 r^2 + 9H_3^2 r_c^2 + 12H_2 H_3 r r_c \cos(\phi + 2\phi_{2,0} - 3\phi_{3,0})}{r^8} r d\phi dr \tag{C.7}$$

$$\delta E \approx \frac{1}{2}\pi\gamma\left(2H_2^2 + 3H_3^2\right) \tag{C.8}$$

The result C.8 is the sum of two superposed fields, h_2 and h_3, as expected for the

nature of the solution for Δh.

The deformation of the interface when two particles approach, δS_{AB}, is due to the superposition of the individual deformation effect. The energy δE_{AB} of this system is given by

$$\delta E = \gamma(\delta S_{AS} - \delta S_A - \delta S_B) \tag{C.9}$$

δS_A and δS_B are the areas around the isolated particles. We assume that h_A is small at particle B and that h_B is small at particle A. So,

$$\begin{aligned}\delta E = \frac{\gamma}{2}\int_S dS\left(\left(\boldsymbol{\nabla}\left(h_A + h_B\right)\right)^2 - \left(\boldsymbol{\nabla} h_A\right)^2 - \left(\boldsymbol{\nabla} h_B\right)^2\right) \\ = \gamma\int \boldsymbol{\nabla} h_A \cdot \boldsymbol{\nabla} h_B dS\end{aligned} \tag{C.10}$$

As the boundary conditions are known, it it better to express C.10 with an integral over the boundary, this can be accomplished using the first Green identity, so we get

$$\delta E = \gamma\int_C h_B(\mathbf{n}\cdot\boldsymbol{\nabla} h_A)dC - \int_S h_B \Delta h_A dS \tag{C.11}$$

But, as was assumed $\delta h = 0$, then

$$\delta E = \gamma\int_C h_B(\mathbf{n}\cdot\boldsymbol{\nabla} h_A)dC \tag{C.12}$$

Now, is convenient to express h_A and h_B as follows

$$h_A = h_{2,A} + h_{3,A} = \frac{H_{2,A} r_c^2 \cos(2\phi - 2\phi_A)}{r^2} + \frac{H_{3,A} r_c^3 \cos(3\phi - 3\phi_A)}{r^3}$$
$$h_B = h_{2,B} + h_{3,B} = \frac{H_{2,B} r_c^2 \cos(2\phi - 2\phi_B)}{r^2} + \frac{H_{3,B} r_c^3 \cos(3\phi - 3\phi_B)}{r^3} \tag{C.13}$$

Then, the energy of the system is

$$\delta E = \gamma \int_C h_B \mathbf{n} \cdot \boldsymbol{\nabla} h_A dC = \gamma \left(\int_C h_{2,B} \mathbf{n} \cdot \boldsymbol{\nabla} h_{2,A} dC + \int_C h_{3,B} \mathbf{n} \cdot \boldsymbol{\nabla} h_{3,A} dC + \int_C h_{2,B} \mathbf{n} \cdot \boldsymbol{\nabla} h_{3,A} dC + \int_C h \right. \tag{C.14}$$

Integrating separately,

$$\int_C h_{2,B} \mathbf{n} \cdot \boldsymbol{\nabla} h_{2,A} dC = -\frac{12\pi H_{2,A} H_{2,B} r_c^4 \cos(2(\phi_A - \phi_B))}{L^4} \tag{C.15}$$

$$\int_C h_{3,B} \mathbf{n} \cdot \boldsymbol{\nabla} h_{3,A} dC = -\frac{60\pi H_{3,A} H_{3,B} r_c^6 \cos(3(\phi_A - \phi_B))}{L^6} \tag{C.16}$$

$$\int_C h_{2,B} \mathbf{n} \cdot \boldsymbol{\nabla} h_{3,A} dC = +\frac{24\pi H_{2,B} H_{3,A} r_c^5 \cos(3\phi_A - 2\phi_B)}{L^5} \tag{C.17}$$

$$\int_C h_{3,B} \mathbf{n} \cdot \boldsymbol{\nabla} h_{2,A} dC = +\frac{24\pi H_{3,B} H_{2,A} r_c^5 \cos(2\phi_A - 3\phi_B)}{L^5} \tag{C.18}$$

The total energy is then,

$$\delta E = -\frac{12\pi H_{2,A} H_{2,B} r_c^4 \cos(2(\phi_A - \phi_B))}{L^4} - \frac{60\pi H_{3,A} H_{3,B} r_c^6 \cos(3(\phi_A - \phi_B))}{L^6} + \frac{24\pi H_{2,B} H_{3,A} r_c^5 \cos(3\phi_A - 2\phi_B)}{L^5} + \frac{24\pi H_{3,B} H_{2,A} r_c^5 \cos(2\phi_A - 3\phi_B)}{L^5} \tag{C.19}$$

The terms in C.19 correspond to quadrupolar-quadrupolar, quadrupolar-hexapolar and hexapolar-hexapolar interactions between the particles.

References

[1] https://byjus.com/chemistry/classification-of-colloids.

[2] Ramsden W (1903) Separation of solids in the surfacelayers of solutions and suspensions. Proc R Soc Lond 72: 156–164.

[3] Pickering SU (1907) Emulsions. J Chem Soc 91: 2001–2021.

[4] Forster JD, et al. Assembly of optical-scale dumbbells into dense photonic crystals. ACS Nano 5:6695–6700, (2011).

[5] Ding T, Song K, Clays K, Tung C-H, Fabrication of 3D photonic crystals of ellipsoids: Convective self-assembly in magnetic field, Adv Mater, 21:1–5, (2009).

[6] Stratford K, Adhikari R, Pagonabarraga I, Desplat JC, Cates ME Colloidal jamming at interfaces: A route to fluid-bicontinuous gels, Science, 309:2198–2201 (2005).

[7] Cates ME, Clegg PS, Bijels: A new class of soft materials, Soft Matter, 4:2132–2138 (2008).

[8] Pawar AB, Caggioni M, Ergun R, Hartel RW, Spicer PT, Arrested coalescence in Pickering emulsions, Soft Matter, 7:7710–7716 (2011).

[9] Velev O, Furusawa K, Nagayama K, Assembly of latex particles by using emulsion droplets as templates. 1. Microstructured hollow spheres, Langmuir, 12:2374–2384 (1996).

[10] V. N.Manoharan, Pinned down, Nature Materials, 14, 869 (2015).

[11] Vella, D., and Mahadevan, L., The Cheerios Effect, Am. J. Phys. (2005) 73, 817.

[12] Peter A. Kralchevsky and Kuniaki Nagayama, Capillary Forces between Colloidal Particles, Langmuir, 10, 23-36 (1993).

[13] Nikolaides, M. et al., Electric-field-induces Capillary Attraction between like-charged at Liquid Interfaces, Nature (2002) 420, 299.

[14] Boniello, G. et al. Nature Mater., Brownian diffusion of a partially wetted colloid, 14, 908–911 (2015).

[15] D. M. Kaz, R. McGorty, M. Man. M. P. Brenner, V. N. Manoharan, Physical ageing of the contact line on colloidal particles at liquid interfaces, Nature Materials 11, 138 (2012).

[16] D. Bonn, J. Eggers, J. Indekeu, J.M. and E. Rolley, Wetting and Spreading, Rewies of Modern Physics, 18, 739-805 (2009).

[17] Yuehua Yuan and T. Randall Lee, Chapter 1, Contact Angles and Wetting Properties.

[18] A. Marmur, Contact-angle hysteresis on heterogeneous smooth surfaces: theoretical comparison of the captive bubble and drop methods, Colloids and Surfaces. A 136, 209-215 (1998).

[19] C. Huh and S.G. Mason, Effects of surface roughness on wetting (theoretical), J.Colloid and Interface Sci. 60, 11-38 (1977).

[20] Y. Pomeau and J. Vannimenus, Contact angle on heterogeneous surfaces: Weak heterogeneities, J.Colloid and Interface Sci. 104, 477-488 (1985).

[21] U. Opik, Contact-Angle Hysteresis Caused by a Random Distribution of Weak Heterogeneities on a Solid Surface, J.Colloid and Interface Sci. 223, 143-166 (2000).

[22] Pierre-Gilles de Gennes, Simple Views on Condensed Matter, Third Edition, World Scientific Publishing Co. Pte. Ltd. (2003).

[23] J. H. Fendler, Nanoparticles at air water interfaces, Curr. Opin. Colloid Interface Sci. 1, 202 (1996).

[24] Ryan McGortyy, Jerome Fung, David Kaz, Vinothan N. Manoharan, Colloidal self-assembly at an interface, Material today, Elsevier, 13, 6 (2010).

[25] M. Daoud, C. E. Williams, Soft Matter Physics, (Springer-Verlag, Berlin, 1999).

[26] P. Pieranski, Two-Dimensional Interfacial Colloidal Crystals, Phys. Rev. Lett. 45, 569 (1980).

[27] D. Stamou, C. Duschl and D. Johannsmann, Long-range attraction between colloidal spheres at the air-water interface: The consequence of an irregular meniscus, Phys. Rev. E. 62, 5263 (2000).

[28] P. G. de Gennes, Wetting: statistics and dynamics, Rev. Of Mod. Phys., 57, 827 (1985).

[29] A. W. Adamson and A. P. Gast, Physical Chemistry of Surfaces (Wiley, New York, 1997).

[30] Detrich Á., Nyári M., Volentiru E., and Hórvölgyi Z., Estimation of contact angle for hydrophobic silica nanoparticles in their hexagonally ordered layer, Materials Chemistry and Physics, 140(2-3), 602–609 (2013).

[31] K. D. Danov, P. A. Kralchevsky, B. N. Naydenov and G. Brenn, Interactions between Particles with an Undulated Contact Line at a Fluid Interface: Capillary Multipoles of Arbitrary Order, J. Col. Interface Sci. 287, 121 (2005).

[32] N. Bowden, A. Terfort, J. Carbeck, G.M. Whitesides, Self-Assembly of Mesoscale Objects into Ordered Two-Dimensional Arrays, Science, 276, 233–235 (1997).

[33] N. Bowden, I.S. Choi, B.A. Grzybowski, G.M. Whitesides, Mesoscale Self-Assembly of Hexagonal Plates Using Lateral Capillary Forces: Synthesis Using the Capillary Bond, J. Am. Chem. Soc., 121, 5373–5391 (1999).

[34] D.B. Wolfe, A. Snead, C. Mao, N.B. Bowden, G.M. Whitesides, Mesoscale Self-Assembly: Capillary Interactions When Positive and Negative Menisci Have Similar Amplitudes, Langmuir, 19, 2206–2214 (2003).

[35] A.B.D. Brown, C.G. Smith, A.R. Rennie, Fabricating colloidal particles with photolithography and their interactions at an air-water interface, Phys. Rev. E, 62, 951– 960 (2000).

[36] B. J. Park and E. M. Furst, Attractive interactions between colloids at the oil-water interface, Soft Matter 7, 7676 (2011).

[37] A. Kozina, S. Ramos, P. Díaz-Leyva and R. Castillo, Disorder Induced by Capillary Interaction between Colloidal Particles Trapped at the Air/Water Interface, J. Phys. Chem. C. 120, 16879 (2016).

[38] Y. Yi, L. Sanchez, Y. Gao, Y. Yu, Janus particles for biological imaging and sensing Analyst, 141 (12), 3526-3539 (2016).

[39] A. Walther, A.H.E. Mueller Janus particles: synthesis, self-assembly, physical properties, and applications Chem. Rev., 113, 7, 5194-5261 (2013).

[40] Du, R.K. O'Reilly Anisotropic particles with patchy, multicompartment and Janus architectures: preparation and application Chem. Soc. Rev., 40, 5, 2402-2416 (2011).

[41] S. Li, L. Zhang, X. Chen, T. Wang, Y. Zhao, L. Li, C. Wang Selective growth synthesis of ternary janus nanoparticles for imaging-guided synergistic chemo- and photothermal therapy in the second NIR window, ACS Appl. Mater. Interfaces, 10 (28), 24137-24148 (2018).

[42] P.G. de Gennes Soft matter, Science, 256 (5056), 495-497 (1992).

[43] Alberto Concellón, Cassandra A. Zentner, Timothy M. Swager. Dynamic Complex Liquid Crystal Emulsions. Journal of the American Chemical Society, 141, 45, 18246-18255 (2019).

[44] K. Kim, J.H. Guo, Z.X. Liang, D.L. Fan Artificial micro/nanomachines for bioapplications: biochemical delivery and diagnostic sensing, Adv. Funct. Mater., 28, 25, 1705867 (2018).

[45] X.M. Li, L. Zhou, Y. Wei, A.M. El-Toni, F. Zhang, D.Y. Zhao, Anisotropic growth-induced synthesis of dual-compartment janus mesoporous silica nanoparticles for bimodal triggered drugs delivery, J. Am. Chem. Soc., 136 (42), 15086-15092 (2014).

[46] L. Zhang, M. Zhang, L. Zhou, Q. Han, X. Chen, S. Li, L. Li, Z. Su, C. Wang, Dual drug delivery and sequential release by amphiphilic Janus nanoparticles for liver cancer theranostics, Biomaterials, 181, 113-125 (2018).

[47] Parmar J, Ma X, Katuri J, et al,. Nano and micro architectures for self-propelled motors, Sci. Technol. Adv. Mater., 16, 14802 (2015).

[48] Orozco J, Mercante LA, Pol R, Merkoci A, Graphene-based Janus micromotors for the dynamic removal of pollutants, J. Mater. Chem. A, 4, 3371–3378 (2016).

[49] Baraban L, Tasinkevych M, Popescu MN, et al. Transport of cargo by catalytic Janus micro-motors, Soft Matter, 8, 48–52 (2012).

[50] S. Jiang, S. Granick, Janus balance of amphiphilic colloidal particles, J. Chem. Phys. 127, 161102 (2007).

[51] H. Rezvantalab and S. Shojaei-Zadeh, Capillary-Induced Interactions between Spherical Janus Particles at Fluid-Liquid Interfaces, Soft Matter, 9, 3640 (2013).

[52] A. Kumar, B. J. Park, F. Tu and D. Lee, Amphiphilic Janus particles at fluid interfaces, Soft Matter, 9, 6604 (2013).

[53] S. Jiang and S. Granick, J. Chem. Phys., 2007, 127, 161102.

[54] B. P. Binks and P. D. I. Fletcher, Langmuir, 2001, 17, 4708–4710.

[55] D. L. Cheung and S. A. F. Bon, Soft Matter, 2009, 5, 3969–3976.

[56] Y. Hirose, S. Komura and Y. Nonomura, J. Chem. Phys., 2007, 127, 054707.

[57] B.J. Park, T. Brugarolas and D. Lee, Janus particles at an oil-water interface, Soft Matter Communication, 7, 6413 (2011).

[58] J. C. Loudet, A.G. Yodh and B. Pouligny, Wetting and Contact Lines of Micrometer-Sized Ellipsoids, Phys. Rev. Lett., 97, 018304 (2006).

[59] R. Di Leonardo, F. Saglimbeni and G. Ruocco, Very-Long-Range Nature of Capillary Interactions in Liquid Films, Phys. Rev. Lett., 100, 106103 (2008).

[60] D. Hönig, D. Möbius, Direct visualization of monolayers at the air-water interface by Brewster angle microscopy, J. Phys. Chem. 95, no. 12, 1991.

[61] D. A. McQuarrie, Statistical Mechanics, University Science Books (2000).

[62] J.P. Hansen, I. R. McDonald, Theory of Simple Liquids (Academic, New York, 1986).

[63] Maxwell J. C. A Treatise on Electricity and Magnetism Constable (1891) reprinted by Dover Books, New York, 1954).

[64] A. Ashkin, Acceleration and trapping of particles by radiation pressure, Phy.Rev.Let., 24, 156 (1970).

[65] A. Ashkin, Science 210, 1081 (1980); V. S. Letokhov and V. G. Minogin, Phys. RQp.73, 1 (1981).

[66] A. Ashkin and J. P. Gordon,Opt. Lett. 8, 511 (1983).

[67] A. Ashkin and J. M. Dzielzic, Phys. Rev. Lett. 54, 1245 (1985).

[68] A. Ashkin, J.M. Dziedzic, J.E. Bjorkholm, and S. Chu, Observation of a single-beam gradient force optical trap for dielectric particles, Optics Lett., 11 (1986), 288.

[69] A. Ashkin, Forces of a single-beam gradient laser trap on a dielectric sphere in the ray optics regime, Biophys. J. , 61, 569 (1992).

[70] A. Ashkin, Optical trapping and manipulation of neutral particles using lasers (Word Scientific, E.U.A., 2006).

[71] P. C. Chaumet, M. Nieto-Vesperinas, Time-averaged total force on a dipolar sphere in an electromagnetic field, Opt. Lett. 2000, 25, 1065.

[72] Perro A., Meunier F., Schmitt V., and Ravaine S. (2009). Production of large quantities of 'Janus' nanoparticles using wax-in-water emulsions. Colloids and Surfaces A: Physicochemical and Engineering Aspects, 332(1), 57–62.

[73] Jian, S., Schult, M. J., Chen Q., Moore J. S., and Granick S. (2008). Solvent-Free Synthesis of Janus Colloidal Particles. Langmuir, 24(18), 10073–10077.

[74] D.G. Grier, A Revolution in Optical Manipulation, Nature, 424 (2003), 21.

[75] http://gibbs.engr.ccny.cuny.edu/technical/Tracking/ChiTrack.php

[76] K.C. Neuman and S.M. Block, Optical trapping, Rev. Sci. Instru.,. 75 (2004), 2787.

[77] A. Gutiérrez, R. Castillo, Optical trapping of particles at the air/water interface for studies in Langmuir monolayers, Rev. Mex. Fís., 56, 339 (2010).

[78] M. J. Kidger, Intermediate Optical Design, SPIE PRESS (Bellingham, Washington, 2004).

[79] J. C. Crocker and D.G. Grier, Methods of Digital Video Microscopy for Colloidal Studies, J. Col. Interface Sci., 179 (1996), 298.

[80] B. E. A. Saleh, M. C. Teich, Fundamental of Photonics, Wiley (1991).

[81] I. Langmuir, The Constitution and Fundamental Properties of Solids and Liquids. II Liquids, JACS, 39 (1917), 1848.

[82] http://www.biolinscientific.com/technology/l-lb-ls-technique/.

[83] Jun, Yonggun et al. Calibration of Optical Tweezers for In Vivo Force Measurements: How Do Different Approaches Compare?, Biophysical Journal 107.6 (2014): 1474–1484. PMC. Web. 6 Sept. 2018.

[84] R. M. Simmons, J. T. Finer, S. Chu, J. A. Spudich, Quantitative Measurement of force and Displacement Using an Optical Trap, Biophysical Journal, 70, 4 (1996), 1813-1822.

[85] Sarshar, Mohammad, Winson T. Wong, and Bahman Anvari. Comparative Study of Methods to Calibrate the Stiffness of a Single-Beam Gradient-Force Optical Tweezers over Various Laser Trapping Powers, Journal of Biomedical Optics 19.11 (2014): 115001. PMC. Web. 6 Sept. 2018.

[86] Rohrbach, A. and Stelzer, E.H.K. (2002). Trapping forces, force constants and potential depths for dielectric spheres in the presence of spherical aberrations. Appl Opt 41, 2494–2507.

[87] B.Capella, G. Dietler, Force-distance Curves by Atomic Force Microscopy, Srface Science Reports, 34, 1-104, 1999.

[88] L. Hong, S. Jiang and S. Granick, Simple Method to Produce Janus Colloidal Particles in Large Quantity, Langmuir, 22 (2006), 9495.

[89] M. P. Allen, D. J. Tildesley, Computer Simulation of Liquids, Clarendon Press (Oxford, 1987).

[90] Fischer T. M., Dhar, P., and Heinig, P. (2006). The viscous drag of spheres and filaments moving in membranes or monolayers. Journal of Fluid Mechanics, 558, 451.

[91] N. Ballard, A. D. Law and S. A. F. Bon, Colloidal particles at fluid interfaces: behaviour of isolated particles, Soft Matter, 15, 1186 (2019).

[92] g. Whyman, E. Bormashenko and T. Stein, The rigorous of Young, Cassie-Baxter and Wenzel equations and the analysis of the contact angle hysteresis phenomenon, Chem. Phys. Letters, 450 (2008), 355-359.

[93] M. E. J. Newman, Power laws, Pareto distributions and Zipf's law, Contemp. Phys. 46, 323 (2005).

[94] S. Jiang, S. Granick, Janus balance of amphiphilic colloidal particles, J. Chem. Phys. 127, 161102 (2007).